



University of
Salford
MANCHESTER

1967 - 2017 50 YEARS



Effect of repurposed drugs on the cellular properties of childhood cancer: in vitro & in silico studies

By: Shazia Begum

Program: MSc by research Biochemistry

Submission year: 2022

University & School: University of Salford, School of
Science, Engineering and Environment

Supervisors: Dr Anna Akinshina & Dr Joanna Denbigh

Co-supervisors: Dr Pika Miklavc & Professor Peter
Gardner

Table of Contents

List of tables	5
List of figures	5
Acknowledgements	12
Abbreviations	12
Abstract.....	13
COVID impact statement	14
Chapter 1 Introduction to cancer and drugs	15
1.1 Cancer	15
1.1.1 Background	15
1.1.2 Cancer stages and grading.....	15
1.1.3 Characteristics of cancer cells	16
1.1.4 Childhood Cancer, Statistics, and survival rate.....	19
1.1.5 Treatment for childhood cancer.....	21
1.2 Rhabdoid tumour	23
1.2.1 Background	23
1.2.2 Histology of rhabdoid tumour cells.....	23
1.2.3 Extracranial RTs	24
1.2.4 Causes of Rhabdoid Tumours.....	30
1.2.5 The prevalence and incidence relating to Rhabdoid Tumours.....	31
1.2.6 Prognosis and Survival.....	32
1.2.7 Treatments.....	32
1.3 Blood Brain Barrier.....	36
1.3.1 Background	36
1.3.2 Cells and the Blood Brain Barrier	36
1.3.3 Methods & strategies for crossing the Blood Brain Barrier	38
1.4 Drug repurposing	42
1.4.1 Background	42
1.4.2 Traditional Drug Development vs Drug Repurposing.....	42
1.4.3 Activity based and in-silico based drug repurposing	45
1.4.4 Examples of repositioned drugs.....	46
1.4.5 Drugs repurposed in this research project.....	47

Chapter 2 Introduction to experimental techniques.....	51
2.1 Cell culture	51
2.1.1 Background	51
2.1.2 Advantages and disadvantages of cell culture	52
2.2 Cytotoxicity assay.....	53
2.3 Fourier transform infrared spectroscopy	55
2.3.1 Background	55
2.3.2 Spectral band analysis	55
2.3.3 Advantages and applications in cancer.....	58
Chapter 3 Introduction to lipid membranes and modelling	60
3.1 Cell membranes	60
3.1.1 Background	60
3.1.2 Asymmetry and lipid content of normal vs cancer lipid membranes	61
3.1.3 Membrane fluidity alteration in the cancer membrane.....	62
3.2 Molecular Dynamics Simulation	65
3.2.1 Background and theory	65
3.2.2 Overview of membrane models.....	68
3.2.3 Lipid choice and membrane compositions in this project.....	69
3.2.4 Molecular dynamics software	72
Chapter 4 Aim and Objectives.....	73
4.1 Aims.....	73
4.2 Objectives	73
Chapter 5 Methodology.....	74
5.1 Experimental Methodology	74
5.1.1 Aseptic techniques	74
5.1.2 Chemicals	74
5.1.3 Cell culture and drug treatment.....	74
5.1.4 Analysis	75
5.2 Computational Methodology	76
5.2.1 Model systems composition	76
5.2.2 Model system setup	77
5.2.3 Simulation steps and parameters	78

5.2.4 Analysis	80
Chapter 6 Results and Discussion.....	81
6.1 Experimental Results & Discussion	81
6.1.1 MTT assay analysis	81
6.1.2 Drug combination analysis, CalcuSyn	85
6.2 Computational Results & Discussion.....	90
6.2.1 Membrane model system visualisation	90
6.2.2 Area per lipid (APL).....	95
6.2.3 Area compressibility modulus.....	102
6.2.4 Lipid tail order parameters.....	106
6.2.5 Mass density & membrane thickness	111
6.2.6 Hydrogen bonds.....	117
6.2.7 Discussion of drug-membrane interactions.....	121
6.2.8 Discussion of lipid phases and lipid rafts	123
Chapter 7 Conclusion.....	126
References	129

List of tables

Table 1. Typical wavenumber assignments of the specific functional groups associated with various biological molecules.....	57
Table 2. Lipid compositions of the membrane and drug systems investigated.	77
Table 3. Different IC50 values achieved in literature for carvacrol and loratadine across different cell lines.	84
Table 4. Combination index values, symbols they are associated with and the descriptions for classification of synergism or antagonism (Bijnsdorp et al., 2011).	86
Table 5. CalcuSyn output for the combination of carvacrol and loratadine.....	87
Table 6. CalcuSyn output for the combination of carvacrol and loratadine.....	88
Table 7. Area compressibility modulus of the cancer and healthy membrane models before and after the addition of drugs.	105

List of figures

Figure 1. Outline of the hallmarks of cancer (Adapted from Hanahan & Weinberg, 2011). ..	16
Figure 2. Log incidence per million for childhood cancers (0-5 years old) between 1988 to 2008, acute lymphoblastic leukaemia, neuroblastoma and hepatoblastoma in parts of America and Asia (Hubbard et al., 2019).....	20
Figure 3. Rhabdoid tumour cells histology. (a) Rhabdoid tumour cells (b) The magnified image here shows that rhabdoid tumour cells are polygonal cells consisting of an eosinophilic cytoplasm and a large- nuclei. The eosinophilic inclusions, which are quite large and round in shape, reside in the cytoplasm, and this causes the nucleus to become pushed to the side (Shokripour et al., 2017).....	23
Figure 4. Rhabdoid Tumour of the kidney found in a 15-month-old female patient. The RT here is seen at the centre of the kidney and involving the renal hilum as shown by the black arrow. Subcapsular hematoma is also present which was proven at the surgery. This image has been adapted from Chung et al. (1995).	25
Figure 5. Rhabdoid tumour of the kidney present in a male infant about 18 months old in the right kidney. The black arrow shows the crescent shaped collection which has the attenuation	

of fluid, white arrows outline the tumour nodules which in presentation appear lobular (Agrons et al., 1997). 25

Figure 6. Rhabdoid tumour of the kidney present in a 4-day old child in the left kidney. This scannographic section here shows a large, lobulated mass found at the centre of the left kidney as shown by the arrow. This image has been adapted from Trabelsi et al. (2016). ... 26

Figure 7. Rhabdoid tumour of the neck discovered in a 9-month-old female. The CT scan shows a large mass located on the right side of the neck which has dislocated the trachea (Stevic et al., 2016). 27

Figure 8. Malignant rhabdoid tumour of the liver shown by the black arrow found in an 8-month-old boy. This image has been adapted from Oita et al. (2015). 28

Figure 9. The Tentorium Cerebelli of the brain. The brown highlights the supratentorial section above the tentorium (red) where atypical teratoid rhabdoid tumours can be found but is uncommon. The yellow highlights the infratentorial section found below the tentorium where atypical teratoid rhabdoid tumours are mainly located within the brain and the grey is the spinal cord. Adapted and modified from Wu et al. (2016). 29

Figure 10. ATRT which was found present in the temporal lobe, indicated by the black arrow, of a 4-year-old boy. This image has been adapted from Shokripour et al. (2017). 30

Figure 11. Schematic diagram showing the cross-section of the different components which make up the blood brain barrier (Di et al., 2008). 37

Figure 12. Only about 2% of the possible drugs which are discovered are actually able to pass the BBB (Di et al., 2008). 38

Figure 13. Steps for traditional drug development. Adapted and modified from the authors Xue et al. (2018) as well as Lombardino and Lowe (2004). 44

Figure 14. Steps involved in drug repositioning. Adapted and modified from Xue et al. (2018). 45

Figure 15. (a) Chemical structure of carvacrol (Yin et al., 2012) (b) thyme (left) and oregano (right) aromatic plants (Marshall, 2021). 47

Figure 16. Chemical structure loratadine (Lovskaya & Menshutina, 2020). 49

Figure 17. (a) An example of our adherent A204 cells under the microscope. (b) Example of suspension K562 parental cells (Baykal-Köse et al., 2020). 51

Figure 18. Cell viability MTT assay done on A204 cells in the presence of a control (cell culture medium), cisplatin, loratadine and carvacrol. 54

Figure 19. Schematic illustration of the process of Fourier transform infrared (FTIR) (Mohamed et al., 2017).....	55
Figure 20. A biological spectrum with the typical peak assignments associated with biological molecules, ranging from 3000 – 800 cm ⁻¹ (Modified from Baker et al., 2014).	57
Figure 21. Spectra achieved for lung cancer and normal sputum whereby the significant peaks are labelled A-F (Modified from Lewis et al., 2010).	59
Figure 22. Simple schematic which shows the basic structure of a lipid bilayer (Bernardino de la Serna et al., 2016).....	60
Figure 23. Lipid membrane compositions of a healthy and cancer cellular membrane. The extracellular pH levels for both cell membranes are also reported (Alves et al., 2016).	62
Figure 24. Summary of the overall interactions which take place within or between a molecule (Notman & Anwar, 2013).	67
Figure 25. Composition of the main mammalian lipids (van Meer & de Kroon, 2011).	70
Figure 26. The chemical structures of the specific lipids which have been used for the simulations in this research project. (a) POPC (b) PSM (c) Cholesterol (Bunge et al., 2008). For both POPC and PSM sn-1 and sn-2 are used to refer to tail 1 and tail 2, respectively.....	72
Figure 27. Simulation steps taken for each mixed membrane system.....	79
Figure 28. Cytotoxic effect and IC ₅₀ value obtained of cisplatin against the A204 cell line....	82
Figure 29. The cytotoxic effects and IC ₅₀ value achieved for (a) carvacrol and (b) loratadine against the A204 RT cell line are presented in the cell viability graph.	83
Figure 30. (a) Dose-effect curve analysis and (b) median-effect plot analysis for assessing the drug combination effect. These have been obtained using the CalcuSyn software.	87
Figure 31. Isobologram plot for assessing the drug combination effect between carvacrol (CAR) and loratadine (LOR). This has been obtained using the CalcuSyn software.	88
Figure 32. (a) Cancer (flexible) membrane with the addition of 16 carvacrol molecules (magenta purple molecules), the water phase is found as red lines above and below the lipid bilayer. In each membrane system the POPC lipids are shown by grey lines, PSM – by royal blue lines and cholesterol – by the bright green lines. The blue, brown, and red large balls represent nitrogen (N), phosphorus (P) and oxygen (O) from the lipid head groups. (b) The different X-Y-Z planes of a modelled system are shown. These images were obtained using the VMD software package.	90

Figure 33. Snapshots of the fully simulated (a) flexible cancer, (b) rigid healthy and (c) intermediate healthy membrane bilayer systems before the addition of any drugs. These fully equilibrated systems were configured after 200 ns of MD production run. The images were obtained using the VMD software package. 91

Figure 34. Snapshots of the fully simulated flexible cancer bilayer with the addition of 8 carvacrol (magenta purple) molecules are shown with; (a) presenting the initial configuration with carvacrol molecules randomly placed in the water phase; (b) showing the configuration after 100 ns of MD production run; and with (c) showing the configuration after 200 ns of MD production run. These images were obtained using the VMD software package..... 91

Figure 35. Snapshots of the fully simulated flexible cancer bilayer with the addition of carvacrol (magenta purple) molecules and loratadine (black) molecules are shown with; (a) The configuration with 16 carvacrol molecules after 200 ns of MD production run; (b) shows the configuration after 350 ns of MD production run for the addition of 8 loratadine molecules to the bilayer; and (c) presents the configuration after 350 ns of MD production run, for the combination of 16 carvacrol molecules with 8 loratadine molecules added in this membrane. These images were obtained using the VMD software package..... 92

Figure 36. Snapshots of the fully simulated healthy rigid bilayer after the addition of carvacrol (magenta purple) and loratadine (black) molecules. (a) The configuration with 8 carvacrol molecules after 200 ns of MD production run; (b) shows the configuration after 200 ns of MD production run for the addition of 16 carvacrol molecules to the bilayer; (c) the configuration of the membrane with the addition of 8 loratadine molecules after 200 ns of MD production run, and (d) presents the configuration after 350 ns of MD production run, for the combination of 16 carvacrol molecules with 8 loratadine molecules added in this membrane. These images were obtained using the VMD software package..... 93

Figure 37. Snapshots of the fully simulated healthy intermediate bilayer after the addition of carvacrol (magenta purple) and loratadine (black) molecules. (a) The configuration with 8 carvacrol molecules after 200 ns of MD production run; (b) shows the configuration of the membrane after 400 ns of MD production run for the addition of 16 carvacrol molecules to the bilayer; (c) the configuration of the membrane with the addition of 8 loratadine molecules after 200 ns of MD production run, and (d) presents the configuration after 350 ns of MD production run, for the combination of 16 carvacrol molecules with 8 loratadine molecules added in this membrane. These images were obtained using the VMD software package. . 94

Figure 38. Area per lipid achieved for the mixed membrane systems without the addition of drugs. The black line represents the cancer membrane, purple line represents the healthy intermediate membrane, and the pink line represents the healthy rigid membrane. Each 50,000 ps (50 ns) simulation represents a single MD simulation block. 96

Figure 39. (a) Area per lipid results of single lipid membrane systems (DOPC, POPC, DPPC, PSM and Cholesterol) as well as mixed lipid membrane systems representing a cancer and healthy model membrane (Hopton, 2019). (b) Area per lipid of mono-lipid membranes (POPC, PSM and Cholesterol) and mixed lipid membrane systems (Cancer, Healthy – intermediate and Healthy – rigid) (Ahmed Irfan, 2020). 98

Figure 40. Area per lipid of each membrane system after the addition of carvacrol, loratadine. (a) Cancer, healthy rigid and healthy intermediate membrane systems with the addition of 8 carvacrol molecules. (b) Cancer, healthy rigid and healthy intermediate membrane systems with the addition of 16 carvacrol molecules. (c) Cancer, healthy rigid and healthy intermediate membrane systems with the addition of 8 loratadine molecules. (d) Cancer, healthy rigid and healthy intermediate membrane systems with the addition of 16 carvacrol and 8 loratadine molecules in combination. Each 50,000 ps (50 ns) simulation represents a single MD simulation block. 100

Figure 41. Area per lipid of the ceramide with and without the addition of increasing concentrations of menthol molecules. S0 represents the pure ceramide membrane (blue line), S16 represents the ceramide membrane with 16 menthol molecules (red line), S32 is for the ceramide membrane with 32 menthol molecules (green line) and S64 shows the ceramide membrane with 64 menthol molecules (Wang & Meng, 2017). 102

Figure 42. Average compressibility modulus achieved for the cancer, healthy rigid and healthy intermediate membrane systems. 105

Figure 43. POPC and PSM lipid tail order parameters for the cancer membrane whereby (a) is representing the POPC sn-1 tail and (b) is for the POPC sn-2 tail. (c) Represents the tail order for the PSM sn-1 tail while (d) is representative of PSM sn-2 tail. 107

Figure 44. POPC and PSM lipid tail order parameters for the healthy rigid membrane whereby (a) is representing the POPC sn-1 tail and (b) is for the POPC sn-2 tail. (c) Represents the tail order for the PSM sn-1 tail while (d) is representative of PSM sn-2 tail. 108

Figure 45. POPC and PSM lipid tail order parameters for the healthy intermediate membrane whereby (a) is representing the POPC sn-1 tail and (b) is for the POPC sn-2 tail. (c) Represents the tail order for the PSM sn-1 tail while (d) is representative of PSM sn-2 tail. 109

Figure 46. Mass density profiles of the cancer membrane after the addition carvacrol and loratadine molecules. (a) The complete mass density profile for the addition of 8 carvacrol molecules consisting of the lipids POPC, PSM and CHOL which are red, light blue and orange lines. The dark blue line represents the head groups of the lipids, the membrane is brown, water is green, and the magenta purple line signifies carvacrol. (b) Same 8 carvacrol molecules mass density profile but this only contains the dark blue line which represents the head groups of the lipids and the magenta purple line to show carvacrol, all other components are omitted. (c) Profile for the addition of 16 carvacrol molecules. (d) Profile for the addition of 8 loratadine molecules. (e) Profile for the combination of 16 carvacrol with 8 loratadine molecules. For profiles (b) to (e) the scale of the graphs was increased for better visibility of the results. All mass density profiles were symmetrised. 112

Figure 47. Mass density profiles of the healthy rigid membrane after the addition of (a) 8 carvacrol molecules, (b) 16 carvacrol molecules, (c) 8 loratadine molecules and (d) the combination of 16 carvacrol with 8 loratadine molecules. 113

Figure 48. Mass density profiles of the healthy intermediate membrane after the addition of (a) 8 carvacrol molecules, (b) 16 carvacrol molecules, (c) 8 loratadine molecules and (d) the combination of 16 carvacrol with 8 loratadine molecules. 115

Figure 49. Average membrane thickness for each membrane system before and after the addition of carvacrol and loratadine. 116

Figure 50. The number of hydrogen bonds formed between the lipids (Membrane-Membrane), between the water and the lipid membrane (Water-Membrane) and total hydrogen bonds formed in the membrane (Total Membrane) before any drugs were added to the cancer and healthy membrane systems. 118

Figure 51. Total number of hydrogen bonds which are formed in the cancer and healthy membrane systems, per lipid for no drugs, 8 and 16 carvacrol molecules, 8 loratadine molecules and for the combination of both drugs. 119

Figure 52. Number of hydrogen bonds formed after the addition of carvacrol and loratadine (a) with the water molecules and (b) with the membrane lipids. 120

Figure 53. Mapping the lipid composition of the membranes used in this research into the ternary phase diagram for POPC/PSM/CHOL system at 37 °C. The composition for cancer (flexible) membrane is shown as black square, the composition for normal (rigid) membrane is shown as pink square, and the composition for normal (intermediate) membrane is shown as purple square in the middle. The red dashed lines show the lipid mol %. The image is adapted from De Almeida et al. (2003). 124

Acknowledgements

First and foremost, I would like to praise Allah (swt) for bestowing this opportunity upon me and His guidance and support throughout my study.

I will forever be grateful to my wonderful supervisor, Dr. Anna Akinshina who has provided me with great guidance during my time doing a MSc by research. I would like to especially thank Rumana Rafiq, Dr Muna Abubaker and all the staff and students of Translational medicine who have helped and supported me through my lab work without hesitation. I would also like to take this opportunity to thank the School of Science, Engineering and Environment at the University of Salford for giving me this research opportunity as well as Kidscan Children's Cancer Research for the partial funding to this project. Also, I am very appreciative to the University of Manchester thank you for giving me the opportunity to collaborate on my research project even though my time was cut short due to COVID-19 and could not be completed. Thank you to Newcastle University for gifting us the A204 cells. A huge thank you to Kiran Ahmed Irfan, who has aided me in both my computational and experimental work, thank you for your patience with me. My family and friends, thank you for your unwavering support for me always.

Abbreviations

CHARMM-GUI	Chemistry at HARvard Macromolecular Mechanics-Graphical User Interface
CHOL	Cholesterol
DMSO	Dimethyl sulfoxide
GROMACS	GRONingen MACHine for Chemical Simulation
MD	Molecular dynamics
MTT	(3-(4,5-dimethylthiazol-2-yl)-2,5-diphenyltetrazolium bromide)
POPC	1-palmitoyl-2-oleoyl-sn-glycero-3-phosphocholine
PSM	Palmitoylsphingomyelin
RT	Rhabdoid tumours
VMD	Visual Molecular Dynamics

Abstract

Rhabdoid tumours (RT) are a rare form of childhood cancer which is known to affect infants under the age of 1 year. Survival rate is a major problem with only 31% of those who are diagnosed living to 1 years old. In this research extracranial RT from the A204 cell line was investigated for its interaction with the drugs loratadine and carvacrol. Drug-cell interactions were probed at a single cell level and biological changes within the cell were monitored experimentally through the cell viability MTT assay. Biological changes were also monitored computationally using molecular dynamics (MD) simulations. Three models for cell membranes were proposed, one model for cancer membrane and two models for healthy membranes. All models comprise three lipid types, the most abundant in cell plasma membranes, 1-Palmitoyl-2-oleoylphosphatidylcholine (POPC), palmitoylsphingomyelin (PSM) and cholesterol (CHOL) with different compositions. Results of the experimental MTT assays showed that while both loratadine and carvacrol are cytotoxic against the A204 cells, loratadine produced the greater cytotoxic effect. Additionally, the drugs produced a synergistic effect when they were used in combination. MD simulation results have shown that individually both drugs permeate the flexible cancer membrane and not the rigid healthy membrane. Similar results are found when used in combination as both drugs again permeate the cancer membrane and not the rigid healthy membrane. Area per lipid increased when drugs permeated the membrane, while no change was found when the drugs did not permeate the membrane. Changes were also detected in relation to tail order of the cancer membrane possibly due to its overall disordered structure resulting in higher flexibility and permeability to the drugs, while the rigid healthy membrane did not allow permeation of drugs. These findings suggest and reiterate the potential benefits of using non-cancer drugs for the treatment of childhood RT.

COVID impact statement

As a result of the coronavirus lockdowns and restrictions which were put in place, we were unable to complete some of the planned experimental work for this research project. We had originally planned to collaborate with The University of Manchester to investigate and monitor the biological changes within the A204 cells before and after the addition of carvacrol and loratadine using Fourier transform infrared spectroscopy. Although this was terminated without data due to the travel restrictions and limited access to labs. This would have allowed us to examine the spectral signatures produced by each drug as well as look for additional features indicating synergistic action when drugs are used in combination on the A204 cells.

Chapter 1 Introduction to cancer and drugs

1.1 Cancer

1.1.1 Background

Cancer is a term which is frequently used to describe a plethora of different diseases. Cancer can start anywhere in the body. Cells can grow and divide to form new cells and when the cells get damaged, they die, and new cells are there in order to take their place, the cell cycle. Feitelson et al. (2015) describes that this process is controlled in a number of ways including growth factors, hormones and using signalling pathways and therefore when this process becomes fragmented cancer develops. In the case of cancer, the damaged cells end up surviving and mutating which produces new cells, though they are not needed, and these extra cells can divide uncontrollably resulting in tumour (mass of cells) growth (Otto & Sicinski, 2017). These cells are able to supersede the apoptotic pathways and further promote the survival of proliferative pathways (Feitelson et al., 2015).

Tumours can be classified as either benign or malignant. Tumours that are benign are non-cancerous, stay in their primary location, have a slow growth rate and do not spread to other parts of the body for example, fibroids, adenoma and lipoma (Adams & Morgan, 2019; Patel, 2020). Tumours which are malignant spread into other tissues and areas within the body. These tumour cells can metastasise by breaking off and invading other parts of the body spreading further away from where the original primary tumour had started (Seyfried & Huysentruyt, 2013). Popper (2016), has reported that when lung cancer metastasises, it is able to spread to the brain and liver especially in the case of small cell lung cancer and adenocarcinoma. Though, the cancer is still named according to its original primary site of origin. Some cancers such as leukaemia do not form solid tumours. Instead it is a cancer originating in the blood and bone marrow due to the accumulation of lymphoid cells, more specifically in the case of acute lymphoblastic leukaemia (Terwilliger & Abdul-Hay, 2017).

1.1.2 Cancer stages and grading

Staging and grading is important as it is used to describe cancer in order to aid doctors to determine the best course of action to undertake when it comes to treatment for the patient. There are two common staging systems which have been used to describe the stages of

cancer: the tumour-node-metastasis (TNM) system and a numbering system (Brierley et al., 2016; Brierley et al., 2019; Greene & Sobin, 2008).

In TNM, T specifically expresses the primary tumour size and how far it has spread to the tissue and structures closest to it. The N outlines details of whether the tumour has spread to the lymph nodes while M refers to whether the cancer has spread to other parts of the body so cancers originating in the lungs spreading to the liver (Brierley et al., 2016). The numbering system, depending on the cancer, can consist of three to four stages usually written as roman numerals. Stage I is used to describe an early cancer which has not spread, while those with stage IV cancer are less likely to recover and it has spread to other organs (Greene & Sobin, 2008).

1.1.3 Characteristics of cancer cells

There are six unique characteristics of cancer cells which are defined as the hallmarks of cancer as shown in Figure 1 below. In the papers by Zalba and ten Hagen (2017) and Hanahan and Weinberg (2011), the authors have noted that these include, “sustaining proliferative signalling, evading growth suppressors, resisting cell death, enabling replicative immortality, inducing angiogenesis, activating invasion and metastasis.”

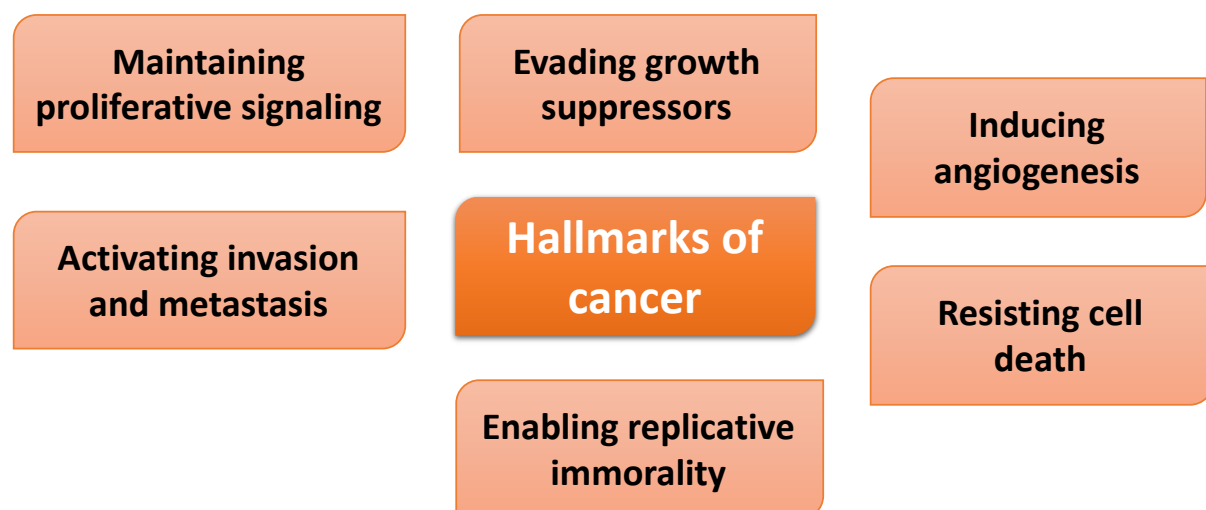


Figure 1. Outline of the hallmarks of cancer (Adapted from Hanahan & Weinberg, 2011).

1.1.3.1 Sustaining proliferative signalling

Normal healthy cells, which contain receptors at their surface, use growth factor signalling to tightly control the growth and division of cells. The growth and proliferative signalling pathways are altered allowing the cancer cells to become independent and maintain proliferation signals allowing them to continue surviving (Fouad & Aanei, 2017; Gutschner & Diederichs, 2012). These cancer cells become independent as a result of many factors including the production of their own growth receptor factors, producing paracrine signals which are used to stimulate normal, tumour-associated cells further supplying the cancer cells with growth factors (Gutschner & Diederichs, 2012; Hanahan & Weinberg, 2011). Furthermore, while in normal cells there are only limited amounts of growth factor ligands, in cancer cells these may be elevated resulting in them becoming hyperresponsive. Moreover, the activation of downstream signalling pathways leads to cancer cells becoming independent from the exogenous growth factor receptors (Gutschner & Diederichs, 2012; Hanahan & Weinberg, 2011).

1.1.3.2 Evading growth suppressors

Cancer cells are able to overcome the anti-growth signals which are dependent on tumour suppressor genes, allowing them to continue growing and proliferating. Activation of the tumour suppressor genes: TP53, PTEN and RB results in apoptosis in the healthy cells and cancer cells can prevent this activation taking place (Gutschner & Diederichs, 2012; Hanahan & Weinberg, 2011). A method in which cancer cells are able to achieve this is through multiple mutations which make the tumour suppresser genes inactive, or through the complete deletion of these genes altogether as described by Gutschner and Diederichs (2012).

1.1.3.3 Resisting cell death

Apoptosis, also referred to as programmed cell death, is an important natural and selective process used to kill off cells which are no longer needed, and this is a barrier which is overridden by the cancer cells (Pfeffer & Singh, 2018; Wong, 2011). Apoptosis uses caspases to implement cell death and the activation of these caspases occurs via two main pathways: the intrinsic (mitochondrial) pathway occurring inside the cell and the extrinsic (death receptor) pathway occurring outside the cell. There are two types of caspases, which are used

to cut the target protein for apoptosis to occur, the initiator caspases (2, 8, 9 and 10) which initiate the apoptosis and executioner caspases (3, 6, 7) which actually execute apoptosis. The intrinsic pathway can be triggered as a result of hypoxia (one of many factors) leading to an increase in the mitochondrial permeability and this can cause pro-apoptotic molecules to be released hence causing cell death. The extrinsic pathway uses death ligands (extracellular cell death signals) which bind to a death receptor, allowing a linking site to be formed for an adapter protein. This complex which has been formed assembles and activates the initiator caspases for apoptosis to occur (Pfeffer & Singh, 2018; Wong, 2011).

Cancer cells have mutations and use many anti-apoptotic mechanisms to achieve this evasion of cell death instead of evasion through a single pathway, including increased levels of anti-apoptotic regulators and the downregulation of the pro-apoptotic pathway (Fernald & Kurokawa, 2013; Hanahan & Weinberg, 2011). These anti-apoptotic regulators, which include the BCL-2 proteins from the B-cell lymphoma-2 family of proteins, work by preventing the upregulation of pro-apoptotic proteins, BCL-2-associated X protein (BAX) and the BCL-2 homologous antagonist killer (BAK), particularly for the intrinsic pathway leading to the avoidance of cell death and this is seen in many different cancers (Pfeffer & Singh, 2018).

1.1.3.4 Enabling replicative immortality

Normal healthy cells are only able to go through the cell growth and division cycle a few times as a result of the barriers, senescence and crisis. Senescence is when the cells enter a non-proliferative state which is irreversible while crisis refers to the cell death (Gutschner & Diederichs, 2012; Hanahan & Weinberg, 2011). Cancer cells, on the other hand, overcome these and emerge free from these barriers, displaying unlimited replication also referred to as immortalisation (Gutschner & Diederichs, 2012; Hanahan & Weinberg, 2011).

1.1.3.5 Inducing angiogenesis

Cells require oxygen and various nutrients from surrounding blood vessels in order to grow and survive. This is normally restricted which limits the size and growth of the cells but as cancer cells are able to induce angiogenesis; this means they are able to form new blood vessels from those which already exist. As a result, this allows cancer cells to have their own

supply of oxygen and nutrients, as well as getting rid of their waste and start to metastasise to spread the cancer (Gutschner & Diederichs, 2012; Hanahan & Weinberg, 2011; Rajabi & Mousa, 2017).

1.1.3.6 Activating invasion and metastasis

Biological changes result in the invasion and metastasis cascade in cancer cells. Metastasis means that the primary tumour has spread to other organs and tissues in the body (Seyfried & Huysentruyt, 2013). This cascade allows cancer cells to invade the healthy tissues and then continue with the intravasation into the blood and lymphatic vessels. Extravasation occurs as the cancer cells escape from the vessels to invade their target tissues and organs, to form additional secondary tumours, from small nodules signifying growth of abnormal tissue, to macroscopic tumours (Gutschner & Diederichs, 2012; Hanahan & Weinberg, 2011; Stuelten et al., 2018). Wang et al. (2017) have reported that cancer cells are also able to hide and evade from the immune system with the help of two types of T cells which further allows them to not be removed from the body. The CD4⁺ T cells which are T helper cells and the CD8⁺ T cells are the cytotoxic T cells.

1.1.4 Childhood Cancer, Statistics, and survival rate

One form in which death occurs in children and adolescents is through cancer. In 2019 it was estimated that in the United States (US) alone there were 11,060 new cases of cancer diagnosed in children and adolescents as reported by Siegel et al. (2019). In 2020, this figure reduced by 10, hence it was estimated that there would be 11,050 cases of children diagnosed with cancer in another report by Siegel et al. (2020). These cancer diagnosis in children were from birth up to the age of 14 years old and from this approximately 1,190 children were expected to die from the disease both in 2019 and 2020 (Siegel et al., 2019, 2020). Furthermore, gender differences exist within childhood cancers as males are more likely to get cancer than females at a ratio of 6:5. Males are more prone to lymphomas, carcinomas and melanomas while females have higher incidence of thyroid carcinoma and leukaemia (Dorak & Karpuzoglu, 2012).

Survival rate for childhood cancer has notably improved over the past decades. In the analysis by Hubbard et al. (2019), the authors extracted data for about 25 years' worth of childhood

cancer incidence occurring between 1988 to 2012 internationally. They found that over those 25 years the incidence for cancers such as leukaemia, neuroblastoma and hepatoblastoma had shown slight increase in many regions including America and Asia as shown in Figure 2. Though this has been the case, Siegel et al. (2019), have reported that for the most common childhood cancer, leukaemia, there has been a 78% decline in deaths as well as increased remission rates of 90% to almost 100% for those with childhood acute lymphocytic leukaemia.

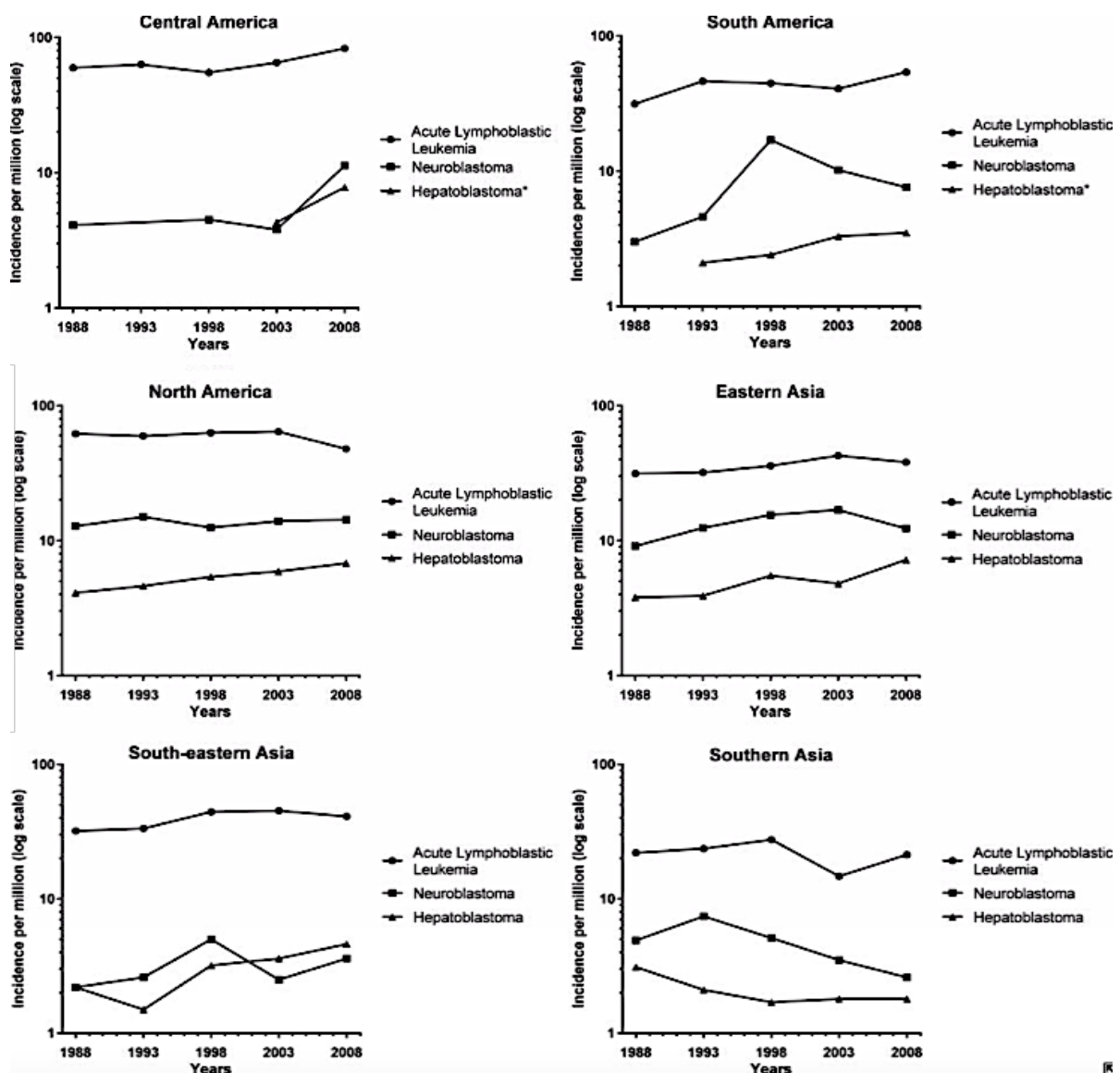


Figure 2. Log incidence per million for childhood cancers (0-5 years old) between 1988 to 2008, acute lymphoblastic leukaemia, neuroblastoma and hepatoblastoma in parts of America and Asia (Hubbard et al., 2019).

1.1.5 Treatment for childhood cancer

There are many types of treatments that exist for cancer patients, though the treatment that each individual child receives can vary depending on many factors. The main factors are the type of cancer they have and how advanced it is. Multimodal therapies are popular and commonly used where the different types of cancer treatments are used in conjunction with each other, i.e. using chemotherapy along with radiation therapy (Saletta et al., 2014) which could lead to increased therapeutic efficacy.

For many solid tumour cancers, the first line of treatment option to be considered would be surgery. This allows much of the tumour to be removed without damaging the neighbouring healthy cells. Chemotherapeutic/anticancer drugs target cancer cells and promote the onset of cell death through different mechanisms of action (Alves et al., 2016). Anticancer drugs such as cisplatin work by inhibiting the DNA synthesis and cell division of the cancer cells, which has been described in the review article by Fuertes et al. (2003). Another class of chemotherapeutics includes anthracyclines which are known to be very potent and work by intercalating themselves in the DNA and RNA base pairs which inhibits DNA/RNA synthesis leading to cell death (Minotti et al., 2004). Radiation therapy is a highly useful and successful treatment method which uses radiation in order to shrink and eradicate the cancerous cells (Jairam et al., 2013).

Although a vast range of cancer treatments already exist and developing new techniques may seem futile, the reality is that many of these treatments are actually far from child friendly. Treatments like chemotherapy and radiation therapy in particular tend to be aggressive and highly toxic to young children which can result in many short- and long-term effects even if they provide better cure rates and higher morbidity (Askins & Moore, 2008). While these treatments do destroy the cancerous cells, they also affect and destroy the healthy cells and tissues nearby leading to severe late side effects in the growth and development of children as well as other abnormalities (Jairam et al., 2013). In a study by Duffner et al. (2014) the combination of polychemotherapy and radiation therapy for paediatric B-cell acute lymphoblastic leukaemia (ALL) patients resulted in the development of leukoencephalopathies nearly 8 years later in those who survived. In another study by Edelmann et al. (2014) on childhood ALL patients who were solely treated with chemotherapy

found that these survivors had problems associated with neurocognitive impairment. They would perform much worse when it came to processing speed, verbal selective reminding and also many problems with academics. Similar findings have also been reported for childhood brain cancer survivors (Askins & Moore, 2008). These are just some of the issues which have been highlighted in terms of childhood cancer treatments and therefore it is essential to develop treatments which leave far fewer devastating consequences long and short term in children.

1.2 Rhabdoid tumour

1.2.1 Background

Rhabdoid tumours (RT) are a highly rare form of malignant cancer, arising in early childhood in children and infants. It was not until in 1978 when RT were first recognized as their own pathological entity (Heck et al., 2013). They are able to grow anywhere in the body with their most common sites being the brain (atypical teratoid RT, ATRT) and extracranial sites being the kidneys (known as RT of the kidney, RTK), and the soft tissue (known as extrarenal RT and malignant RT) (Geller et al., 2015). These extrarenal sites where RT can be found mainly include the skin, liver and lungs but does not limit RT which have been seen in more or less all soft tissues in the body.

1.2.2 Histology of rhabdoid tumour cells

Histologically, RT consist of many distinguishing features including their large polygonal shaped cells. These cells contain an eosinophilic cytoplasm, an unconventional nuclei and nucleoli which can be with or even without fibrillary globoid inclusions (Kohashi et al., 2016; Shokripour et al., 2017). From Figure 3b, which has magnified a section of RT cells from Figure 3a, it can be seen that as the cytoplasm has the round eosinophilic inclusions, it pushes the nucleus of the cells more to the side thus a higher nucleus to cytoplasm ratio (Shokripour et al., 2017). The histology of RT cells differs from other cancers such as Hodgkin's lymphoma. Piccaluga et al. (2011) describe Hodgkin's lymphoma cells as consisting of "a large rim of cytoplasm" as well as a minimum of "two nuclei with acidophilic or amphophilic nucleoli" and these cover "more than 50% of the nuclear area".

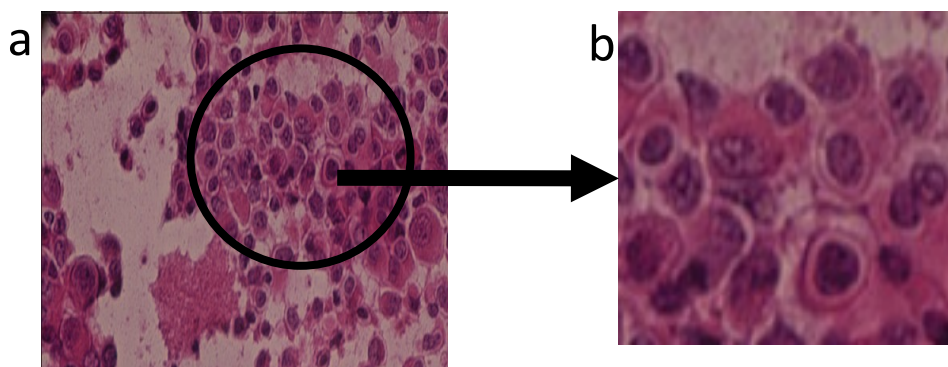


Figure 3. Rhabdoid tumour cells histology. (a) Rhabdoid tumour cells (b) The magnified image here shows that rhabdoid tumour cells are polygonal cells consisting of an eosinophilic cytoplasm and a large- nuclei. The eosinophilic inclusions, which are quite large and round in

shape, reside in the cytoplasm, and this causes the nucleus to become pushed to the side (Shokripour et al., 2017).

1.2.3 Extracranial RTs

1.2.3.1 Rhabdoid tumours of the kidney and case studies

RTK was the first to be identified in 1978 as stated in the papers by Heck et al. (2013) and Nesvick et al. (2018). In the early days CT (computed tomography) scans were used as a tool to commonly identify the characteristics associated with RTK (Agrons et al., 1997; Chung et al., 1995). The study by Chung et al. (1995), using a GE 9800 CT scanner, found that RTK, a large and heterogenous mass, was predominantly at the centre within the kidney and also included the hilum. The hilum is the border found on the kidney and it is the gateway for some structures of the kidney including the blood vessels and nerves (Treuting & Kowalewska, 2012). This was the main finding of the location of the tumour within the kidney examined across all 8 cases of children who were new-born up to the age of 13. The CT scan of a 15-month-old female by Chung et al. (1995) is also presented in Figure 4 to further reiterate this finding. As well as this, the other characteristics, which suggested a RTK present, identified by Chung et al. (1995) from the CT scans include calcification and subcapsular hematoma.

Calcification is a characteristic which has been mainly reported in RTs and it is seen if there are hyperdense areas observed on the non-contrast CT scans of the kidneys. Chung et al. (1995) found calcification in the case of 2 out of the 4 tumours on the non-contrast CT scans. Subcapsular hematoma was seen in more than half the children and it is the hypodense collections detected on the CT scans (Chung et al., 1995).

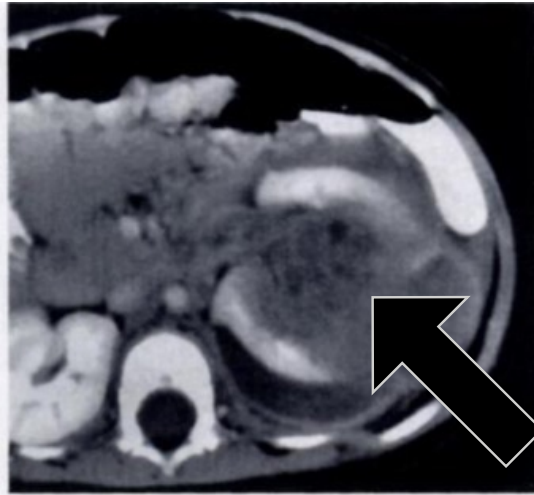


Figure 4. Rhabdoid Tumour of the kidney found in a 15-month-old female patient. The RT here is seen at the centre of the kidney and involving the renal hilum as shown by the black arrow. Subcapsular hematoma is also present which was proven at the surgery. This image has been adapted from Chung et al. (1995).

In the study by Agrons et al. (1997), 21 cases of children (new-born to 36 months old, 13 males and 8 females) who had RTK were investigated using CT technology. It was found that the main characteristic associated with RTK included “a peripheral crescent with the attenuation of fluid” which is also shown in Figure 5 by the black arrow. Figure 5 also highlights the solid lobular tumour nodules as shown by the white arrows above the attenuation of fluid (Agrons et al., 1997). Though they were able to compare their findings to a larger comparison group consisting of 153 patients aged 3 and younger who had solid renal masses, Agrons et al. (1997) concluded that due to the similarities in the CT scans “a peripheral crescent with the attenuation of fluid” cannot be solely used to distinguish a RTK from other solid renal tumours.

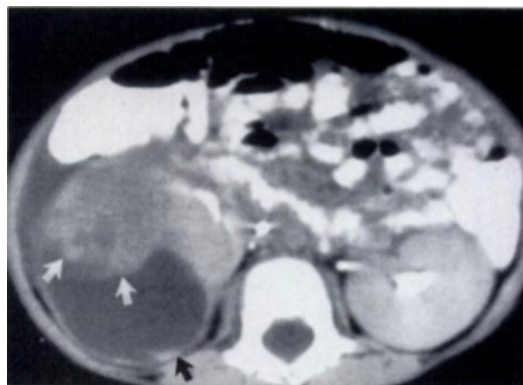


Figure 5. Rhabdoid tumour of the kidney present in a male infant about 18 months old in the right kidney. The black arrow shows the crescent shaped collection which has the attenuation

of fluid, white arrows outline the tumour nodules which in presentation appear lobular (Agrons et al., 1997).

A more recent case report by Trabelsi et al. (2016) of RTK which was identified in a 4-day old new-born child. The CT showed a large and lobulated mass, about 5 cm in size, which was found at the centre of the left kidney displayed in Figure 6, similarly to what has been previously reported in the studies by Chung et al. (1995) and Agrons et al. (1997). Furthermore, advances in diagnostic tools since the 90s has allowed better identification of the type of cancer someone has, as before not being able to distinguish between renal tumours and RTK was a problem. The histology of the cells and immunohistochemical staining was able to provide diagnostic confirmation of RTK (Trabelsi et al., 2016).

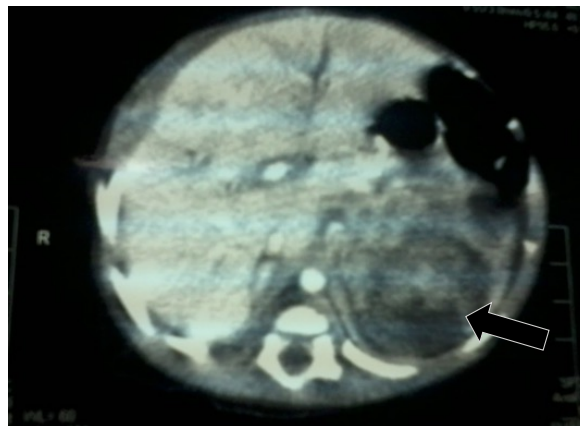


Figure 6. Rhabdoid tumour of the kidney present in a 4-day old child in the left kidney. This scannographic section here shows a large, lobulated mass found at the centre of the left kidney as shown by the arrow. This image has been adapted from Trabelsi et al. (2016).

1.2.3.2 Soft tissue, neck case study

RTs have also been found in other soft tissue areas such as the neck region (Dobbs et al., 2011). The CT scan, presented in Figure 7, of a 9-month-old female child revealed a large tumorous mass on the right side of the neck which had actually left the trachea dislocated and as a result the airway was compromised (Stevic et al., 2016). Due to these complications, monitoring airway is a colossal challenge for anaesthesiologists especially during surgery to remove the tumour (Stevic et al., 2016).

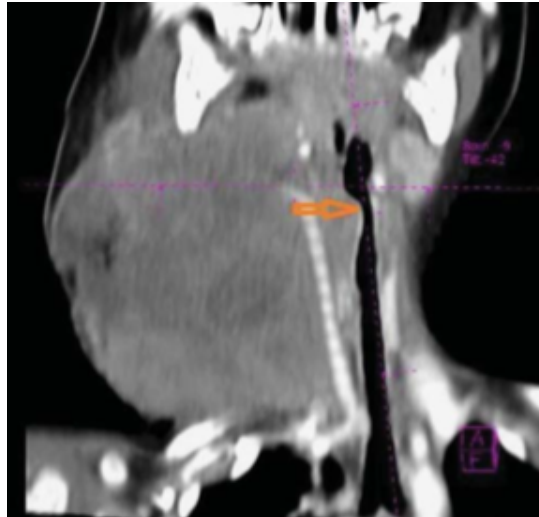


Figure 7. Rhabdoid tumour of the neck discovered in a 9-month-old female. The CT scan shows a large mass located on the right side of the neck which has dislocated the trachea (Stevic et al., 2016).

1.2.3.3 Other extracranial Rhabdoid Tumours, liver case study

Various case reports of childhood cancers have also shown the presence of RTs in the liver. In this specific case study, the RT was found on the right posterior lobe of the liver of an 8-month-old boy discovered through the CT scan as shown in Figure 8. The tumour was about 5 cm in diameter, and it was highly metastatic, and it had further spread to the lymph nodes and lungs. The characteristics of the tumour cells related strongly to the RT cells such as the large nucleoli and eosinophilic cytoplasm as well as this a positive test for vimentin from the immunohistochemical study and a negative outcome for INI1/BAF47 further aided the diagnosis as malignant RT of the liver (Oita et al., 2015). A positive test for vimentin is usually found in RTs (Gündüz et al., 1998), although it is not specifically limited just for this and therefore other techniques and tests are combined before a diagnosis is given.

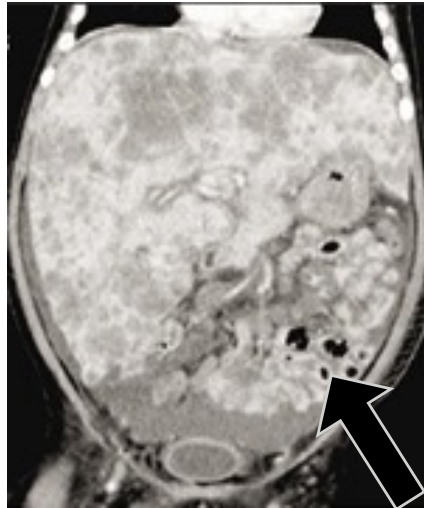


Figure 8. Malignant rhabdoid tumour of the liver shown by the black arrow found in an 8-month-old boy. This image has been adapted from Oita et al. (2015).

1.2.3.4 Atypical Teratoid Rhabdoid Tumours, background, and case study

Atypical teratoid rhabdoid tumours also known as ATRTs are defined as a malignant central nervous system (CNS) cancer found on the brain and the spinal cord. When ATRT was first discovered in 1996, it was hard to differentiate it from other embryonal brain tumours as they had a similar neuro-epithelial histology (Richardson et al., 2018). These tumours are rare, aggressive and highly malignant and because of this they are categorised as Grade IV tumours (Shokripour et al., 2017). The cranial cavity of the brain is divided into two main regions, the supratentorial and infratentorial regions (Rai et al., 2018). The cancerous cells in the ATRTs grow on the tissues of the brain so these tumours are found forming in the infratentorial region of the cerebellum or the brain stem both of which can be seen in Figure 9 located above the tentorium cerebelli. ATRT can also be found in the supratentorial region, which is below the tentorium cerebelli, however this is largely uncommon.

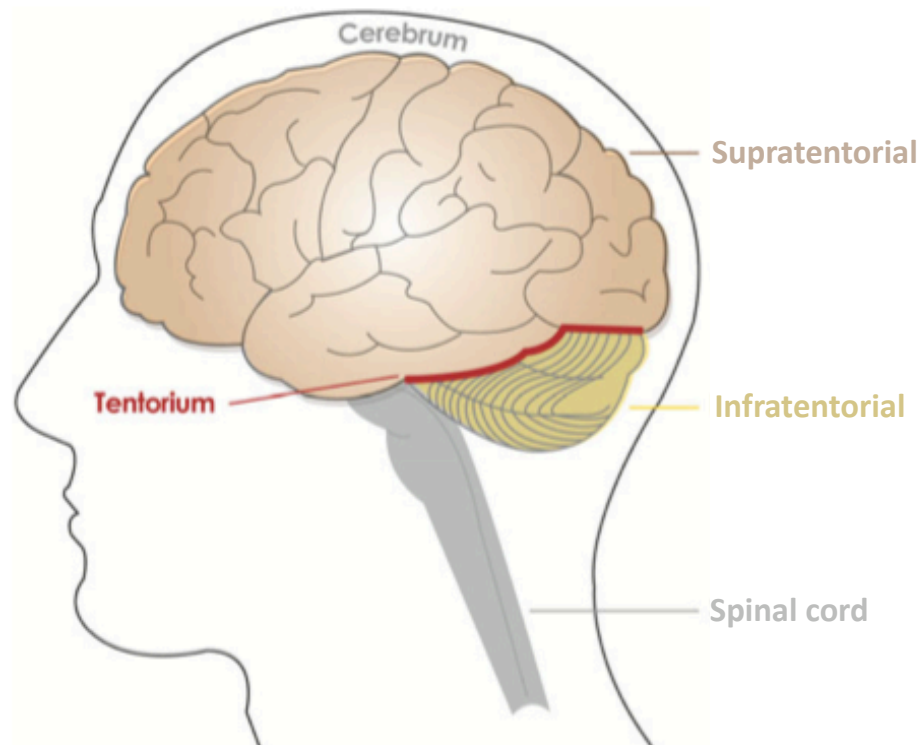


Figure 9. The Tentorium Cerebelli of the brain. The brown highlights the supratentorial section above the tentorium (red) where atypical teratoid rhabdoid tumours can be found but is uncommon. The yellow highlights the infratentorial section found below the tentorium where atypical teratoid rhabdoid tumours are mainly located within the brain and the grey is the spinal cord. Adapted and modified from Wu et al. (2016).

A case report of ATRT was identified in a 4-year-old boy. The tumour mass which was found on the temporal lobe, as seen in Figure 10, was initially misdiagnosed as anaplastic oligodendroglioma (Shokripour et al., 2017). In order to get the correct diagnosis, a section of the tumour was excised from the child and an immunohistochemical study and H&E staining was conducted on it. The results of the stain showed the tumour cells with many characteristics specifically associated with RT cells and a positive reaction for the vimentin from the immunohistochemical study further confirmed the diagnosis as ATRT (Shokripour et al., 2017).

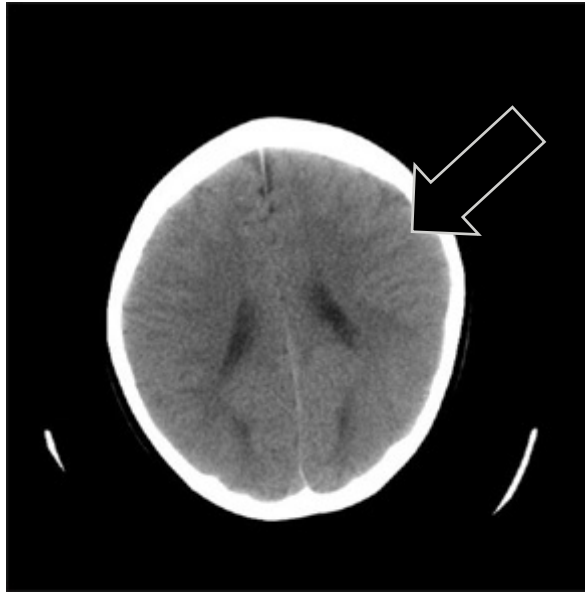


Figure 10. ATRT which was found present in the temporal lobe, indicated by the black arrow, of a 4-year-old boy. This image has been adapted from Shokripour et al. (2017).

1.2.4 Causes of Rhabdoid Tumours

RT mainly occur due to the inactivation of SMARCB1, a tumour suppressor gene (Richardson et al., 2018). A tumour suppressor gene in general is responsible for the decrease in cell division, slowing down DNA repair and telling cells when to die. When the tumour suppressor genes do not work correctly and lose their function, cells will continue to grow and divide in an uncontrollable manner, and this is what leads to cancer. The SMARCB1 gene is originally found at the 22q11.2 cytoband, a part of monosomy (chromosome) 22 (Geller et al., 2015; Shih & Koeller, 2018) , when this is translocated and deleted, it results in the formation of tumours which was identified as a genetic feature for those with RT. The SMARCB1 protein codes the hSNF5 subunit, an important component of the SWI/SNF (switch/sucrose nonfermentable) chromatin re-modelling complex, and this controls the cell division and differentiation in the normal tissues (Brennan et al., 2013; Brok et al., 2016; Richardson et al., 2018; Shih & Koeller, 2018). Therefore, the role of the SWI/SNF is to actually control the chromatin compaction and which ultimately controls the gene expression (Brennan et al., 2013). When SMARCB1 tumour suppressor gene is inactivated, it acts as a more reliable biomarker for RT cancers than solely looking at the histology of the cancer cells.

In a small cohort of patients, approximately 2 - 5% of cases, the inactivation of SMARCB1 does not occur and this is actually identified as being normal. However, the RT formation this time occurs due to the SMARCA4 subunit which is also a part of the SWI/SNF complex coding for the BRG1 subunit, and this is the gene which is inactivated (Brennan et al., 2013; Brok et al., 2016; Kram et al., 2018; Richardson et al., 2018; Shih & Koeller, 2018).

Besides the inactivation of the tumour suppressor gene, RT do not have many hallmarks/biomarkers which are related to genetic abnormalities. This suggests that the germline mutation which occurs at the SMARCB1/SMARCA4 tumour suppressor gene is reasonable enough to promote the oncogenic transformation of the normal healthy cells to cancerous cells (Brennan et al., 2013).

1.2.5 The prevalence and incidence relating to Rhabdoid Tumours

RT predominates in infants and children younger than 1 years old representing 1-2% of all childhood brain tumours (Richardson et al., 2018). Heck et al. (2013), collated records from the California Cancer Registry of diagnosis for children under the age of 6 years old occurring between 1988 to 2007. They found the risks of extracranial RTs to be greater in children who have a low birthweight, gestation (referring to the period of time for development inside the womb between conception and birth), of less than 37 weeks or more than 42 weeks or in children who are part of a multiple birth.

Those who are diagnosed can also present more than one type of primary RT. The infants and children will have a RT found not only in their central nervous system but also a RT present in their kidneys, liver or in their lungs (Geller et al., 2015). However, while the chance of getting bilateral RTs is low, bilateral Wilms tumours of the kidneys have a greater occurrence contributing to approximately 2% of the cases related to RTK (Geller et al., 2015).

Symptoms of RTs can vary depending on where the tumour is located. Some general symptoms which are identified in children with RTs includes headaches, vomiting, irritability as well as a raised region of where the tumour is such as a raised intracranial region if the RT is found in the brain (Biswas et al., 2016).

1.2.6 Prognosis and Survival

RTs are known to have a poor prognosis and consequently survival rate also decreases significantly. Survival rate is determined by 2 main prognostic factors, age of the patient and stage of the RT cancer.

RTs overall are only diagnosed at the later stages, stages III to V, this has presented a 5-year survival of up to 33% (Heck et al., 2013). More specifically, when RTs are detected early on, between stages I and III, survival rate has been reported at 41.8% which is significantly higher when compared to only 15.9% survival in those patients where RTs are discovered passed stage III. These results were seen in the National Wilms Tumour Study (NWTs), which reported 142 RT cases occurring from 1969 to 2002 and further concluded an overall survival rate at 4 years as 23.2% (Tomlinson et al., 2005). This study was also able to conclude that survival rate was far greater in children who were over the age of 2 years old (41.1%) than for those who were infants under 6 months old (8.8%).

In addition to this, the research conducted by Sultan et al. (2010) about RTs further evidenced these conclusions. The research included the data of 229 patients from the Surveillance, Epidemiology and End Results (SEER) programme in which they determined that the stage of the tumour and age are important contributors of increased survival rate.

1.2.7 Treatments

Generally, no standard therapeutic pathway specifically exists for childhood RT, as it is so rare. Instead, multiple different therapeutic approaches such as surgery, chemotherapy and radiation therapy are employed in combination for patients. As a result of this, trying to establish a standard regimen for RT especially ATRT is even more challenging (Geller et al., 2015; Ginn & Gajjar, 2012; Heck et al., 2013; Richardson et al., 2018).

1.2.7.1 Multidrug chemotherapy and combination with radiation therapy

When it comes to chemotherapy as a treatment for childhood extracranial RTs there are 2 famous case studies which have to be mentioned due to their rather successful outcomes, Waldron et al. (1999) and Wagner et al. (2002).

In the case study by Waldron et al. (1999) revealed a 31-month-old patient with a stage IV RTK. The line of treatment which was used included a surgical resection of the tumour, radiation therapy and chemotherapy. The dose intensification course for chemotherapy drugs included the combination of vincristine, cyclophosphamide and doxorubicin which was altered every two weeks with ifosfamide and etoposide. From these chemotherapy drugs it was doxorubicin which was seen as an important inclusion for survival. This patient was able to show a complete remission after 60 months since they got their diagnosis. Likewise, the case study by Wagner et al. (2002) whereby they reviewed two cases of patients with a late stage RTK also found success in their multimodal treatment. Besides radiation therapy for both patients they were also given two alternating courses of chemotherapy drugs with the first course incorporating ifosfamide, carboplatin and etoposide and the second course entailing vincristine, doxorubicin and cyclophosphamide. Within about 24 months these patients did not have any evidence of the disease or any detection of metastasis. On the other hand, the study previously mentioned from Tomlinson et al. (2005) had found no overall effect of doxorubicin on the survival rate between those who received it and those who did not.

While various high dose chemotherapy drugs are used for ATRT it is often combined with autologous stem cell rescue for younger patients with ATRT in order to delay or even possibly avoid cranio-spinal radiation (Gardner et al., 2008; Ginn & Gajjar, 2012; Richardson et al., 2018). Gardner et al. (2008) looked at the effect of chemotherapy with stem cell rescue after surgery in 13 children who were diagnosed with ATRT. The induction chemotherapy course consisted of 5 cycles of cisplatin, etoposide, vincristine and cyclophosphamide for 'Head Start 1' which consisted of 6 children and high dose methotrexate was also added to this course for 'Head Start 2' consisting of 7 children. This was then followed by consolidation chemotherapy which contained thiotepa, etoposide and carboplatin alongside stem cell rescue and this was given to patients who presented no evidence of the disease after induction chemotherapy. If there was still evidence of the disease, these patients were, in addition to consolidation chemotherapy, also given radiation therapy. The approximate event-free survival and overall survival rate at 3 years was 23% for the 13 children. Long term remission in this study was therefore said to be achievable when using high dose methotrexate with multi-drug chemotherapy and stem cell rescue which allows patients to

avoid radiation therapy. Furthermore, a Canadian registry has also reported far better outcome when using high dose chemotherapy for childhood ATRT with 2-year overall survival improving from $27.3\% \pm 9.5$ to $47.9\% \pm 12.1$ avoiding the use of radiation therapy (Lafay-Cousin et al., 2012). These results have led to the North American Children's Oncology group conducting a ATRT trial which was based on high dose chemotherapy (Richardson et al., 2018). The initial reports of this study were seen as highly promising as there were notably increased survival rates when compared to the Children's Cancer Group (CCG 9921) and Paediatric Oncology Group (POG 9923) studies that used the usual chemotherapy approaches (Reddy et al., 2016; Richardson et al., 2018). Therefore, from looking at these research findings trial and error with multimodal drug chemotherapy can be regarded a useful treatment option for when treating patients with RTs.

1.2.7.2 Radiation therapy

In terms of radiation and radiotherapy for extracranial RTs, which Tomlinson et al. (2005) also investigated in the NWTS, it was found that from the 142 patients in the study 100 patients had received radiation therapy. Survival rate in those who received the radiation therapy was 28% compared to those who did not receive radiation therapy the survival rate was only 12.2% at 4 years. However, Tomlinson et al. (2005) stated that the effect of radiation therapy was challenging to analyse since in the NWTS it was mainly given to patients who were older and were at a later stage of the disease, age and stage of disease being important prognostic factors relating to treatment mentioned previously. Older patients were able to be given the higher dose of radiation which is associated with better therapeutic effect while there was only a single infant who received radiation therapy at a 25+ Gy dose in this study. Those who received the high 25+ Gy dose had a relative risk of death of 85% than those who did not receive it. Therefore, effect on survival for radiation therapy was decreased and not significant. Radiation therapy doses of 25 Gy have been commonly used since the 1980s for childhood paediatric cancers (Kutanzi et al., 2016). Before this much higher doses were given and these were correlated with short- and long-term side effects as highlighted in the "Cancer" section.

Similarly, radiation therapy tends to be either given at lower dosage or deferred and avoided completely in younger patients with ATRT (Richardson et al., 2018). In the study by von Hoff et al. (2011) no overall survival benefit of radiation therapy was distinguished even in cases where patients received focal or craniospinal radiation therapy, or in cases of salvage and upfront radiation therapy proposing no use of this for childhood ATRT patients. On the other hand, in the meta-analysis of the observational studies, Athale et al. (2009) found a greater mean survival trend for patients given radiation therapy at 18.4 months survival time compared to only 9.5-month survival time for those not receiving it. Equally, overall survival benefits of radiation therapy were described in the paper by Buscariollo et al. (2012) though these were related to age of patients. These contradicting results still pose great challenges in treating patients with ATRT.

As one of the common sites in which RT is found is the brain as mentioned above, the blood brain barrier presents a challenge for drugs to cross at therapeutic concentrations used to treat diseases. More detail about the blood brain barrier is reported in the section “Blood Brain Barrier”.

RTs are difficult to diagnose and treat, there are only a few recorded successful case studies which are found in medical practice. Treatments like chemotherapy and radiation therapy lead to long term adverse side effects in children. Drugs which are used are developed for adults and not specific to children and also normal cells can also be killed with radiation therapy. Therefore, the disease needs investigating from different perspective and therefore our chosen area is at the cellular level.

1.3 Blood Brain Barrier

1.3.1 Background

The blood brain barrier (BBB), consists of a layer of cells in which they are packed tightly together in order to prevent potential therapeutic agents from crossing into the brain at concentrations used to treat diseases (Wohlfart et al., 2012). Highly selective, semi-permeable as well as restrictive are a few of the words associated with the BBB. This means that the BBB only allows certain molecules to enter the brain via various methods of transport. By injecting the bloodstream of a mouse with dye, Paul Ehrlich was able to initially demonstrate that a barrier existed between the blood and the brain in the late 19th century (Dyrna et al., 2013). It was then later learnt that the BBB contained brain capillaries which led to the limited passage of molecules into the brain though it was still not known which properties allowed for the restrictive nature of the BBB. The introduction of the powerful electron microscope was used to establish the individual layers of the BBB, the cells which were accumulated in this and how the BBB worked, was understood (Dyrna et al., 2013; Pardridge, 2012). The limiting access into the BBB proves to be a great challenge for scientists when developing methods of drug delivery and therapeutics into the brain (Daneman & Prat, 2015).

Dong (2018), has emphasised the low success rate of drugs being developed specifically targeting the brain each year in comparison to the drug development in other fields. This is a major problem as the number of individuals with brain diseases (including cancer) is increasing, and drug development is unable to keep up. The process of drug development runs into many major problems which Dong (2018) has highlighted can encompass clinical trials, side effects of the drugs and the complexity of the brain itself.

1.3.2 Cells and the Blood Brain Barrier

Within a healthy brain environment, the BBB plays a crucial role in maintaining the homeostasis which is a key component for allowing proper neuronal function to take place (Daneman & Prat, 2015). The BBB comprises of specialised cells as shown in Figure 11, including endothelial cells (ECs), astrocytes, pericytes, tight junctions (TJs), neurons, and the basal membrane (Di et al., 2008). These cells work together in order to build “tight brain capillaries in the BBB” as referred to by Dong (2018). The inter-endothelial junctions so the

TJs, adherens junctions and gap junctions each control the permeability of the brain and they link the ECs together forming a continuous barrier. The ECs and TJ barrier are also further surrounded by the pericytes, astrocytes and the basal membrane (Dong, 2018). Each of these components are essential and important in protecting the brain from harm. The BBB is a complex microenvironment and has a gap of only 40 nm between the cells (Warren, 2018). Additionally, it has been mentioned that the BBB does not have a static structure, because of this the components of the BBB are able to change when physiological changes occur in the brain (Dong, 2018; Warren, 2018). Therefore, the structure of the BBB is seen as more dynamic than static.

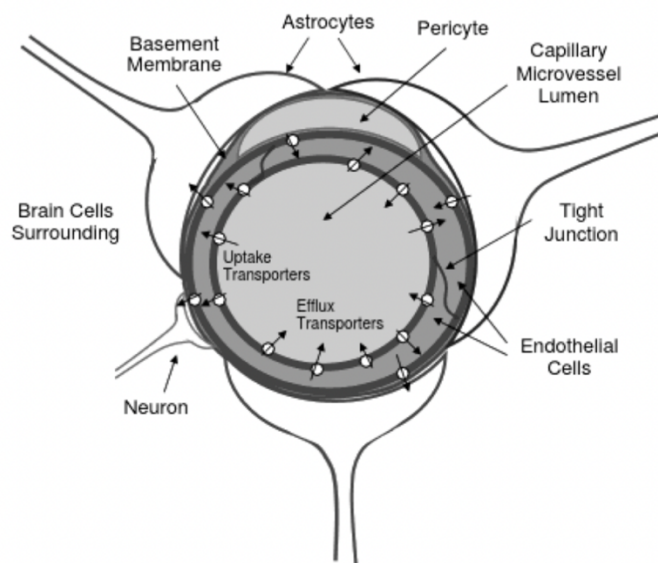


Figure 11. Schematic diagram showing the cross-section of the different components which make up the blood brain barrier (Di et al., 2008).

The small gaps in the BBB only allow for the passage and diffusion of small molecule drugs which have a molecular weight of less than 400 Da and approximately less than 8 hydrogen bonds (Pardridge, 2012). Therefore, as illustrated in Figure 12, most therapeutic drugs are unable to reach the concentrations needed to provide remedial benefits in the brain, with only about 2% of drugs which are discovered actually passing the BBB (Di et al., 2008). Furthermore, proteins and water-soluble molecules such as glucose are able to pass into the BBB using transporter proteins (Dong, 2018; Warren, 2018).

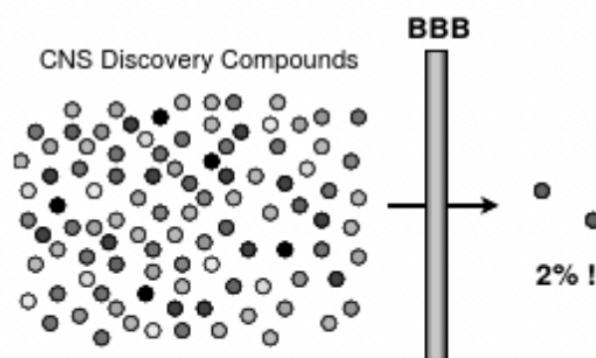


Figure 12. Only about 2% of the possible drugs which are discovered are actually able to pass the BBB (Di et al., 2008).

1.3.3 Methods & strategies for crossing the Blood Brain Barrier

In the recent years many techniques have been tried as potential strategies for transporting and facilitating drugs into the brain surpassing the BBB.

1.3.3.1 Active transporters

One method to achieve this through the use of active transporters in the BBB. Linking drugs to amino acid transporters allows them to enter into the BBB. In the study by Peura et al. (2013) which looked at improving the brains uptake of dopamine, showed how they were able to achieve this in two stages. Firstly, the authors synthesised 3 amino acid prodrugs of dopamine and then they were able to transport it across the BBB by utilising the large amino acid transporter 1 (LAT1) found in the BBB. Peura et al. (2013) used rat brain perfusion in their study which revealed that the phenylalanine prodrug had produced higher affinity and brain uptake when compared to the other prodrugs in the study. On the other hand, while this technique seems advantageous, Dong (2018) has argued that it can only be used for the transport of small molecules therefore limiting its use.

Other examples of active transporters include the active efflux transporters, specifically those belonging to the ATP-binding cassette (ABC) gene family. These ABC efflux transporters of the BBB include P-glycoprotein (P-gp), multidrug resistance protein (MRP) as well as the breast cancer resistance protein (BCRP). Löscher and Potschka (2005) have described the purpose of these efflux transporters as they can determine which drugs are circulated in the brain and

those which are gotten rid of. For example, lipophilic drugs can be taken out of the brain capillary ECs, which make up the BBB as seen in Figure 11, using the P-gp efflux transporter. Qosa et al. (2015) have also noted that this control of the ABC is able to reduce the exposure of toxic side effects of drugs which otherwise would have been able to enter the brain though this has also resulted in limited amounts of therapeutic drugs penetrating into the brain. Resistance to therapeutic drugs is also a problem associated with active efflux transporters due to them being overexpressed at the BBB. By activating A2A adenosine receptor with an A2A adenosine receptor agonist such as Lexiscan, Kim and Bynoe (2016) have stated that P-gp expression can be decreased allowing anticancer drugs to adequately accumulate in the brain. Thus, while some active transporters can aid drug delivery, targeting a decrease in expression for active efflux transporters can also provide another therapeutic method in which drug delivery can increase to the brain.

1.3.3.2 Viral vectors

Viral vectors have been studied for many years as sources of gene delivery. Gene delivery which has been emphasised as a cancer treatment option, allows genetic information to be passed on to target cells, which will then help produce the required therapeutic proteins (Collins et al., 2008). This is because viruses themselves are unable to passively get into the BBB, instead the viruses transfect/introduce the genetic material into the target cell (Dong, 2018). This approach of using viral vectors is seen as promising as a result of the high transfection efficiency it produces (Pérez-Martínez et al., 2012). Specifically, the adeno-associated virus (AAV) vectors have been used for gene delivery into the brain, crossing the BBB, as they have shown remarkable safety profiles within humans (Bors & Erdő, 2019; Dong, 2018). In the study by Zhang et al. (2011) the authors were able to demonstrate how recombinant AAV vectors were able to overcome and cross the BBB in neonatal mice. However, whilst there are many advantages of using viral vectors as drug delivery systems which can surpass the BBB, there are also many limitations. Pérez-Martínez et al. (2012) emphasised that manufacturing and producing viral vectors can be very difficult and also highly expensive. In addition to this, the safety of the use of viral vectors as a whole has not been confirmed yet. In a clinical trial for the AAV2_{CU}hCLN2 viral vector, which was administered using a highly invasive and risky approach; via injection directly into the brain through burr holes made in the skull, many adverse effects were seen, but it was not

confirmed whether this was due to the vector itself or other possible factors (Dong, 2018). Due to these limitations more research and trials are needed before viral vectors are utilised on humans.

1.3.3.3 Nanoparticles

Nanotechnology, particularly nanoparticles, have provided an alternative method for facilitating drugs into the brain, across the BBB (Alam et al., 2010). Nanoparticles use the receptor-mediated endocytosis mechanisms that are found within the brain capillaries endothelial cells to cross the BBB (Alam et al., 2010; Wohlfart et al., 2012). In a study by Medina et al. (2017) the synthesised poly(lactic-co-glycolic acid) (PLGA) nanoparticles conjugated with quantum dots (QDs) were reported. These QDs acted as “barcoding” allowing to track the nanoparticles at the cellular level. This research showed that these nanoparticles do not cross the healthy BBB but are able to do so in the presence of brain tumours through various methods. Gao et al. (2017) were able to encapsulate the hydrophobic drug, propofol, by using propionylated amylose helix which would form the nanoclusters. In their study the Goa team found that by triggering a particular physiological condition in the brain, the nanoparticles were able to facilitate the encapsulated drug to be released, generating a high concentration which in response allowed it to cross the BBB. While nanoparticles are effective for brain drug delivery, Saraiva et al. (2016) has mentioned that large amounts of these nanoparticles are still found in different regions of the body including the kidneys and liver before they are removed which could be harmful. Therefore, work needs to be done so nanoparticles which release drugs, are solely made to target the brain and even specific brain cells further improving therapeutic efficacy (Saraiva et al., 2016). Nanoparticles such as lipoproteins, which have been used as drug carriers, also have limited applications as there are issues regarding the scale up and drug loading processes (Dong, 2018).

Other useful techniques which are also employed include disruption of the BBB and using brain permeability enhancers to facilitate drug delivery into the brain. These techniques work by using molecules which target specific areas of the BBB to open momentarily allowing large concentrations of drugs to be dispensed directly into the brain. An example of a permeability enhancer includes cereport, the synthetic bradykinin agonist RMP-7. In the article by Prados et al. (2003), the authors described how cereport was able to successfully increase the

amount of carboplatin reaching the brain tumours of animal models, but similar results could not be achieved when trialled for malignant glioma patients. Hence, more research and understanding are still required due to studies into these areas showing discrepancies between animal and human findings (Dong, 2018). As well as employing new techniques in order to facilitate the drug delivery cascade, drugs themselves can also be repurposed to pass through the BBB.

1.4 Drug repurposing

1.4.1 Background

The term drug repurposing is also frequently denoted as drug repositioning and drug redeployment. Drug repurposing is a useful technique in which new uses and different medical indications are discovered for existing drugs, so they can be used as treatments for diseases which they were not originally designed for (Pushpakom et al., 2019; Shim & Liu, 2014; Xue et al., 2018). The drugs which are used for the repurposing can be pre-existing cancer drugs referred to as “soft repurposing”, or non-cancer drugs referred to as “hard repurposing” (Pantziarka et al., 2018).

1.4.2 Traditional Drug Development vs Drug Repurposing

Drug repurposing is seen as an effective alternative approach in comparison to the traditional drug discovery strategies. Traditional drug discovery is very time-consuming, can be very expensive and the processes have high-risk factors associated with them, while drug repurposing is seen as a high reward method (Shim & Liu, 2014; Xue et al., 2018). The whole process of traditional drug development starting from the bench-top to the market is a strenuous process, outlined in Figure 13, which can take many years to successfully get a drug approved and into the market. The paper presented by Shim and Liu (2014), reports that in the US and EU, the time it takes to get drugs into the market has increased over the years, during the 2000s it took around 10 years but can now take up to at least 14+ years. Moreover, Shim and Liu (2014) found that even though more and more money is being spent by large pharmaceutical companies into the discovery and development of new drugs, the amount of actual new drugs on the market has not increased abundantly. In comparison to the traditional methods, drug repurposing, as outlined in Figure 14, is able to get a drug on to the market in far less time and is seen more cost effective on a global scale. For many countries it can cost around \$1.6 billion to develop new uses for existing drugs through drug repurposing, whilst traditional drug development can cost around \$12 billion hence giving many countries more opportunities of developing drugs which have far less investments (Xue et al., 2018).

1.4.2.1 Traditional drug development timeline

Traditional drug discovery consists of many stages with the 3 main phases being discovery phase, development phase and then the approval and market phase all shown in Figure13 (Lombardino & Lowe, 2004; Xue et al., 2018). Once the area of medical need is identified and other background research is done, chemicals are synthesised and tested in laboratories and in animal models to check for their efficacy and safety (Lombardino & Lowe, 2004; Xue et al., 2018). As a result, at the end of the discovery phase the drug candidate is chosen for development. During the development phase the chosen candidate goes through further testing in animals as this is something which is required by law, before the scale-up synthesis occurs. Once the safety of the drug has been further confirmed the pharmaceutical company will then file for an Investigational New Drug (IND) application to the Food and Drug Administration (FDA) (Lombardino & Lowe, 2004). Clinical trials begin with phase 1 where healthy individuals are recruited and tested for tolerance with the new drug. In phases 2 and 3 of clinical trials sick patients are used at a larger scale and are monitored for a longer period of time to test the drug for side effects, toxicity and other problems so these issues can be adjusted (Lombardino & Lowe, 2004; Xue et al., 2018). Once the drug has been perfected the company will file a New Drug Application (NDA) to the FDA, if this is then approved by the FDA the drug will then be put on the market. Additionally, Xue et al. (2018) have mentioned that even after the drug has been approved it is still monitored by the FDA.

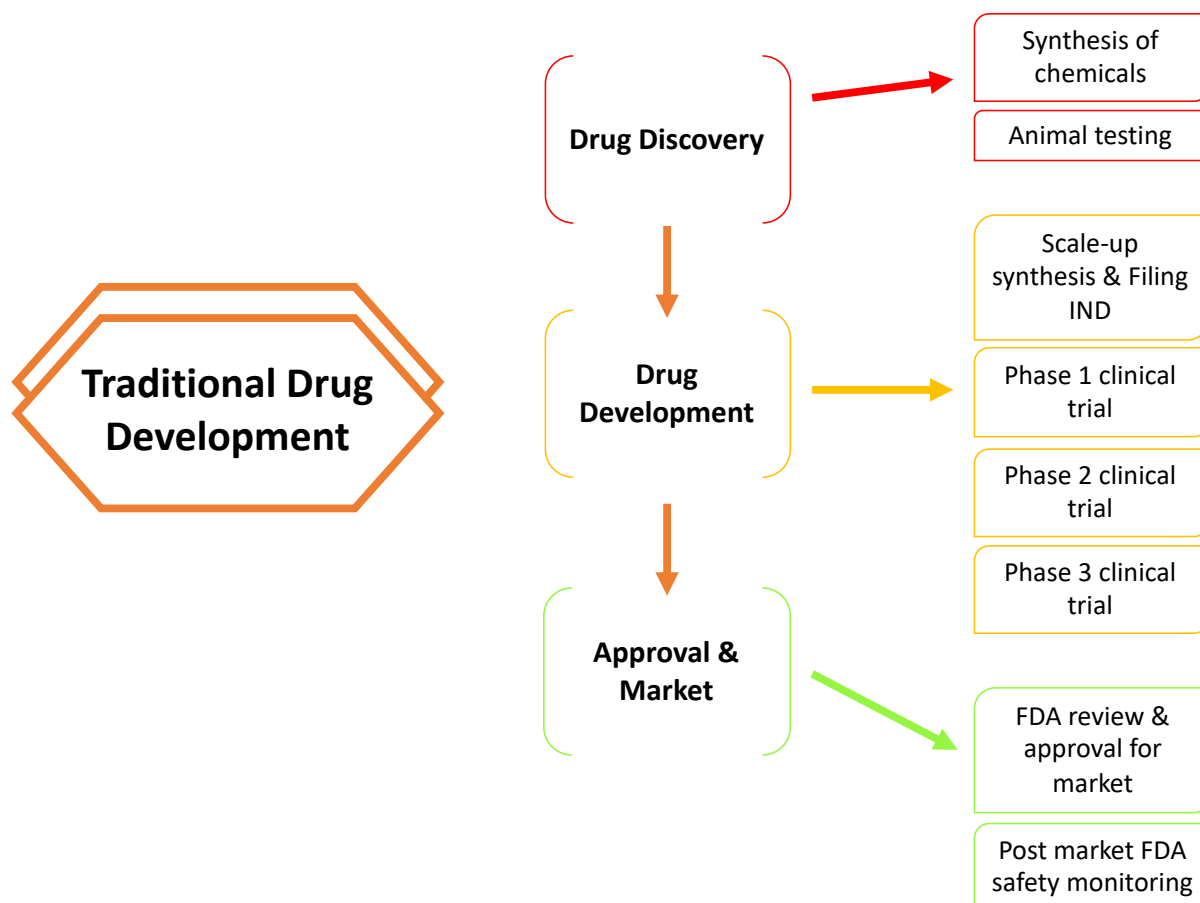


Figure 13. Steps for traditional drug development. Adapted and modified from the authors Xue et al. (2018) as well as Lombardino and Lowe (2004).

1.4.2.2 Drug repurposing timeline

In drug repositioning fewer steps are taken to get a drug into the market which can be seen in Figure 14. Once the drug candidate is established, pharmaceutical companies need to get a licence for the drug. During the development phase the safety and efficacy is tested and depending on the chosen drug candidate this could begin at various stages whether it is the pre-clinical or clinical trials. This is because much information about toxicity and safety issues may already be known about the drug as it could already be approved by the FDA and exist in the market. After these tests are completed the FDA will review it and upon approval the drug will then enter the market where it will still be monitored by the FDA (Xue et al., 2018).

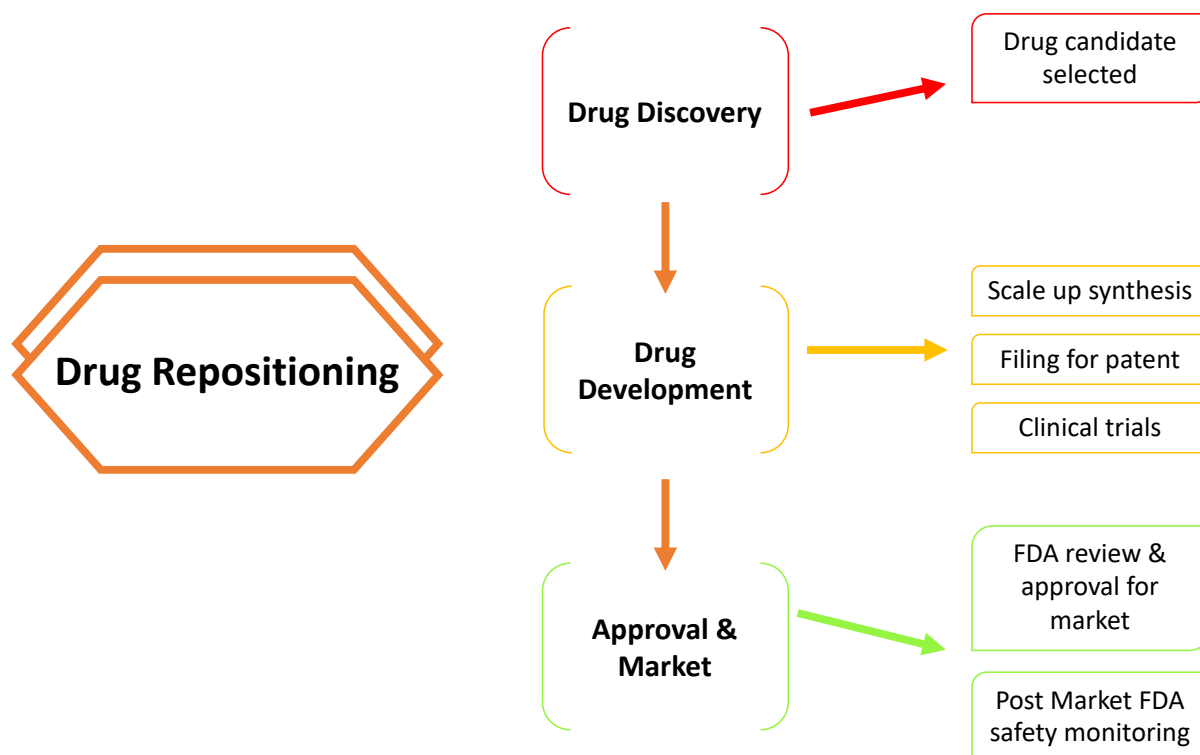


Figure 14. Steps involved in drug repositioning. Adapted and modified from Xue et al. (2018).

1.4.3 Activity based and *in-silico* based drug repositioning

With soft and hard repurposing, there are two further approaches used by researchers for choosing which drugs to use when it comes to drug repurposing, activity-based and *In-silico* based drug repurposing. Activity-based drug repurposing allows the researchers to screen the actual drugs while *in-silico* based drug repurposing uses databases and other bioinformatics tools to comprehensively determine interactions between potential drugs and their protein targets (Dubus et al., 2009; Shim & Liu, 2014). Between the two methods *in-silico* based drug repurposing is seen as more successful as it can be done quicker, cheaper, it does not require the entire collection of existing drugs. While this is the case, Shim and Liu (2014) have outlined that drawback related to the high rates of false positives achieved in the screening with *in-silico* based drug repurposing still exist with this method.

1.4.4 Examples of repositioned drugs

1.4.4.1 Sildenafil

A widely known example of a repositioned drug includes Sildenafil, a phosphodiesterase type 5 (PDE5) inhibitor. Originally developed to treat hypertension and angina by Pfizer in 1985, this drug had failed during the phase 2 clinical trials. The induction of penile erections was found to be a side effect of Sildenafil during the phase 1 clinical trials in the UK. As a result, the focus was shifted, and Sildenafil was repurposed and approved by the FDA for the treatment of erectile dysfunctions, ultimately leading Pfizer to the production of a blockbuster drug marketed as Viagra® in 1998 (Jourdan et al., 2020; Shim & Liu, 2014).

1.4.4.2 Thalidomide

Another well-known example of a repurposed drug includes Thalidomide. The main purpose of Thalidomide, when it was first put into the market in 1957, was for the treatment of morning sickness to aid pregnant women. However, one of the major side effects of this drug and the main reason this drug was pulled off from the markets, included birth defects and death affecting over 10,000 children worldwide. While it resulted in some children being born without limbs others had deformed limbs and many other extremities and ultimately the many children did not survive after a few months. Once it was off the market research groups looked at the structure of Thalidomide once again, and this time they found anticancer properties such as tumour angiogenesis as well as cell proliferation associated with it. Additionally, Thalidomide was tested in clinical trials against many human cancers. Thalidomide was therefore repurposed and approved by the FDA as a first line treatment option for multiple myeloma in combination with Dexamethasone (Boyer et al., 2018; Jourdan et al., 2020; Shim & Liu, 2014; Telleria, 2012).

1.4.4.3 Remdesivir

Recently, the drug Remdesivir has been repurposed. This drug was initially developed in 2014 during the outbreak of Ebola where much success was amassed across animal models however it failed to replicate this success during the clinical trials on humans (Eastman et al., 2020; Pardo et al., 2020). Now due to the COVID-19 pandemic where antiviral treatment such as vaccines are needed remdesivir has shown to be a promising candidate in this regard. In

one study by Grein et al. (2020) clinical improvements were seen in 36 out of the total 53 COVID-19 patients who were treated with compassionate use remdesivir. Additional studies have also yielded similar findings and as a result the FDA approved its use for hospitalised COVID-19 patients (Eastman et al., 2020).

1.4.5 Drugs repurposed in this research project

In this present study the drugs which have been chosen for repurposing prospects include carvacrol and loratadine.

1.4.5.1 Carvacrol

Carvacrol (5-isopropyl-2-methylphenol) is a monoterpene phenol (Figure 15a) found as the main constituent of many essential oils including aromatic plants such as oregano and thyme (Figure 15b). This monoterpene has been classified as, generally recognised as safe (GRAS), by the FDA and as a result there are various commercial uses of carvacrol found in food industries as a flavouring agent and food preservative and cosmetic industries in perfume (Lopez-Romero et al., 2015; Suntres et al., 2015). Various research studies have demonstrated the strong anti-inflammatory, antimicrobial and antifungal properties associated with carvacrol as well as the anticancer properties which will be the focus of this research project (Lopez-Romero et al., 2015; Suntres et al., 2015).

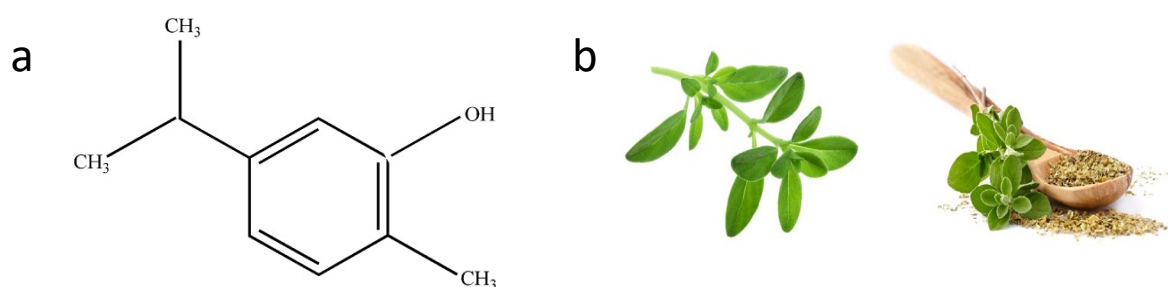


Figure 15. (a) Chemical structure of carvacrol (Yin et al., 2012) (b) thyme (left) and oregano (right) aromatic plants (Marshall, 2021).

1.4.5.1.1 Effect of carvacrol on non-small cell lung cancer

In a study conducted by Koparal and Zeytinoglu (2003), they investigated the effects of carvacrol on the human non-small lung cancer (NSCLC) cell line A549. From their findings Koparal and Zeytinoglu (2003) established that carvacrol did effect the A549 cells through induction of cytoplasmic blebbing leading to inhibition of cell viability and cell proliferation. The carvacrol treated A549 cells were able to display some apoptotic characteristics and when compared to the HFL1 cell line which are normal lung cells carvacrol showed no impactful effect on these cells. This lead to suggestive conclusions early on that carvacrol may display anticancer effects and therefore can be used as a possible drug candidate for treating cancer (Koparal & Zeytinoglu, 2003). In addition to this, in a later paper by Jung et al. (2018) who also looked at the effect of carvacrol on NSCLC, achieved similar findings. Jung et al. (2018) reported that AXL, a receptor tyrosine kinase commonly overexpressed in patients with NSCLC (Zhang et al., 2018) resulting in enhanced cell survival and proliferation, is downregulated when in the presence of carvacrol treatment at a transcriptional level.

1.4.5.1.2 Effect of carvacrol on human metastatic breast cancer

Furthermore, anticancer effects of carvacrol have also been discovered in human metastatic breast cancer cells specifically the MDA-MB 231 cell line. Arunasree (2010) found that carvacrol was able to induce apoptosis in the MDA-MB 231 cells and used a variety of assays in order to prove this work which included, MTT (3-(4,5-dimethylthiazol-2-yl)-2,5-diphenyltetrazolium bromide), Annexin V and the mitochondrial membrane potential assay. Apoptosis induction for the MDA-MB 231 cells was ultimately dose dependant on the IC₅₀ of carvacrol at 100 mM and this led to Arunasree (2010) further demonstrating the potential of carvacrol as a therapeutic drug candidate when treating cancers.

1.4.5.1.3 Effect of carvacrol on human oral squamous cell carcinoma

Additionally, Dai et al. (2016), found that carvacrol was able to inhibit the tumour cell proliferation, metastasis and invasion while also inducing apoptosis in human oral squamous cell carcinoma (OSCC). Carvacrol was able to achieve this by downregulating the CDK regulators, CCND1 and CDK4 while also upregulating the CDK inhibitor P21. These results provided a mechanism of how carvacrol worked in human OSCC therefore aiding future treatment options.

1.4.5.2 Loratadine

Loratadine is a second-generation antihistamine medication (Figure 16), marketed and more commonly known as Claritin (Blass, 2015). It has been used to manage allergies by blocking the action of the histamine receptor H_1 , without causing sedation, a problem which occurred with those of the first generation antihistamines (Randall & Hawkins, 2018; Tenn et al., 2018). Haria et al. (1994) analysed 15 different studies which consisted of up to 55,000 patients related to loratadine. The authors found that this drug was well tolerated by many age groups including children and the elderly when they were given 10 mg per day with few side effects. Loratadine has also shown anticancer effects against many cancer cell lines including NSCLC and breast cancer.

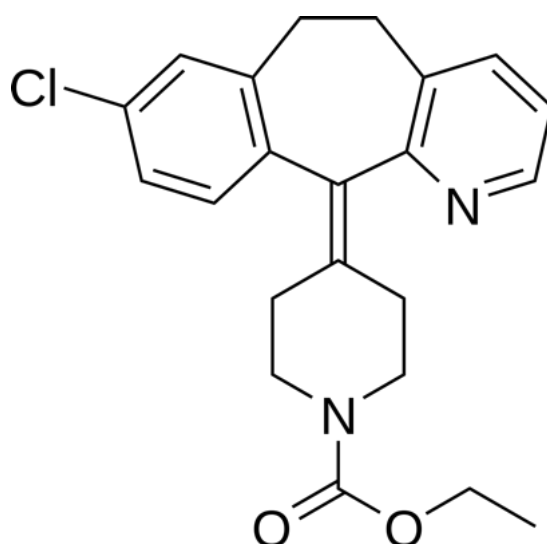


Figure 16. Chemical structure loratadine (Lovskaya & Menshutina, 2020).

1.4.5.2.1 Effect of loratadine on non-small cell lung cancer

Loratadine has been linked to the reduced mortality of patients when it was repurposed for non-localised NSCLC. Ellegaard et al. (2016) carried out a cohort study over a 16-year time period from 1995 to 2011 in Denmark looking into loratadine as a possible treatment option for NSCLC. Loratadine was chosen after screening the cationic amphiphilic drug (CAD) library found this to be able to induce lysosomal cell death and produced cytotoxic activity against NSCLC. Ellegaard et al. (2016) also found that patients who had received concurrent chemotherapy alongside loratadine those were the patients where reduced mortality was highest compared to those who did not receive chemotherapy. Therefore, the possible

conclusion of CAD antihistamines including loratadine being able to boost the efficacy of chemotherapy was made.

1.4.5.2.2 Effect of loratadine on breast cancer

Breast cancer survival has been shown to improve when treating those diagnosed with antihistamines such as loratadine. Fritz et al. (2020) studied the effect loratadine among other antihistamines in 61,627 Swedish women who were diagnosed with breast cancer between 2006 to 2013. It was found that compared to those who did not use the antihistamines survival improvement of breast cancer was definitely noticeable regardless of factors such as stage of the cancer or the age of patients. Olsson et al. (2018) were also able to achieve similar findings in their study and additionally suggested beginning trials into using antihistamines (loratadine and desloratadine) as a potential adjuvant treatment option in breast cancer.

Subsequently, from the anticancer and other properties mentioned above shown by both drugs makes them notably ideal candidates for drug repurposing use in this research project.

Chapter 2 Introduction to experimental techniques

2.1 Cell culture

2.1.1 Background

The process of cell culture is defined as removing animal or plant cells from their natural setting (*in vivo*) and growing them in an artificial and controlled environment (*in vitro*) with closely monitored conditions (Hudu et al., 2016). The earliest record of cell culture can be dated back to the 20th century where it was first used to study the behaviour of animal cells and tissue growth among other things (Segeritz & Vallier, 2017).

Cells can exist in two different forms, either adherent, like the A204 cells in this research project presented in Figure 17a, or suspension like those shown in Figure 17b for the K562 parental cells (Baykal-Köse et al., 2020). Adherent cells are anchorage-dependant, and this is the form most cells take. In this case, cells need to attach to something like the surface of the culture flask, in order to proliferate, for example mouse fibroblast STO cells (Segeritz & Vallier, 2017; Verma et al., 2020). On the other hand, McAteer and Davis (2002) have stated that suspension cells can successfully proliferate detached from the surface floating in the culture media. Verma et al. (2020) have used the example of blood cells as suspension cells as they are suspended in plasma and therefore would easily be able to grow in suspension cultures.

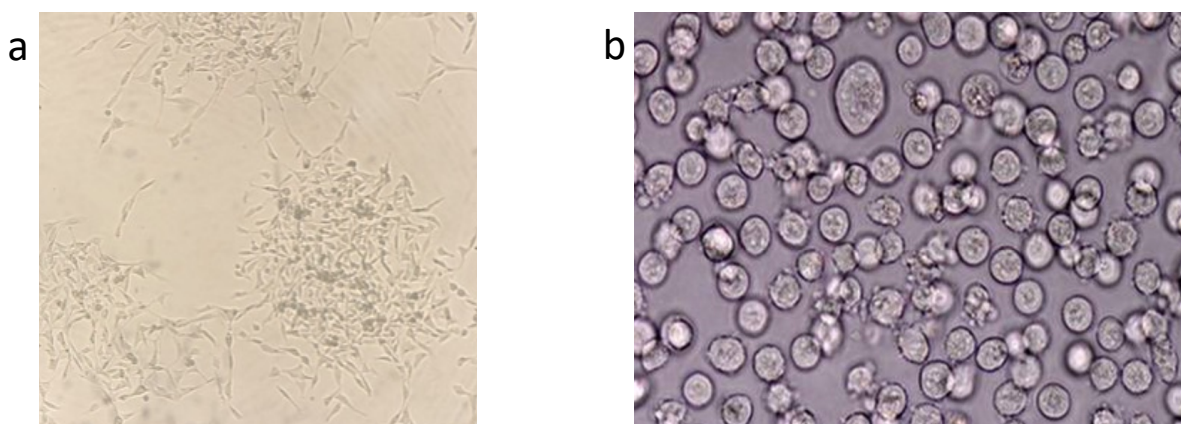


Figure 17. (a) An example of our adherent A204 cells under the microscope. (b) Example of suspension K562 parental cells (Baykal-Köse et al., 2020).

In order to grow and establish a cell line, the process initiates from acquiring cells directly from the tissues which are then treated with the growth media to reach confluence, a primary

culture. The term confluence refers to the surface of the culture flask being covered up to 80% in a monolayer of growing cells. From this, the cells are sub-cultured/passaged in new flasks and media giving rise to a secondary culture and this process continues many times creating a cell line (Hudu et al., 2016; McAteer & Davis, 2002).

McAteer and Davis (2002) have stated that in order to achieve successful survival and proliferation of the isolated cells, the in vitro conditions in which they are kept are very important. Since cells are so used to living in certain conditions the in vitro environment must match this. The cell culture medium allows control over factors such as pH, the nutrient composition, osmolality plus the amount and times it is refilled and changed. The authors have also made clear that each cell line is unique to what it needs to survive and proliferate however most mammalian cell cultures optimal culture conditions include four key factors: a pH ranging between 7.2 and 7.5, osmolality between 280 to 320 mOsmol/kg, the CO₂ levels in the air should be from 2% to 5% and the temperature ranging between 35 °C to 37 °C.

2.1.2 Advantages and disadvantages of cell culture

Several useful advantages and applications of cell culture exist. Cell culture has allowed scientists to develop model systems relating to diseased cells granting deeper insight into their basic biology and physiology (Segeritz & Vallier, 2017). In the paper from Verma et al. (2020), it was mentioned that information regarding the origin of cells can be found through homogenous culture. Additionally, it was stated that animal cell cultures also allow specific cell types to be identified through biomarkers or even karyotyping. The work of cell culture also allows researchers to avoid backlash resulting from ethics and morals as animals in a 'living' sense are not used in the experiments.

Cell culture is especially important when it comes to cancer research. As normal healthy cells and cancer cells can be cultured, scientists can study the differences which exist between them. By understanding the possible pathways normal cells take to develop into cancer cells, researchers can use cell culture to screen drugs accordingly and experiment until non-toxic doses with the least side effects are discovered (Segeritz & Vallier, 2017). Furthermore, the benefits of cell culture have also been reaped in the field of genetic engineering. By recognising the effect genes can have on cells, this has allowed for genetic manipulation

whereby the genome of the cells is changed to help repair the genes which are not correctly functioning in patients (Segeritz & Vallier, 2017; Verma et al., 2020).

On the other hand, many cons of cell culture also exist. Segeritz and Vallier (2017) have argued that contamination in cell culture is a problem mainly because they are highly challenging to spot and contamination in the form of mycoplasma and viral infections are seen as contagious. Reasons for contamination could result from human error due to the lack of knowledge regarding the proper care and handling of cell lines (Mirabelli et al., 2019). As well as this, after many passages and subculturing of cells, it can lead to changes in properties and outcomes which were originally seen in the initial cells possible reducing the ability to achieve reproducible results (Segeritz & Vallier, 2017).

2.2 Cytotoxicity assay

The MTT colorimetric assay is a well-established gold standard method used to assess cell proliferation, cell viability and cytotoxicity (Stockert et al., 2012). In this research project MTT assay was used to assess cytotoxic effects and the cell viability of A204 cells in the presence of carvacrol and loratadine. Cells which are viable contain enzymes of nicotinamide adenine dinucleotide phosphate (NADPH) dependant cellular oxidoreductase which reduces the yellow tetrazolium dye MTT to its insoluble purple formazan crystals; providing clear visual representation of cell viability and toxicity (Kwete et al., 2017). This reduction is found to mainly take place in the mitochondria of living cells, though Lü et al. (2012) have also suggested involvement of other organelles like the endoplasmic reticulum which also encompasses reducing agents and enzymes. Therefore, Lim et al. (2015) have stated that the number of living, viable cells which are found in the cell culture can be directly correlated to the amount of purple formazan crystals which are formed. An example of an MTT assay 96-well plate is shown in Figure 18 below where viability of A204 cells (purple formazan crystals) can be seen in the presence of various drugs and culture medium.

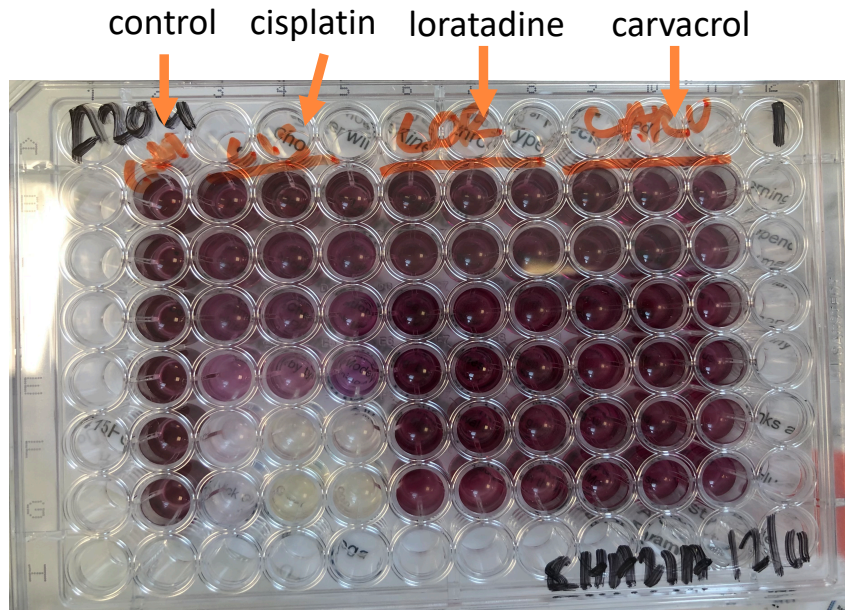


Figure 18. Cell viability MTT assay done on A204 cells in the presence of a control (cell culture medium), cisplatin, loratadine and carvacrol.

2.3 Fourier transform infrared spectroscopy

2.3.1 Background

Fourier transform infrared (FTIR) spectroscopy is a powerful analytical tool which can be used to identify the biochemical composition of many inorganic and organic molecules including biological molecules (Sabbatini et al., 2017; Su & Lee, 2020). Essentially, when the molecules interact with the IR radiation, some of this radiation is absorbed by the molecules while the rest just passes through and is transmitted. Therefore, FTIR is able to quantify the absorption produced by infrared light from the components of the biological sample which results in an FTIR spectrum. The spectrum is plotted with either the % transmittance or the absorption intensity against the wavenumber. This was a method which was originally widely used for molecular structure determination in analytical chemistry traditionally by chemists, though it is now dominating in the field of biomedical research (Fale et al., 2015; Mohamed et al., 2017; Su & Lee, 2020; Vogt et al., 2019). The schematic diagram of the components of FTIR and their set up is provided in Figure 19 (Mohamed et al., 2017).

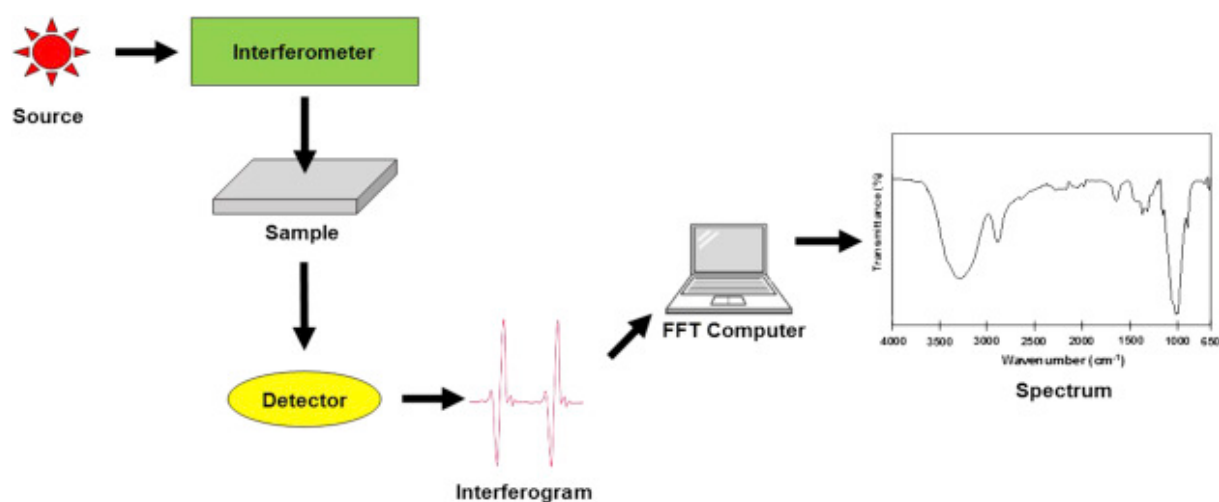


Figure 19. Schematic illustration of the process of Fourier transform infrared (FTIR) (Mohamed et al., 2017).

2.3.2 Spectral band analysis

Cells are made up of various biological molecules such as lipids and proteins which each have different chemical structures as they consist of varying functional groups including methyl groups (CH₃), hydroxy groups (OH) and carbonyl groups (R-C=O) and it is these which govern

how the molecule will interact with the Infrared (IR) radiation resulting from the molecular vibrations (Barth, 2007; Sabbatini et al., 2017). These molecular vibrations include bending and stretching vibrations which are specific to each bond involved in the biological molecules, occurring when IR radiation is absorbed. This results in an overall net change in the dipole moment allowing the molecule to be IR active (Baker et al., 2014; Barth, 2007).

Functional groups of biological molecules have distinct and well-defined spectral peaks on an IR spectrum which is unique for all cells (Walsh et al., 2008). This is seen as an important use of FTIR spectroscopy as it allows monitoring of the biochemical response of the cell before and after it has undergone treatment for example with different combinations of drugs (Sabbatini et al., 2017). Table 1 provides an overall summary, gathered from previous papers, on the spectral peak ranges of the specific functional groups of biological molecules (Baker et al., 2014; Derenne et al., 2014; Sabbatini et al., 2017; Su & Lee, 2020). The fingerprint region ($600\text{--}1450\text{ cm}^{-1}$) as well as the amide I (1700 cm^{-1}) and amide II (1500 cm^{-1}) spectral regions are the most important when it comes to biological materials, as this is where most of the constituents are found. Additionally, the stretching vibrations are located at the higher wavenumber regions which are found between $2550\text{--}3500\text{ cm}^{-1}$ and these include the S-H, C-H, N-H and O-H bonds. The bending vibrations are found between $1460\text{--}1400\text{ cm}^{-1}$ as the $\text{CH}_2/3$ groups from the side chains on amino acids as well as fatty acids are present here (Baker et al., 2014; Sabbatini et al., 2017; Su & Lee, 2020; Walsh et al., 2008). Moreover, the low wavenumber region is found between $650\text{--}1500\text{ cm}^{-1}$ (Mohamed et al., 2017). The typical peak assignments of the constituents of biological molecules are also presented in the biological spectrum in Figure 20 below (Baker et al., 2014).

While the Beer-Lambert law states that the area of the peak is proportional to the concentrations of the functional group in the biological material, Dreissig et al. (2009) have reported that it is not actually common to find a single wavenumber which is associated with a single constituent of a complicated biological material, which is also seen in Table 1. Therefore, a range is more likely to be used to quantify a component in a biological sample and moreover Derenne et al. (2014) have mentioned that IR spectroscopy has to be calibrated using not only the reference spectra but also with multiple wavelength regression.

Table 1. Typical wavenumber assignments of the specific functional groups associated with various biological molecules.

Biomolecule	Functional group	Wavenumber (cm ⁻¹)	References
Lipid	CH ₂ & CH ₃	3050-2800	(Derenne et al., 2014; Sabbatini et al., 2017)
	C=O	~1745	
Protein	Peptide bonds	1700 (Amide I)	(Baker et al., 2014; Su & Lee, 2020)
		1500 (Amide II)	
Carbohydrate	C-OH	~1050	(Sabbatini et al., 2017)
DNA	Phosphodiester bond	~1241	(Baker et al., 2014; Sabbatini et al., 2017)
	Deoxyribose C-O	~1020	
RNA	Ribose C-O	~1120	(Baker et al., 2014; Sabbatini et al., 2017; Su & Lee, 2020)

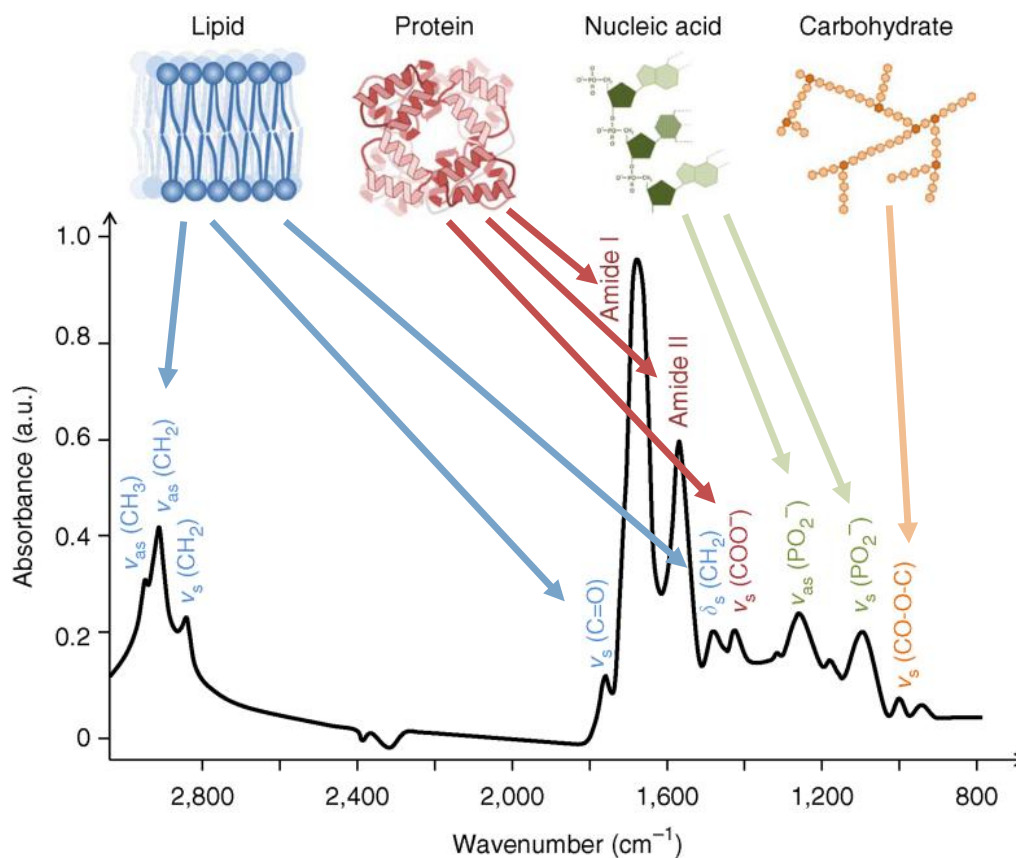


Figure 20. A biological spectrum with the typical peak assignments associated with biological molecules, ranging from 3000 – 800 cm⁻¹ (Modified from Baker et al., 2014).

2.3.3 Advantages and applications in cancer

There are many advantages associated with using FTIR as a diagnostic tool especially in the field of cancer. Firstly, the simplicity involved in this technique allows it to be highly reproducible as well as label-free and non-destructive when analysing and therefore providing detailed information about the various biological materials (Baker et al., 2014; Chrabaszcz et al., 2018; Doherty et al., 2018; Su & Lee, 2020). Le Naour et al. (2012) were able to show in their study how the sensitivity of FTIR towards the chemical changes from the alteration of the liver in a normal state to a pathological state is able to lead to the identification of a biomarker related to chronic liver diseases. This is able to further demonstrate the use of FTIR spectroscopy in cancer due to its many clinical uses, including diagnosis, interpreting the cell spectra to identify the different stages cancer cells are in and monitoring the response of the cancer cells towards treatment (Fale et al., 2015; Su & Lee, 2020). Hence, monitoring treatment response of extracranial RT cells will be the purpose of FTIR in this study.

Lewis et al. (2010) were able to utilise FTIR spectroscopy for lung cancer detection from the biochemical changes which occurred in the sputum as their biomarker. From the sputum which was obtained from all the participants (25 lung cancer patients and 25 healthy control participants) the changes were monitored. Lewis et al. (2010) found that FTIR was successfully able to produce clear distinct spectra for those with lung cancer and the control group. Wavenumbers which were obtained at regions 964 cm^{-1} , 1024 cm^{-1} , 1411 cm^{-1} , 1577 cm^{-1} and 1656 cm^{-1} resulted in the main differences between the two spectrums. The spectra achieved for these distinct differences can be seen in Figure 21 whereby the dashed line represents the healthy control group, and the solid line represents the cancer group (Lewis et al., 2010). The wavenumbers labelled F and E on the spectra, 1656 cm^{-1} and 1577 cm^{-1} , produced peaks correspondingly in the amide I and the amide II regions. The peaks found in the regions of 1400 cm^{-1} to 1450 cm^{-1} , which has been linked to proteins, produced a much broader peak around 1411 cm^{-1} for the lung cancer spectra than the control group counterpart. The latter peaks, representing the nucleic acids and carbohydrates, seen between the regions of 1000 cm^{-1} and 1100 cm^{-1} show a clear disparity in their heights between the cancer and healthy spectra. As a result of the high sensitivity and specificity achieved from FTIR and its non-

invasive technique the authors concluded that FTIR would potentially be a great tool for lung cancer diagnosis.

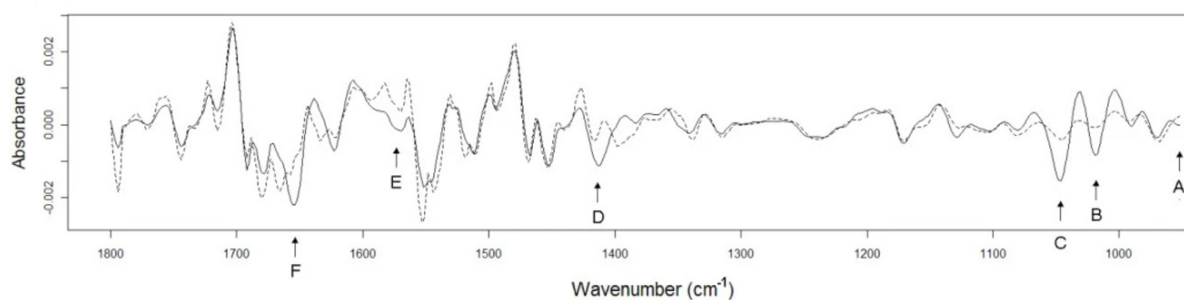


Figure 21. Spectra achieved for lung cancer and normal sputum whereby the significant peaks are labelled A-F (Modified from Lewis et al., 2010).

Another example of the benefits of FTIR in the cancer field was shown in the research study by Fale et al. (2015). In this paper, using FTIR, three cancer cell lines were tested for their response to the anticancer drug doxorubicin as well as acquiring information about the mechanisms relating to resistance to anticancer drugs. The chemical changes which occurred from doxorubicin treatment on the live cells were emphasised on the FTIR spectra. On the FTIR spectrum Fale et al. (2015) also pointed out the regions for nucleic acids and carbohydrates on the spectra (as seen in Figure 20 above) where changes occurred and could be related to the mechanism of resistance for doxorubicin to these specific cancer cells. Therefore, obtaining information about mechanisms of resistance through FTIR is a benefit for researchers especially as it can aid the field of drug development.

By probing the drug-cancer cell interactions at a single cell level, subsequent biological changes within the cell will be monitored using infrared spectroscopy. The spectral signatures of each drug will be examined as well as looking for additional features indicating synergistic action when drugs are used in combination.

Chapter 3 Introduction to lipid membranes and modelling

3.1 Cell membranes

3.1.1 Background

The lipid membrane plays a significant role for cells as it is used to preserve the cellular architecture in addition to the cellular structure (Casares et al., 2019). The purpose of the lipid membrane is to surround the cell acting as a barrier enabling selective permeation of molecules. While the cells also depend on the lipid membrane for energy storage and signalling purposes, it also compartmentalises the space inside cells (Casares et al., 2019; Shahane et al., 2019). A simplistic schematic of the overall structure of a lipid bilayer is provided in Figure 22. Here it can be seen that polar head groups and a hydrophobic core makes up the basic structure of lipid bilayers as well as cholesterol (Bernardino de la Serna et al., 2016).

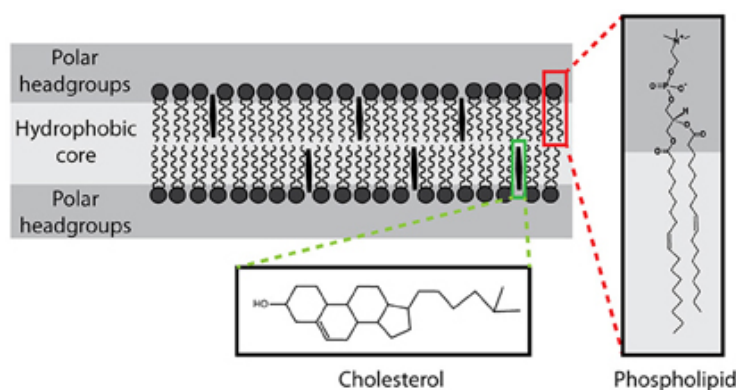


Figure 22. Simple schematic which shows the basic structure of a lipid bilayer (Bernardino de la Serna et al., 2016).

The fluid mosaic model is one of the most widely accepted models used to describe the organisation of biological cell membranes which was proposed by Singer and Nicolson (1972). This model suggests that the cell membrane is composed of a lipid bilayer whereby the lipids are amphipathic; have both hydrophobic and hydrophilic properties which is the case for the phospholipids, glycolipids, and sterols. The lipid bilayer also contains embedded integral and peripheral proteins and both these lipids and proteins are described to be in constant motion and free to move between the bilayers (Goñi, 2014). Research has gone into further developing this model and this has seen the addition of membrane domains as well as

formation of curvature and pores among others, all which enhances the complexity of the membrane and increases its functioning (Goñi, 2014; Nicolson, 2014; Zalba & ten Hagen, 2017).

Lipids form bilayers (i.e., the basic structures of the plasma membranes of cells) similar way as surfactants form micelles when placed in water. It is a result of the lipids amphipathic nature which leads to bilayer formation in an aqueous environment, with the tails at the core surrounded and protected by the head groups facing water (Hanafy et al., 2018; Zalba & ten Hagen, 2017).

Furthermore, depending on the structure of lipids, there is a curvature and distortion of the membrane (Zalba & ten Hagen, 2017). While the phospholipids phosphatidylcholine (PC) and sphingomyelin (SM), which possess more larger head groups, have a cylindrical shape and form lipid bilayers in an aqueous solution, phosphatidylserine (PS) and phosphatidylethanolamine (PE) phospholipids are referred to as 'cone shaped lipids', which have smaller head groups in comparison, and these bring about a negative curvature and distortion to the membrane overall (Escribá et al., 2008).

Although phospholipids have the cone shaped and cylindrical shaped structures, cholesterol is much more of a flat molecule. This flat structure allows it to fit into the lipid bilayers between the glycolipids and the sphingolipids with the hydrocarbon chain at the centre of the bilayer (Song et al., 2014).

3.1.2 Asymmetry and lipid content of normal vs cancer lipid membranes

The lipid components of the lipid bilayer are not in equal proportions. Generally glycolipids found on the extracellular leaflet form only about 2% of the complete membrane whereas sterols, particularly cholesterol and the phospholipids are found in considerably higher concentrations in comparison (Cooper, 2000).

The composition of lipids between the intracellular and extracellular leaflets of lipid bilayers is known to be asymmetrical (Zalba & ten Hagen, 2017; Zwaal et al., 1977). In a normal cell membrane, the extracellular leaflet is largely enriched with lipids such as PC and SM while

greater numbers of PE and negatively charged PS are found occupying in its inner leaflet, as demonstrated in Figure 23 (Alves et al., 2016; Llado et al., 2014; Shahane et al., 2019; Zalba & ten Hagen, 2017). In the cancer membrane represented in Figure 23, more charged PS lipids are found on the extracellular leaflet while higher numbers of PC are found in the intracellular leaflet (Alves et al., 2016; Rivel et al., 2019).

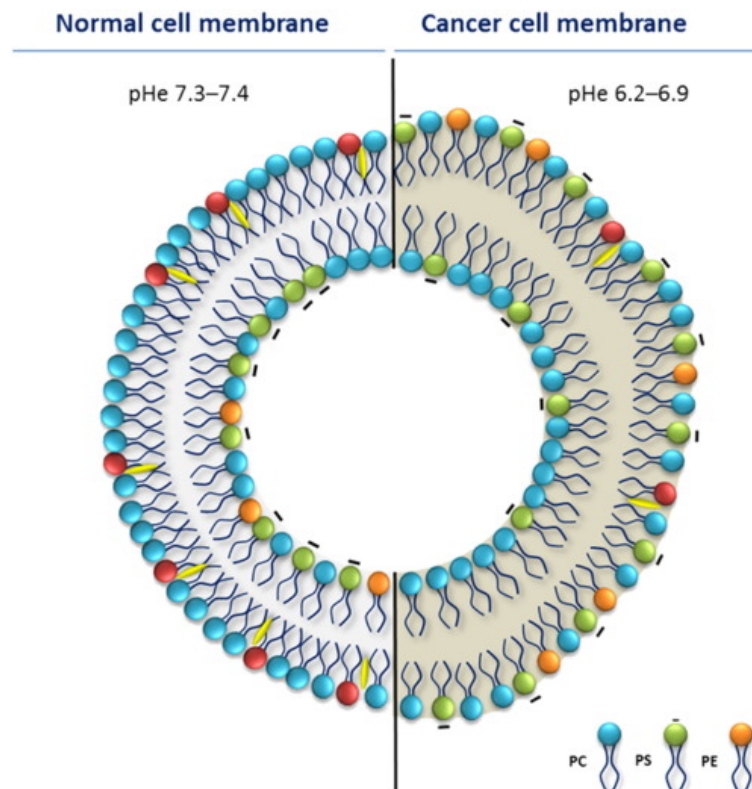


Figure 23. Lipid membrane compositions of a healthy and cancer cellular membrane. The extracellular pH levels for both cell membranes are also reported (Alves et al., 2016).

3.1.3 Membrane fluidity alteration in the cancer membrane

The cell membrane fluidity is affected by the overall temperature as well as lipid content of cholesterol and unsaturated phospholipids.

Zalba and ten Hagen (2017) have stated lipids are able to change from the state of order to disorder when they are at the transition temperature. There is not a specific transition temperature value as this itself alters depending on the lipid types and their amount present in the membrane. For example, for POPC and POPE lipids transition temperatures identified by molecular dynamics simulations are in a range of 270 to 280 K (Leekumjorn & Sum, 2007). The experimental transition temperature values for both POPE and POPC achieved are 25 °C

(298 K) and $-2\text{ }^{\circ}\text{C}$ (273.15 K), respectively (Lopes et al., 2018; Silviu, 1982). The transition temperature for PSM is much higher, about $38\text{ }^{\circ}\text{C}$ (311 K) (Arsov et al., 2018; Bunge et al., 2008). Therefore, membranes with different lipid content should exhibit different transition temperatures. Below the transition temperature the membrane is more rigid and ordered as the lipids are more tightly packed together while above the transition temperature the authors mention that the membrane is less tightly packed, disordered and is therefore more fluid. At physiological temperature ($\sim 310\text{ K}$) membranes are in liquid disordered state to maintain lipid lateral mobility (Zalba & ten Hagen, 2017).

Saturated phospholipids only possess single bonds, their tails are relatively stretched out and straight, and these can therefore be packed more ordered and tightly together making the membrane more rigid. On the other hand, unsaturated phospholipids have at least 1 *cis* double bond in their tails which eludes them from getting tightly packing resulting in a more disordered fluidic membrane (Nicolson & Ash, 2014; Subczynski & Wisniewska, 2000).

In phospholipid plasma membranes, small and flat cholesterol molecules increase ordering of lipid tails, increase bilayer thickness and fluidity of membranes and induces phase separation which leads to lipid raft formation (Redondo-Morata et al., 2012; Yang et al., 2016; Zalba & ten Hagen, 2017). Cholesterol is also able to flip flop between the bilayers as it is more mobile than other lipids. By doing this it relaxing the stresses found in the bilayer as it allows balance in the area found between the leaflets (Gu et al., 2019).

Some of the differences in the lipid content between the cancer and normal membrane can also be observed in Figure 23. For example, a reduction in the levels of SM present as well as up to 7 times more PS lipids can be seen in the extracellular leaflet of many cancer membranes when compared to normal cell membranes (Llado et al., 2014; Rivel et al., 2019). However, there are no general patterns associated with cancer-related changes in membrane lipid profile, the reported changes are different for various cancers. Some of the differences in lipid content within cancer cells compared to normal healthy cells are described ahead. The changes for leukemic cells are associated with lower content of cholesterol and SM, and higher content of phospholipids with mono- and polyunsaturated acyl chains (Koizumi et al., 1980; Pratt et al., 1978; Shinitzky, 1984; Van Blitterswijk et al., 1982). In hepatoma cells, the

opposite change was observed, where the fraction of cholesterol was reported higher than in normal hepatocytes (Cinosi et al., 2011; Mahler et al., 1988; Shinitzky, 1984; Van Hoeven et al., 1975). Sok et al. (1999) studied membrane fluidity of human lung cancer by electron paramagnetic resonance (EPR) and concluded that the membranes of tumour tissues were more fluid, than those of normal lungs. Similar conclusions regarding increase of membrane fluidity were also made by Kozłowska et al. (1999) on their study of melanoma cells.

The studied literature data show that cholesterol metabolism is altered in cancer cells, and this can lead to variations in the amount (whether higher or lower) of cholesterol which is found in cancer cells. When the cholesterol content of cells is found to be lower some of the effects this has is that the cell membranes can be deformed a lot more easily and results in the cell becoming highly metastatic (Zalba & ten Hagen, 2017). Shahane et al. (2019) have additionally mentioned that reduction in the levels of cholesterol in the membrane can lead to disorder in the lipid hydrocarbon chains and also can increase the lateral diffusion for the lipids along the membrane. When levels of cholesterol are higher than normal it can result in a much more rigid cell membrane making it far less able to be permeated as is the case for multi-drug resistant cells (Zalba & ten Hagen, 2017).

As stated by Alves et al. (2016), the membrane fluidity upon malignant transformation depends on the lipid changes and can change in either direction. Lymphomas and lung carcinoma cells show higher membrane fluidity than their normal counterparts. Contrary, other cancer cells such as hepatoma cells shows decreased membrane fluidity. Contradictory statements regarding changes of membrane fluidity are found in literature. In the review from Shinitzky (1984) on membrane fluidity in malignancy the author states that: “it appears that, with a few exceptions, tumour cells from solid tissues (e.g., hepatoma) have a lower membrane fluidity than their normal analogues, while tumours of flowing cells (e.g., leukaemia) have a higher membrane fluidity than their normal analogues”, while Csoboz et al. (2013) in their review on membrane fluidity and hyperthermia have stated the opposite: “Several solid tumours are characterised by the higher fluidity of their cell membranes correlating with their proliferative and invasive potentials and their metastatic abilities”.

3.2 Molecular Dynamics Simulation

3.2.1 Background and theory

Molecular dynamics (MD) is a computer simulation method commonly utilised for studying biomolecular systems and it was first performed on folded proteins in the late 1970s (Hospital et al., 2015). It is used to calculate the movement and spatial position of all atoms and molecules in a molecular system based on Newton's law of motion (De Vivo et al., 2016; Durrant & McCammon, 2011; Hollingsworth & Dror, 2018). Additionally, MD simulations can predict, to an atomic level, the response from biomolecules to various perturbations including protonation and mutation (Hollingsworth & Dror, 2018).

MD simulations have proven to be useful in the field of drug discovery. Liu et al. (2018) have stated that an abundance of knowledge regarding protein and ligand interactions can also be obtained. This information is therefore not only important for our understanding of the biomolecular systems and the protein and ligand interactions but also in accelerating the drug discovery and drug design process (Adelusi et al., 2022). Some of the areas of the drug discovery process where MD simulation is found to be useful in is lead optimisation and virtual screening (Hollingsworth & Dror, 2018; Liu et al., 2018). Considering lipids in the field of drug discovery, MD simulations can give insights in membrane organisation and properties including molecular orientation, arrangement of headgroups and tails, interactions of membranes with solvents and small molecules (including drugs) and larger molecules such as bio-polymers, proteins and DNA (Feller, 2000; Harayama & Riezman, 2018; Hollingsworth & Dror, 2018).

In recent works, MD simulations are habitually being used as a means of interpreting, validating and even guiding experimental work (Hollingsworth & Dror, 2018). Various levels of detail can be achieved through MD simulations such as atomistic and coarse-grained. While atomistic MD simulation models are effective for mimicking actual biomolecular systems, coarse grained models are also highly popular especially for when longer simulation times are required or when larger systems occupying up to 500,000 atoms need to be simulated (Hospital et al., 2015).

MD simulations are based on the numerical solution of Newton's equations of motion for a system of many interacting atoms. Newton's second law of motion is simple, and it is depicted in Equation 1:

$$\mathbf{F} = m \cdot \mathbf{a} \quad (1)$$

where F is the force acting on atoms, m is their mass and a is acceleration. However, in practice, we don't know the force and acceleration, but we know the interaction potentials between all atoms (defined prior simulation started), positions (initial coordinates) and the velocities (from previous simulation or assigned to all atoms using Maxwell-Boltzmann distribution for specified temperature). In order to solve this equation numerically, it is rewritten in a slightly more complex way. Forces acting on each atom can be calculated as a negative derivative of the potential $V(r)$ with respect to positions of all atoms as seen in Equation 2:

$$\mathbf{F}_i = -\frac{dV(\mathbf{r})}{d\mathbf{r}_i} \quad i = 1, 2, \dots, N \quad (2)$$

The acceleration (a) is a derivative of velocity with respect to time and the velocity (v) is a derivative of positions with respect to time.

$$\mathbf{a} = \frac{d\mathbf{v}}{dt} = \frac{d^2\mathbf{r}}{dt^2} \quad (3)$$

$$\mathbf{F}_i = -\frac{dV(\mathbf{r})}{d\mathbf{r}_i} = m_i \frac{d\mathbf{v}_i}{dt} = m_i \frac{d^2\mathbf{r}_i}{dt^2} \quad (4)$$

whereby the $V(r)$ is the sum of all interaction potentials from the force fields.

$$V(\mathbf{r}) = V_{\text{bonded}}(\mathbf{r}) + V_{\text{non-bonded}}(\mathbf{r}) \quad (5)$$

The force on each atom depends on the positions and speeds of other atoms in the systems. The atoms are moved in correspondence with Newton's law of motion by little time steps (approximately 10^{-15} s = 1-2 fs, the time scale for real molecular motions) for atomistic simulations. All moves of the atoms are saved as atomic trajectory that is analysed after simulations are completed (Abraham et al., 2014; Hollingsworth & Dror, 2018; Hospital et al., 2015).

The interaction potentials between atoms governs the behaviour of the system are called force fields (Lopes et al., 2017). Different variations of force fields exist each consist of distinctive sets of interaction parameters and connectivity of atoms as well as approximating overall energy of the system (De Vivo et al., 2016). Parameters of force fields consist of the atom types identifying all the atoms which are present in the molecule. Additional to atom mapping, the parameters describe **bonded** interactions which occur within the molecule and **non-bonded** interactions which occur between other molecules. Bonded interactions refers to the bonds, angles and dihedrals and non-bonded interactions refer to the short-ranged van der Waals parameters where the data is achieved experimentally or long ranged electrostatic interactions where the charges would be derived from quantum mechanics calculations (Notman & Anwar, 2013). A diagram summary of the interactions which take place can be found in Figure 24 which has been adapted from Notman and Anwar (2013). Force fields specific for biological molecules such as CHARMM, OPLS and AMBER contain parameters which can be used to study lipids, proteins, nucleic acids, and drug molecules (Durrant & McCammon, 2011; Lopes et al., 2017).

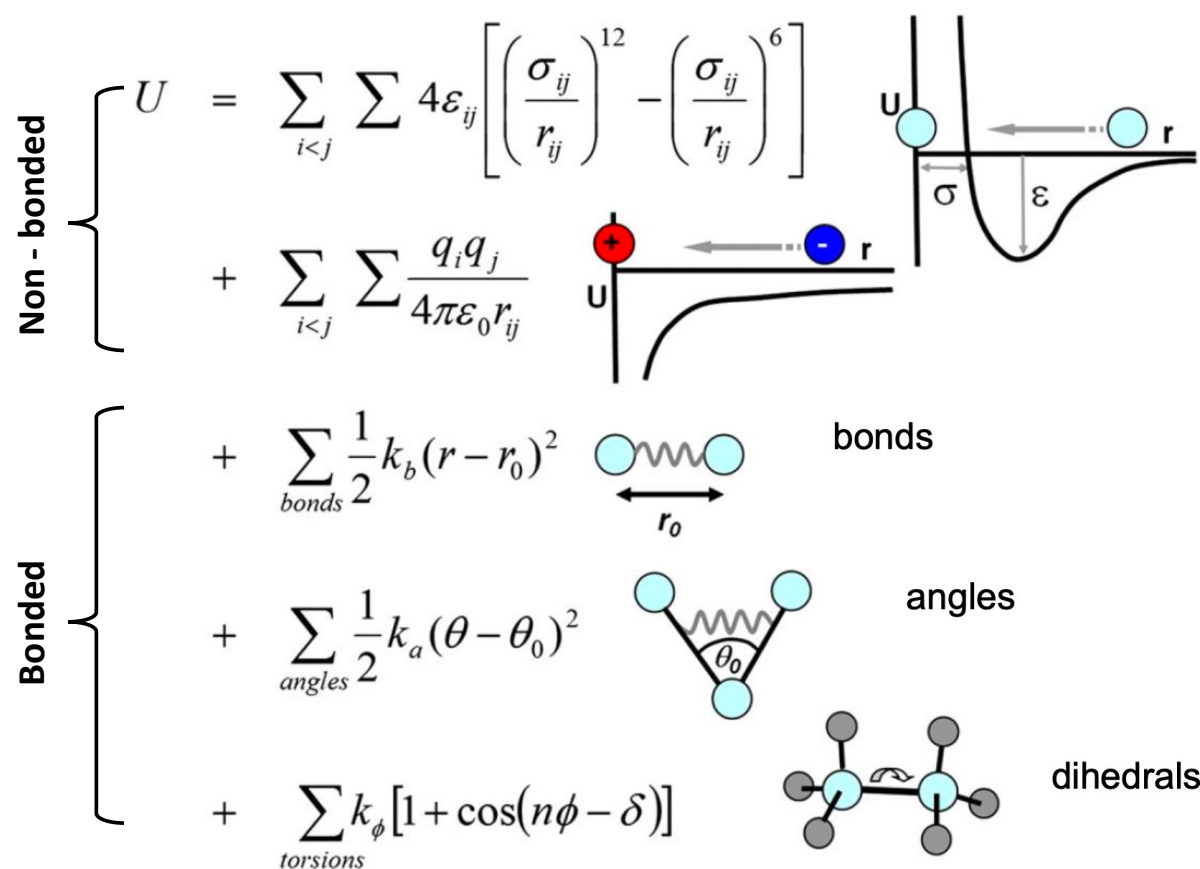


Figure 24. Summary of the overall interactions which take place within or between a molecule (Notman & Anwar, 2013).

The general molecular dynamics algorithm follows the following steps (Abraham et al., 2014):

1. **Initial input conditions.** These include specifying interaction potentials $V(r)$ as a function of atom positions, positions (r) of all atoms in the system and the velocities v of all atoms in the system. Interaction potentials are required to calculate forces whereas positions (coordinates) and velocities are required to move the atoms during simulation with a small-time step Δt .
2. **Calculation of all forces.** The forces are calculated from the potentials using Equation 2. The forces are calculated between all non-bonded atom pairs (for all atoms) and bonded atom pairs (include only up to three nearest neighbouring atoms in the same molecule).

$$\mathbf{F}_i = \sum_j^{\text{all atom}} \mathbf{F}_{ij}(\text{non-bonded}) + \sum_k^{k \leq 3} \mathbf{F}_{ik}(\text{bonded}) \quad (6)$$

3. **Simulation of atom movements.** The Newton's equations of motion for all the atoms in the system are solved numerically using Equation 4 in each time step Δt . The system configuration is updated.
4. **Writing output data.** The system parameters (new positions, velocities, forces, all components of system energy, temperature, pressure, etc.) are written in a trajectory file that further used for analysis.
5. **Data analysis.** Final trajectory and coordinate files are used for post-processing analysis (for example calculating average temperature, energies, density distributions, and system-specific analysis such as order of the lipid tails).

The steps 2-4 are repeated for required number of time steps. Typical simulation time for lipid membrane nowadays is about 100-500 ns (Botan et al., 2015), that using a typical time step of 2 fs gives between 50 to 250 x 10⁶ time steps.

3.2.2 Overview of membrane models

In this research project atomistic molecular modelling was used to model cancer and healthy membrane models and study their interactions with drugs. The models used in this research project are however simple and generic due to lack of information on RT cell membranes such as which lipid types and their specific concentrations in the membrane. Simplistic model

membranes are found more frequently in computational research papers whereby only a few select number of lipids are studied. In the research paper from Van der Paal et al. (2017), the authors only used the two lipid types, CHOL and DOPC. Additionally, Wadhwa et al. (2021) studied the lipids POPC, POPS and CHOL when looking at the effect of the drugs withaferin-A and withanone across a model cell membrane.

Complex multi-component membrane models for cancer cells were proposed in a range of recent molecular dynamics studies, (Andoh et al., 2016; Andoh et al., 2013; Klähn & Zacharias, 2013; Rivel et al., 2019; Shahane et al., 2019). All these studies based their models on different cancer types, where lipid compositions used in simulations were adopted from experimental data. Andoh et al. (2013) focus on the plasma membranes of normal murine thymocytes and leukemic GRS1 cells and mouse hepatocytes and hepatomas (Andoh et al., 2016). The authors based their models on the experimental research data from Van Blitterswijk et al. (1982) for leukaemia and Van Hoeven et al. (1975) for hepatomas. The model membranes used in their calculations comprised 23-25 kinds of lipids with symmetric distribution between the leaflets. Rivel et al. (2019) studied permeation of anticancer drug cisplatin through model membranes of normal and cancer cells. The model for normal membrane was adopted from the experimental values for mammalian erythrocyte membrane (Daleke, 2008) and contain 5 lipid types, PC, PE, PS, SM, and CHOL. Normal membrane considered two asymmetric leaflets and the associated changes upon canceration focused on the loss of asymmetry and re-distribution of lipids among the leaflets. Same lipid types, PC, PE, PS, SM, and CHOL were used by Klähn and Zacharias (2013) in their complex asymmetrical models for healthy and cancer eukaryotic cells, (M-Eukar) and (M-Cancer) based on the experimental data for lipid composition of erythrocyte membranes, published by Zachowski (1993). Further, Shahane et al. (2019) adopted these models in their study of key properties of different membranes (including bacterial membrane). In the two latter studies the models for both cancer and normal membranes retain asymmetry in lipid distribution in outer and inner leaflets.

3.2.3 Lipid choice and membrane compositions in this project

No doubts that complex multi-lipid computational models with embedded asymmetry in lipid distribution between the leaflets resemble better the real cancer and normal cell membranes. However, so far there are no literature data available describing lipid composition of

membranes of RT cell making it impossible to create an RT-specific model. Also, multi-lipid membranes are expected to contain large amount of lipids in total to have all the lipids represented in sensible amounts. This leads to increase in system size (including lipids and water molecules) and consecutive increase in computational time. Another difficulty in multi-lipid systems is that it become difficult to observe and evaluate changes associated with specific lipid type.

Based on the publication by van Meer and de Kroon (2011), three lipids which represented the three most common lipid types as shown in Figure 25, phospholipids, sphingolipids and sterols, were chosen. This included POPC which represented phospholipids as well as PSM and CHOL each representing sphingolipids and sterols, respectively.

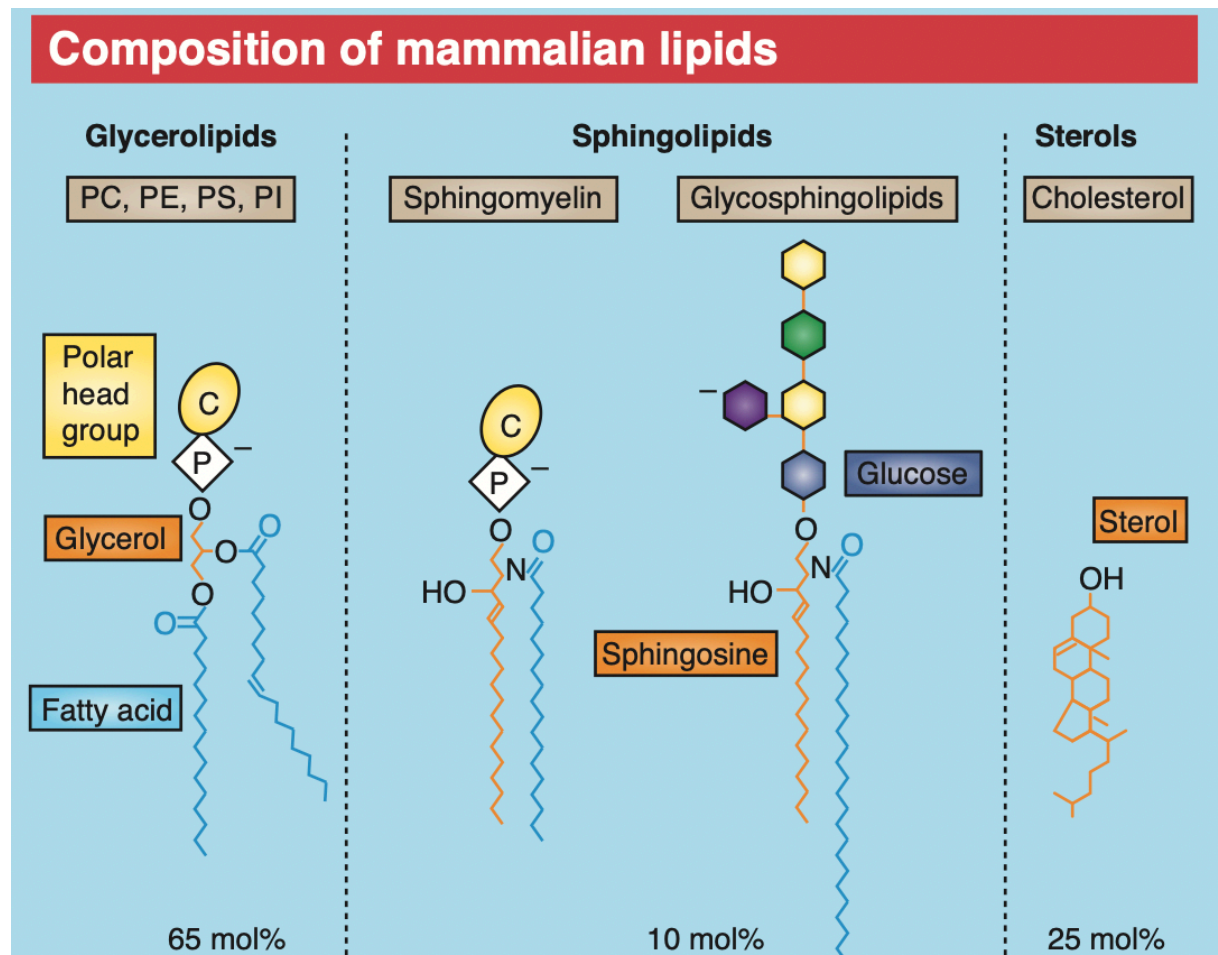


Figure 25. Composition of the main mammalian lipids (van Meer & de Kroon, 2011).

3.2.3.1 1-Palmitoyl-2-oleoylphosphatidylcholine (POPC)

The structure of POPC consists of two non-polar hydrocarbon chains/tails each which have different carbon lengths (C18:1-C16:0). As a typical glycerophospholipid, one of the tails are saturated, which in this case is the shorter 16-carbon chain while the 18-carbon chain is unsaturated due to the presence of a *cis* double bond between the 9th and 10th carbon atoms as circled red in Figure 26a (Bunge et al., 2008; Watanabe, 2018). Lipids like POPC, which are cylindrical in shape with larger head groups, are very commonly found in the lipid membrane as out of the three main lipid types mentioned above, these constitute up to 65% of the lipid membrane composition (van Meer & de Kroon, 2011; Zalba & ten Hagen, 2017).

3.2.3.2 Palmitoylsphingomyelin (PSM)

The structure of the sphingomyelin PSM, as seen in Figure 26b below, is made up of two sets of hydrocarbon chains/tails both which are saturated in comparison to POPC (Watanabe, 2018). Niemelä et al. (2004) have described these as a sphingosine chain which is 18 carbons long and a palmitoyl chain which is shorter at 16 carbons in length. The sphingosine chain contains a *trans* double bond between the 4th and 5th carbon atoms as well as a hydroxyl group which are both highlighted with red circles on the structure. Both structures of POPC and PSM contain a polar headgroup, where the phosphate group is linked to choline as highlighted by the red rectangles drawn in Figure 26a and Figure 26b. Moreover, the saturated tails in the structure of PSM allows it to make more rigid membranes than that of POPC.

3.2.3.3 Cholesterol (CHOL)

A rigid tetracyclic ring system occupies the main structure of cholesterol. It is a steroid alcohol with a short, branched hydrocarbon chain and a hydroxyl group shown by the red circle in Figure 26c (Bunge et al., 2008; Martinez-Seara et al., 2010). This is a common component found in lipid membranes and like PSM, this is also responsible for adding rigidity to the membrane. Furthermore, it is primarily found in between the hydrocarbon chains of specifically sphingolipids acting as a sort of glue allowing the lipid rafts to stay in place (Simons & Ehehalt, 2002).

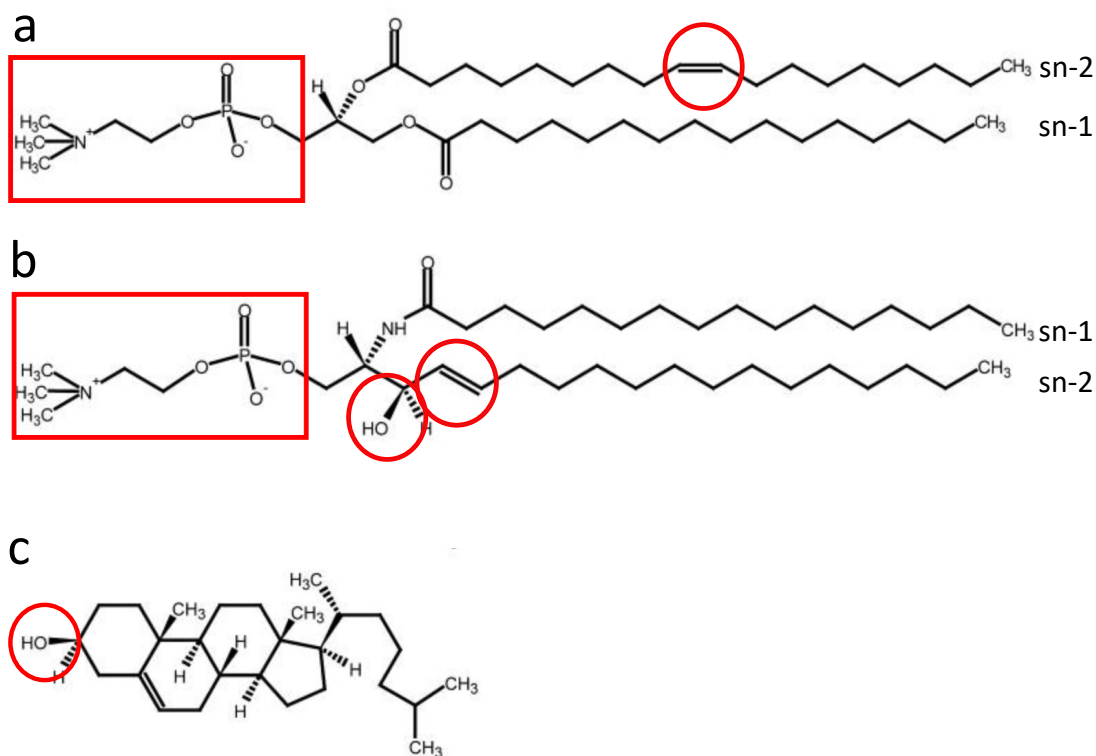


Figure 26. The chemical structures of the specific lipids which have been used for the simulations in this research project. (a) POPC (b) PSM (c) Cholesterol (Bunge et al., 2008). For both POPC and PSM sn-1 and sn-2 are used to refer to tail 1 and tail 2, respectively.

In this project we focus only on three lipids, POPC, PSM and CHOL, keeping distribution of them between the leaflets symmetrical. Our membrane compositions are as follows: cancer (flexible) membrane 65% POPC, 10% PSM, 25% CHOL; rigid (normal) membrane 65% PSM, 10% POPC, 25% CHOL; intermediate (normal) membrane 37.5% POPC, 37.5% PSM, 25% CHOL. The levels of POPC and PSM were inverted with the higher amount in the cancer and healthy rigid membrane systems, respectively. The intermediate membrane considered in this research project contained equal amounts of both POPC and PSM. As research has already been done on testing different concentrations of CHOL by other groups (Van der Paal et al., 2017), the amount of CHOL considered for each membrane remained the same for each mixed membrane system.

3.2.4 Molecular dynamics software

Lipid membranes and their interactions with drugs were modelled using GRONingen MACHine for Chemical Simulation (GROMACS, www.gromacs.org), the 2018.4 molecular dynamics

(MD) simulation package (Van Der Spoel et al., 2005). There are many advantages associated with the use of GROMACS over other software packages such as AMBER (Assisted Model Building with Energy Refinement) <https://ambermd.org> (Case et al., 2005). This includes it being a free and open-source software allowing the academic use of this MD package without any restrictions, unlike AMBER which can be very costly to use (AMBERMD, 2022). It is widely used for analysis of biomolecular simulations such as proteins and lipids as well as for drug molecules. GROMACS has also been used in the field of chemistry particularly for analysis of inorganic and organic substances. Moreover, the development of the GROMACS software over the years has now led to simulation times for much larger systems accomplishable within a week or two. GROMACS is equipped with multiple system building and analysis tools which allows its code to be much easier and simpler to use. Another advantage associated with this software package is that it allows both coarse grained and atomistic levels of detail to be obtained about the systems (Abraham et al., 2015; Lee et al., 2016; Nian et al., 2021; Pronk et al., 2013; Van Der Spoel et al., 2005).

Chapter 4 Aim and Objectives

4.1 Aims

The aims of this research project are to investigate the childhood cancer, Extracranial Rhabdoid Tumours (RT) and its sensitivity to a number of current and repurposed drugs. Specifically, we aimed to investigate (1) the cytotoxicity of the drugs carvacrol and loratadine to the A204 cell line individually and in combination and (2) the interactions of these drugs with cancer and healthy cell membrane lipids on an atomistic level.

4.2 Objectives

The cytotoxicity of both drugs individually and in combination was assessed experimentally using the cell viability/cytotoxic MTT assay against the A204 extracranial RT cell line. The results achieved for IC_{50} were then compared to those obtained in literature for our drugs as well as for our positive control cisplatin, a drug currently used in cancer treatment. Moreover, atomistic MD simulations were completed for the model cancer and healthy membranes in water before and after the addition of drugs individually and in combination.

Chapter 5 Methodology

5.1 Experimental Methodology

5.1.1 Aseptic techniques

The use of aseptic techniques (1% Virkon and 70% ethanol) for this experiment ensured that the A204 cell line was not affected by the means of any contamination. All equipment used during experimental work was sterilised beforehand. Additionally, the cell cultures were incubated at 37 °C within a humidified atmosphere at a 5% CO₂ level.

5.1.2 Chemicals

The drugs for this experimental study, carvacrol and loratadine were both purchased from Sigma Aldrich and stored at room temperature. Cisplatin was bought from Insight Biotechnology and was kept stored at 4 °C. MTT reagent, Thiazolyl Blue Tetrazolium Bromide, trypsin-EDTA and penicillin/streptomycin were also purchased from Sigma Aldrich (Gillingham, UK). The MTT reagent was stored in a fridge between 2 and 8 °C while the others were both stored at -20 °C. The cell culture medium, Roswell Park Memorial Institute (RPMI) 1640 as well as L-Glutamine were both purchased from Lonza (Manchester, UK) and stored at room temperature and -20 °C respectively. Fetal bovine serum was bought from Thermo Fischer Scientific (Altrincham, UK) and was also stored at -20 °C.

5.1.3 Cell culture and drug treatment

A live flask and a frozen cryovial of extracranial RT (A204 cell line) cells were gifted from Newcastle University (Newcastle upon Tyne, UK). These A204 cells were grown in RPMI-1640 medium which was supplemented with 10% FBS, 1% penicillin/streptomycin and 1% L-Glutamine. These cells were sub-cultured up to 2 to 3 times a week depending on their confluency as was done following the protocol provided by Newcastle university.

Once the A204 cells reached approximately 80 – 90% confluency, using 1.5 mL trypsin-EDTA the cells were detached from the flask and centrifuged at 1200 rpm (revolutions per minute) for 5 minutes to get a pellet. This pellet of cells was then re-suspended in complete RPMI media as a single cell suspension. An equal 1:1 dilution of the A204 cells and the trypan blue solution was placed into the Neubauer Chamber and the cells were counted under the

microscope. 10,000 cells per well were then seeded onto a 96-well plate for 24 hours allowing them to adhere. Then these cells were further incubated at various concentrations of carvacrol (0.03125 mM, 0.0625 mM, 0.125 mM, 0.25 mM, 0.5 mM and 1mM) and loratadine (5 μ M, 10 μ M, 20 μ M, 40 μ M, 80 μ M and 160 μ M) for 72 hours. The negative control group contained just the A204 cells with complete RPMI media while the positive control group was treated with only cisplatin (0.8 μ M, 1.56 μ M, 3.13 μ M, 6.25 μ M, 12.5 μ M and 25 μ M).

5.1.4 Analysis

The IC_{50} concentrations of the drugs in the experiment were obtained using the MTT colorimetric assay. Following the 72-hour incubation, 50 μ l MTT reagent was added to the 96-well plate which was then left to incubate for an additional 3 hours. Media and MTT reagent were aspirated from the wells and 200 μ l DMSO (dimethyl sulfoxide) was added. The absorbance was then measured using a Multiskan Ascent reader V1.24 (Thermo Fisher Scientific) for the wells at 540 nm (A_{540}) and 690 nm (A_{690}). All the experiments in this research project were set up to be completed in biological and technical triplicates. The cell viability was calculated using Equation 7 below:

$$\text{Cell viability \%} = \frac{\text{Sample } A_{540} - \text{Sample } A_{690}}{\text{Negative control } A_{540} - \text{Negative } A_{690}} \times 100 \quad (7)$$

After achieving the IC_{50} values for both carvacrol and loratadine, for combination the A204 cells were treated with a 7-set serial dilution, with the approximate IC_{50} for carvacrol (0.0625 mM, 0.125 mM, 0.25 mM, 0.5 mM, 1mM, 2 mM and 4 mM) and loratadine (3.125 μ M, 6.25 μ M, 12.5 μ M, 25 μ M, 50 μ M, 100 μ M and 200 μ M) being added in the fourth (mid-point) dilution as shown in bold for the concentrations. The above steps for MTT assay were then repeated after the 72-hour incubation period. Analysis was conducted using the GraphPad Prism version 8 software. Probability values of < 0.05 were considered significant. Previous studies in literature have also found using the CalcuSyn software a reliable method in order to carry out analysis of drug combination effects (Panwar et al., 2020). As a result of this the CalcuSyn software has also been used in this research project to analyse the effect of the loratadine and carvacrol drug combination on the A204 cells. This allows us to determine whether the drug combination effect is possibly synergistic, additive, or even antagonistic.

5.2 Computational Methodology

5.2.1 Model systems composition

In this project three membrane compositions were considered. The membrane systems represented a cancer (flexible) membrane and two varieties of healthy membrane with one being rigid and the other an intermediate healthy membrane system. All lipid membrane system consisted of 128 lipid molecules with 64 molecules occupying each leaflet and additionally hydrated with 5120 water molecules in total. Drugs studied in this project are carvedilol and loratadine. The drugs were studied individually (8 or 16 carvedilol molecules or 8 loratadine molecules) and in combination (16 carvedilol + 8 loratadine molecules). The drugs were added to the water phase of each membrane to study unbiased drug-membrane interactions.

For the cancer lipid membrane model, the lipid composition was as follows: 65% POPC, 25% CHOL and 10% PSM. A higher percentage of POPC in the cancer membrane allowed this membrane system to be more fluid. For the rigid healthy membrane, the amount of POPC and PSM was reversed as this consisted of 65% PSM, 25% CHOL and 10% POPC. Higher percentage of PSM in comparison to the cancer membrane allows for this rigidity in the healthy membrane. The intermediate healthy membrane had a lipid composition of 25% CHOL and equimolar concentrations of POPC and PSM at 37.5% each. In all lipid membrane systems, the amount of CHOL content remained the same while PSM and POPC content altered. A summary of the lipid compositions occupying the membrane systems is provided in Table 2.

Table 2. Lipid compositions of the membrane and drug systems investigated.

	Mol %			No. of lipids			CARV	LOR
	POPC	PSM	CHOL	POPC	PSM	CHOL	No. of carvacrol molecules	No. of loratadine molecules
MIX 1 (Cancer)	65	10	25	84	12	32	8 & 16	8
MIX 2 (Rigid, healthy)	10	65	25	12	84	32	8 & 16	8
MIX 3 (Intermediate, healthy)	37.5	37.5	25	48	48	48	8 & 16	8

5.2.2 Model system setup

The mixed lipid membrane models were constructed using the Chemistry at HARvard Macromolecular Mechanics-Graphical User Interface (CHARMM-GUI) membrane builder <https://charmm-gui.org/> (Jo et al., 2008). This online builder tool allows you to choose which specific lipids you would want your membrane system to consist of (POPC, PSM, CHOL), the amount of lipids in your membrane (128), number of water molecules (5120) among other things. The files were then saved and transferred to the School's HPC server for further equilibration and simulation (see details in the section 'simulation steps and parameters').

The structures of the drugs were found through screening the ZINC12 docking library database (Irwin & Shoichet, 2005; ZINC12, 2020). From this the co-ordinate MOL2 files for the drugs was obtained. The SwissParam website <https://www.swissparam.ch/> allowed topology files relating to the drugs to be generated, which were needed to correctly simulate the systems, once the MOL2 file was uploaded (SwissParam, 2020; Zoete et al., 2011). The topology files were then uploaded to the School's HPC server, which was used to carry out the simulations.

All simulations and analysis were carried out using GROMACS molecular dynamics package (version 2018.4) www.gromacs.org (Van Der Spoel et al., 2005) pre-installed in the School's HPC server. Once the membranes in water were fully equilibrated, this acted as the initial starting point for when the drugs (carvacrol and loratadine) were added individually and in combination. The drugs were added to the water phase of the membrane systems to assess interactions of the drugs with membranes and passive permeation of the drugs. The drug molecules were inserted into the membrane system using *gmx insert-molecules* GROMACS tool. To make space for the additional drug molecules being introduced, water molecules were replaced. As a result of this, the box size had to be slightly increased at the z axis. The water was then added back again by solvating the system using *gmx solvate* tool with the amount of water molecules lost in total after the addition of the drug molecules (total number of water molecules was kept 5120 through all simulations).

5.2.3 Simulation steps and parameters

The CHARMM36 force field was used to carry out the simulations for lipids and CHARMM22 was used for the drug simulations, together with the TIP3P water model. The lipid membrane systems all underwent the standard set of simulation steps (Energy minimisation, NVT-equilibration, NPT-equilibration, and several MD-runs in NPT ensemble) and post-processing analysis which are illustrated in Figure 27. The temperature throughout the simulations was kept constant (310 K, physiological body temperature) as well as the pressure (1 bar).

Energy minimisation (EM) was the first simulation which the mixed bilayer systems were subjected to. This simulation is relatively short, only taking up to 1 minute to complete and it works by utilising the steepest decent algorithm by GROMACS (Sommer et al., 2015). EM simulations were done in order to check the workings of the systems i.e., to adjust the bonds and angles within the molecules to prevent the system from crashing.

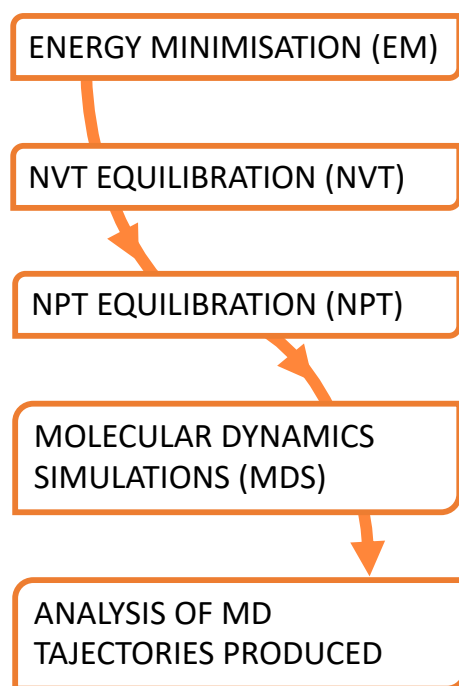


Figure 27. Simulation steps taken for each mixed membrane system.

Next was the canonical ensemble, NVT (constant number of particles, volume and temperature) equilibration simulation (Childers & Daggett, 2018). This was done at 200 ps and could take up to 2 hours on 8 cores depending on the size of the system which was being simulated.

Additionally, NVT was followed by the isothermal-isobaric ensemble, NPT which maintained a constant number of particles, pressure and temperature, at 10 ns and 20 ns simulation time (Wereszczynski & McCammon, 2012). For the initial 10 ns NPT simulation, Berendsen thermostat and barostat were used to control the temperature and pressure with a time constant of 5 ps (Lin et al., 2017). While Nose-Hoover and Parrinello-Rahman barostat were used with the second 20 ns NPT simulation. By having two different simulation times the volume during NPT simulations was able to alter to assist the equilibration of the systems. NPT simulations altogether could take up to 2 – 3 days to finish running, when ran on 12 cores depending on system size.

MD simulations, which were carried out last, were implemented from the same parameter principles as those which were found in the NPT ensemble simulations. The MD simulations were running in intervals of 50 ns on 12 or 16 cores depending on the number which were

free to use on the School's bioinformatics server. This could take up to a week or longer to finish. As a standard, after equilibration stages has completed, four sets of 50 ns (200 ns) MD simulations were carried out on each of the systems. The last 3 x 50ns simulation blocks were used for averages and standard deviation calculations. In a few cases, when longer simulations were needed to reach equilibrium additional MD simulations were carried out (up to 400 ns). The equilibrium was assessed by visualising the system using the Visual Molecular Dynamics (VMD) software and ensuring that the membrane X-Y cross-sectional area (relating to the area per lipid) had reached a plateau. Each simulation step needed to be done chronologically to prevent the system from crashing and ensure correct simulation results.

To run each simulation a set of two standard Gromacs commands were used, *gmx grompp*, that takes coordinate and parameters files and produces a binary topology file and *gmx mdrun* that runs the simulation using the previously created topology file. For convenience and to avoid mistakes, these two commands were combined in bash scripts for each simulation type. Once each simulation finished, the resulting coordinate and trajectory files were used for consecutive simulations and data analysis.

5.2.4 Analysis

The final three blocks from the MD simulations (50 ns each, 150 ns total) were used for the subsequent analysis of each membrane system. The assessed properties of the membrane were area per lipid, area compressibility modulus, tail order, density profiles, membrane thickness and hydrogen bonds. The analysis was conducted using the GROMACS tools available with the package. For density profiles and membrane thickness *gmx density* was used; for the tail order *gmx order* tool was used that computes the order parameter per atom for carbon tails; for hydrogen bonds *gmx hbond* tool was used that computes and analyses hydrogen bonds (Lindahl et al., 2021). Further details about each analysis can be found in the section for "Results and Discussion". Also, a visual representation when determining the possibility of the drugs (carvacrol and loratadine) permeating cancer and healthy lipid membrane systems was also provided using VMD software.

Chapter 6 Results and Discussion

In this research project both experimental and computational results were achieved. Experimental results yielded MTT assay analysis of IC_{50} achieved for the drugs, in addition to analysis of the combined drug effects from CalcuSyn. Computational results generated analysis of area per lipid, area compressibility modulus, tail order, mass density profiles and membrane thickness as well as analysis of hydrogen bonds for the cancer and healthy membrane systems.

6.1 Experimental Results & Discussion

6.1.1 MTT assay analysis

The anticancer properties of carvacrol and loratadine have been investigated against many different cancer cell lines some which have been outlined in the “Drug repurposing” section. Herein we studied the cytotoxic effects of carvacrol and loratadine against the extracranial RT A204 cell line.

6.1.1.1 Cisplatin

Firstly, cisplatin is an anticancer drug used widely for various cancers such as sarcomas, bones, soft tissue and even blood related cancers (Dasari & Tchounwou, 2014). As cisplatin is already marketed as an anticancer drug, this was used as the positive control serving as a method of validity for the rest of the data obtained of the other drugs against the A204 cell line. The concentration range used for cisplatin is mentioned in the “Experimental methodology” section.

The IC_{50} values were calculated using nonlinear regression (GraphPad Prism version 8) by using log-transformed drug concentrations plotted against the % cell viability. The log(inhibitor) versus normalized response-variable slope option was used for the IC_{50} calculation. From the cell viability graph in Figure 28, a steady course of decline in cell viability for cisplatin is found achieving an IC_{50} value of $2.53 \pm 0.39 \mu\text{M}$. Across literature data a range of results have been obtained for cisplatin such as an IC_{50} value of $0.5 \mu\text{M}$ against the H12.1 human testicular germ cell tumour cell line. As well as this, $1.64 \mu\text{M}$ for the 1777N Rpmet embryonal carcinoma cell line was found alongside an IC_{50} value of $4.70 \mu\text{M}$ against

1411HP testicular embryonal carcinoma cell line have been achieved (Schaffrath et al., 2017). As our results are found fairly between those IC₅₀ values in literature, it poses as a source of validity for our experimental work showing that the method employed for testing cytotoxic activity essentially works.

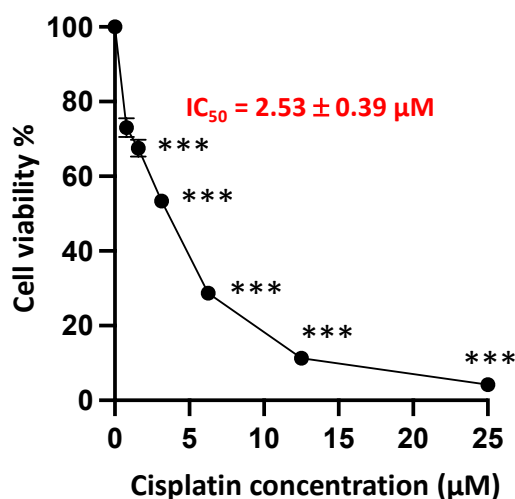


Figure 28. Cytotoxic effect and IC₅₀ value obtained of cisplatin against the A204 cell line.

6.1.1.2 Carvacrol and loratadine

The A204 cells were treated with various concentrations of carvacrol (0.03125 mM, 0.0625 mM, 0.125 mM, 0.25 mM, 0.5 mM, and 1 mM) and loratadine (5 µM, 10 µM, 20 µM, 40 µM, 80 µM and 160 µM) for 72 hours. We obtained the IC₅₀ value for each drug using the cytotoxic MTT assay and the results for this are shown in Figure 29 in the form of a cell viability graph. This graph reports the percentage of viable A204 cells found at the specific concentration in respect to both carvacrol and loratadine. The experimental IC₅₀ values which was achieved for carvacrol was 0.44 ± 0.07 mM, while loratadine had an IC₅₀ value of 26.42 ± 4.95 µM. The one-way ANOVA analysis gave a p-value of <0.01 for carvacrol concentrations of 0.125 mM (p= 0.003), 0.25 mM (p= 0.005), 0.5 mM (0.009), and a p-value of <0.001 for 1 mM. A p-value of <0.001 for the loratadine concentrations of 20 µM (0.0008), 40 µM, 80 µM and 160 µM was achieved while 5 µM had a p-value of <0.01 (p= 0.008). These p-values obtained demonstrate that these results are statistically significant.

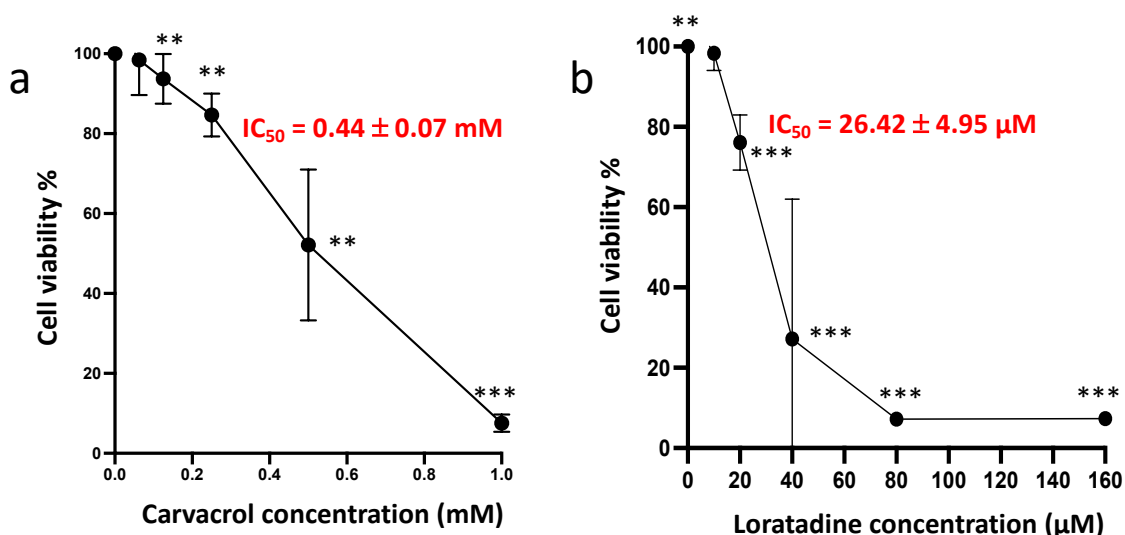


Figure 29. The cytotoxic effects and IC_{50} value achieved for (a) carvacrol and (b) loratadine against the A204 RT cell line are presented in the cell viability graph.

There has been a range of IC_{50} values which have been reported in literature for carvacrol and loratadine against various cell lines. These results which have been found are summarised in Table 3. For carvacrol this includes IC_{50} values of 0.38 mM (at 24 hours) and 0.244 mM (at 48 hours) obtained by Ozkan and Erdogan (2012) against the H1299 drug resistant lung cancer cell line. As well as this, in the paper by Günes-Bayir et al. (2018) an IC_{50} of $82.57 \pm 5.5 \mu\text{M}$ for carvacrol was achieved against human gastric adenocarcinoma while Melušová et al. (2014) obtained an IC_{50} of 425 μM against the HepG2 cell line. In a study by Wijesundara et al. (2021), it was found that the concentration range of 15.6, 31.3, 62.5, 125, and 250 $\mu\text{g}/\text{mL}$, was not cytotoxic to the human tonsil epithelium cells. When looking at the inhibitory potential of loratadine on L-lactic acid transport with the breast cancer cell lines Hs578T and MDA-MB-231 which express MCT1 and MCT4, it was found that the IC_{50} values were 10 μM and 61 μM , respectively (Yat et al., 2017). Additionally, in a study conducted on the pancreatic cancer MIA PaCa-2 cell line, loratadine has displayed an IC_{50} value of 326.4 μM (Desai et al., 2019). Therefore, after assessing what was already known about both drugs, a somewhat greater concentration range than that found in literature was chosen to be tested for carvacrol and a mid-range was tested for loratadine.

Table 3. Different IC₅₀ values achieved in literature for carvacrol and loratadine across different cell lines.

Drug	Cell line	IC ₅₀	References
Carvacrol	H1229 drug resistant lung cancer	0.38 mM & 0.244 mM	(Günes-Bayir et al., 2018; Melušová et al., 2014; Ozkan & Erdogan, 2012)
	Human gastric adenocarcinoma	82.57 ± 5.5 µM	
	HepG2 cells	425 µM	
Loratadine	Hs578T and MDA-MB-231 breast cancer	10 µM & 61 µM	(Desai et al., 2019; Yat et al., 2017)
	MIA PaCa-2 pancreatic cancer	326.4 µM	

Both drugs were found to produce cytotoxic effects against the A204 cells thus reducing the cell viability of the cells. However, it is seen that the effect of loratadine is much stronger than that produced of carvacrol (the concentrations used for loratadine are in the µM range, while those for carvacrol are in the mM range). Hence, higher concentrations of carvacrol are needed to achieve a 50% cell viability for the A204 cells compared to that of the required concentration for loratadine. Carvacrol exhibits relatively low levels of toxicity in general and is approved for use in the food industries, so is it potentially safe for consumption. Loratadine has been tested and it is regularly used as an antihistamine medication by an extensively wide range of people and as mentioned previously, it is well tolerated by the body. Therefore, the high concentration of carvacrol in comparison to loratadine which was needed to achieve a notable cytotoxic effect in terms of its IC₅₀ value was predictable.

A limitation associated with using the MTT assay, includes dissolving the insoluble formazan crystals in either DMSO (as used in this project) or another organic solvent like isopropanol as this can affect the results. Moreover, it is difficult to completely remove all floating formazan crystals and hence this can also interfere with the results due to the well-to-well errors. Additional colorimetric assays exist including the likes of the neutral red uptake assay, MTS

(5-(3-carboxymethoxyphenyl)-2-(4,5-dimethyl-thiazoly)-3-(4-sulfophenyl) tetrazolium) assay or even the WST-8 (2-(2-methoxy-4-nitrophenyl)-3-(4-nitrophenyl-5-(2,4-disulfophenyl)-2H tetrazolium, monosodium salt) assay. However Aslantürk (2017) has stated that even though all these other methods exist, the MTT assay is found to be by far the easiest, most cost effective and safest to use and has the highest reproducibility rate amongst the rest. Consequently, our decision to use the MTT assay for determining cell viability and cell toxicity can be justified.

6.1.2 Drug combination analysis, CalcuSyn

Upon the combination of different drugs, the outcome of this can be synergistic, antagonistic, or even additive. The term synergy refers to when the combination of the drugs is more effective than when used individually. When an antagonistic effect is achieved this would mean that the combination of different drugs is less effective than when they are used individually. While additive refers to no difference between the effect of the drugs produced individually or when they are in combination (Bijnsdorp et al., 2011).

By calculating the values for the combination index (CI) through the CalcuSyn software, this method allows us to determine whether the drug combination is effective. The values which are achieved for CI correspond to a certain symbol and description which can be found in Table 4. In simple terms, when the CI value is less than 0.8 a synergistic effect is achieved while a value for CI over 1.20 means an antagonistic effect is achieved and anything in between relates to an additive effect for the drug combination (Bijnsdorp et al., 2011).

Table 4. Combination index values, symbols they are associated with and the descriptions for classification of synergism or antagonism (Bijnsdorp et al., 2011).

CI	Symbol	Description
<0.1	+++++	Very strong synergism
0.1 – 0.3	++++	Strong synergism
0.3 – 0.7	+++	Synergism
0.7 – 0.85	++	Moderate synergism
0.85 – 0.9	+	Slight synergism
0.9 – 1.10	±	Nearly additive
1.10 – 1.20	-	Slight antagonism
1.20 – 1.45	--	Moderate antagonism
1.45 – 3.30	---	Antagonism
3.30 – 10	----	Strong antagonism
>10	-----	Very strong antagonism
Simplified CI values and their indication		
<0.8		Synergism
0.8 – 1.20		Additive
>1.20		Antagonism

Table 5 depicts the CalcuSyn results which have been achieved for the combined drug effects of carvacrol and loratadine. The CI values are presented for the combination at ED₅₀, ED₇₅ and ED₉₀ levels of inhibition. The D_m, m and r values have also been presented for all drugs and the combination. The value for D_m refers to the median effect/drug dose which is required for the 50% (ED₅₀) inhibition. The m value is used to explain the slope in terms of kinetic order and shape of the median effect curve. The r value characterises the median effect plots' linear correlation coefficient which in turn denotes conformity of the data to the mass-action law (Chou, 2010; Matthews et al., 2017).

From the combination of both drugs, the CI is provided in Table 5, it can be reported that for the ED₅₀ i.e., IC₅₀ levels of inhibition the CI value is less than 0.8. This therefore infers a very

strong level of synergy occurring between the drugs. On the other hand, a very strong antagonistic response is seen at the ED₇₅ and ED₉₀ i.e., IC₇₅ and IC₉₀ levels of inhibition.

Table 5. CalcuSyn output for the combination of carvacrol and loratadine.

	ED ₅₀	ED ₇₅	ED ₉₀	Dm	m	r
	CI values at					
Carvacrol	N/A	N/A	N/A	952.59056	3.37704	0.94685
Loratadine	N/A	N/A	N/A	37.79736	3.34412	0.94140
Combination	0.00360	1.32793	489.42767	0.13098	0.17612	0.59214

Output of results also included a dose-effect curve and median-effect plot as presented in Figure 30a and Figure 30b. Good correlation coefficients can be reported from the median effect plot for both carvacrol and loratadine as well as the combination. The r values in Table 5 were 0.95, 0.94 and 0.59 for carvacrol, loratadine and the combination, thus obtaining a linear correlation coefficient and hence somewhat good level of conformity to the mass action law. For the dose-effect curve, an m value of more than 1 indicates a sigmoidal curve, less than 1 shows a flat sigmoidal curve and when the value is equal to 1 the dose-effect curve would be regarded as hyperbolic (Chou, 2010). As a result, both dose-effect curves for the carvacrol and loratadine are higher than 1 so the lines are sigmoidal, while for combination the dose-effect curve is a flat sigmoidal as the Dm value is greater than 1.

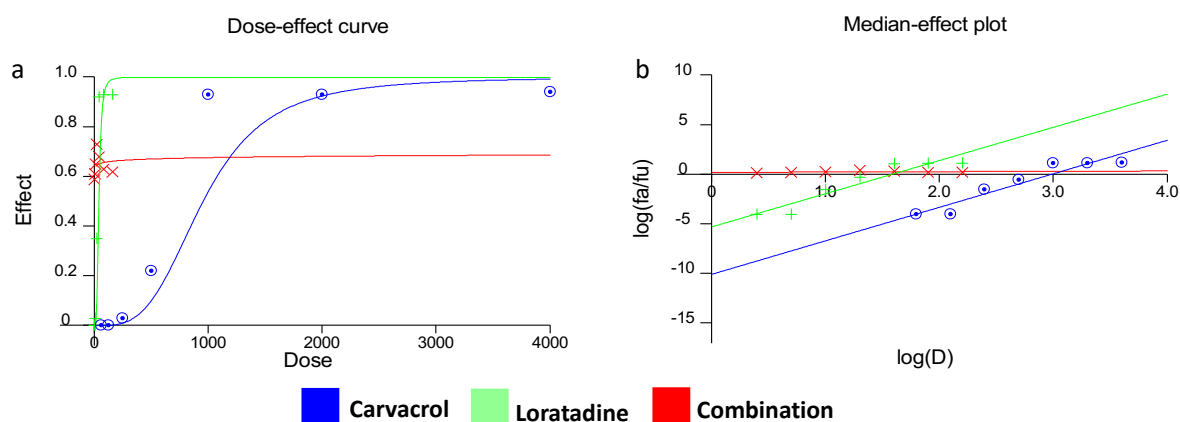


Figure 30. (a) Dose-effect curve analysis and (b) median-effect plot analysis for assessing the drug combination effect. These have been obtained using the CalcuSyn software.

Due to this more work was required looking at different combination concentrations than those mentioned in the “Experimental Methodology” for carvacrol and loratadine. Further analysis of drug combination effects, where the drug concentration of carvacrol remained constant (500 mM) and loratadine changed (3.125 μ M, 6.25 μ M, 12.5 μ M, 25 μ M, 50 μ M, 100 μ M and 200 μ M) was therefore done. The CI is reported in Table 6. From the combination of both drugs, it can be reported that for the ED₅₀ and ED₇₅ levels of inhibition the CI values consistently remain less than 0.8. This therefore indicates a strong level of synergy occurring between the drugs while a moderate synergy/slight additive response is seen at the ED₉₀ level of inhibition achieving a CI value of 0.82. This response overall is better than that which was produced previously in Table 5.

Table 6. CalcuSyn output for the combination of carvacrol and loratadine.

	ED ₅₀	ED ₇₅	ED ₉₀	Dm	m	r
	CI values at					
Carvacrol	N/A	N/A	N/A	952.59056	3.37704	0.94685
Loratadine	N/A	N/A	N/A	37.79736	3.34412	0.94140
Combination	0.37831	0.55927	0.82680	13.75330	1.52728	0.91883

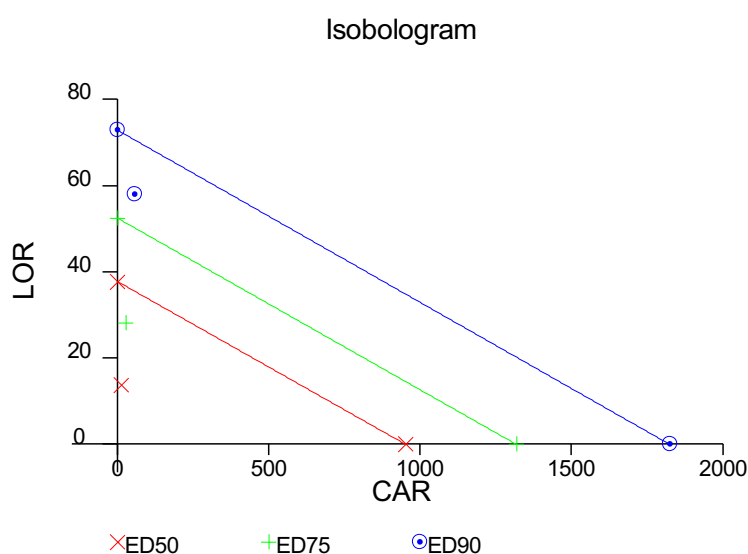


Figure 31. Isobologram plot for assessing the drug combination effect between carvacrol (CAR) and loratadine (LOR). This has been obtained using the CalcuSyn software.

Moreover, the isobologram plot as presented in Figure 31, is another form of analysis produced by the CalcuSyn software which can be used to indicate synergy or antagonistic effect between drug combinations. This isobologram plot is the output achieved from the further analysis concentrations of both drug combinations. Bijnsdorp et al. (2011) have stated that for the isobologram plot, when the data points are found to the left side of the line this indicates synergy while data points to the right side indicate an antagonistic effect between the combined drugs. Hence, as for our isobologram plot, the data points remain to the left side of each level of inhibition indicating overall synergy for this combination where carvacrol concentration remains the same and loratadine concentration changes.

6.2 Computational Results & Discussion

6.2.1 Membrane model system visualisation

An overall modelled lipid membrane system, in this research project, as shown in Figure 32a for the cancer membrane with 16 carvacrol molecules, will consist of a water phase (red lines) above and below the lipid bilayer. The colours royal blue, grey and bright green each are associated with the different lipid types in the mixed membranes, while carvacrol is represented by the magenta purple. Also, the blue, brown, and red large balls are used to represent the atoms nitrogen (N), phosphorus (P) and oxygen (O) which are present in the lipid head groups. Furthermore, the X-Y-Z planes of the cancer membrane model with the addition of 16 carvacrol molecules can be found in Figure 32b, acting as a representative for all systems.

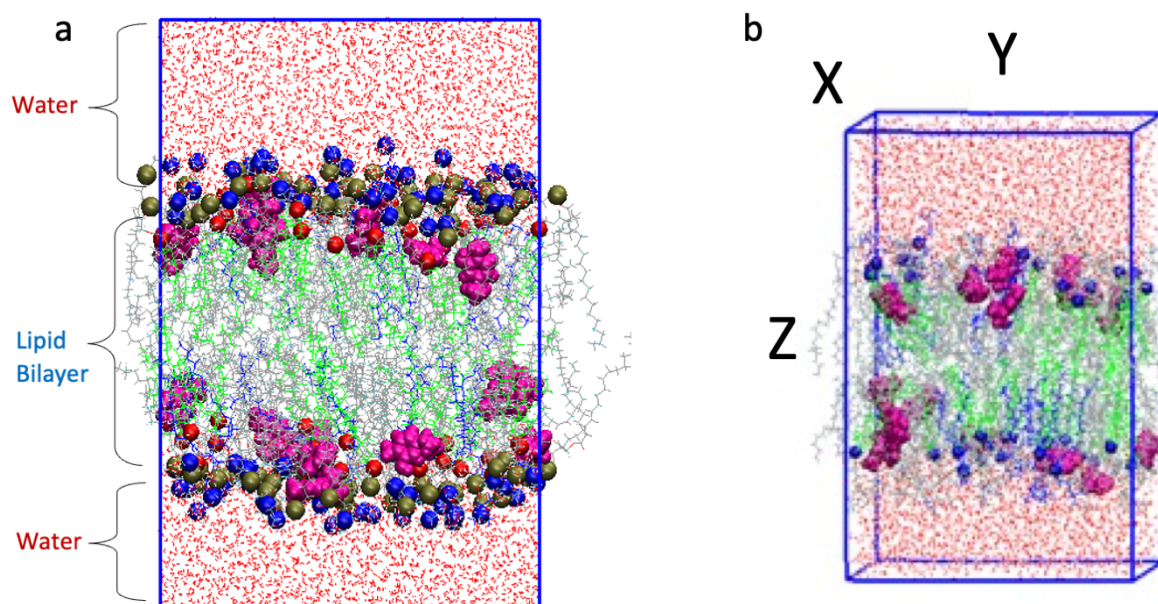


Figure 32. (a) Cancer (flexible) membrane with the addition of 16 carvacrol molecules (magenta purple molecules), the water phase is found as red lines above and below the lipid bilayer. In each membrane system the POPC lipids are shown by grey lines, PSM – by royal blue lines and cholesterol – by the bright green lines. The blue, brown, and red large balls represent nitrogen (N), phosphorus (P) and oxygen (O) from the lipid head groups. (b) The different X-Y-Z planes of a modelled system are shown. These images were obtained using the VMD software package.

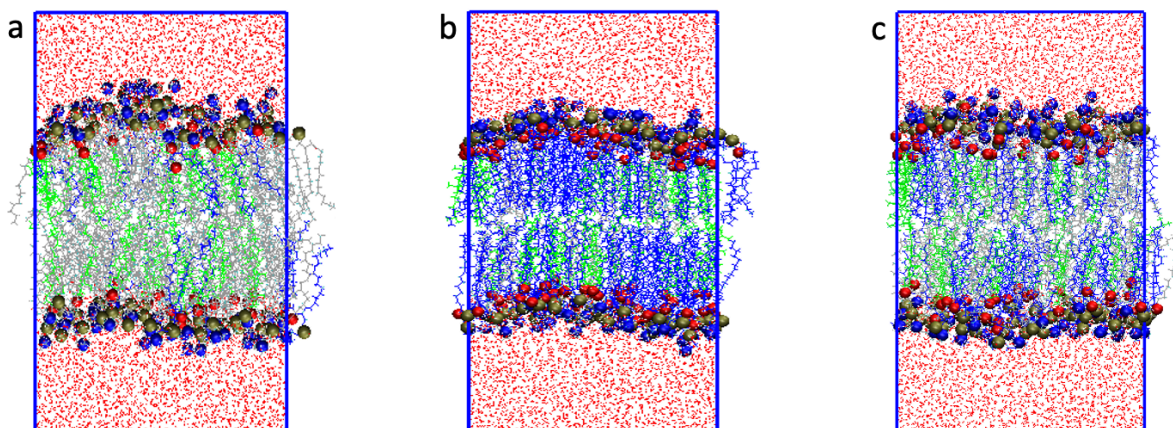


Figure 33. Snapshots of the fully simulated (a) flexible cancer, (b) rigid healthy and (c) intermediate healthy membrane bilayer systems before the addition of any drugs. These fully equilibrated systems were configured after 200 ns of MD production run. The images were obtained using the VMD software package.

The pure mixed membrane systems were all simulated for a total of 200 ns in order to fully equilibrate their bilayers. The final snapshots of each of these membrane systems is presented in Figure 33. The difference in lipid composition for each system is made very apparent as the higher number of POPC in the cancer membrane is represented by the overshadowing bright green lines than in comparison to the healthy rigid membrane where PSM (blue lines) dominates. On the other hand, a balance in colour is found in the healthy intermediate membrane for both POPC and PSM as the lipid composition for these was equal in this system hence “a transition/intermediate membrane”.

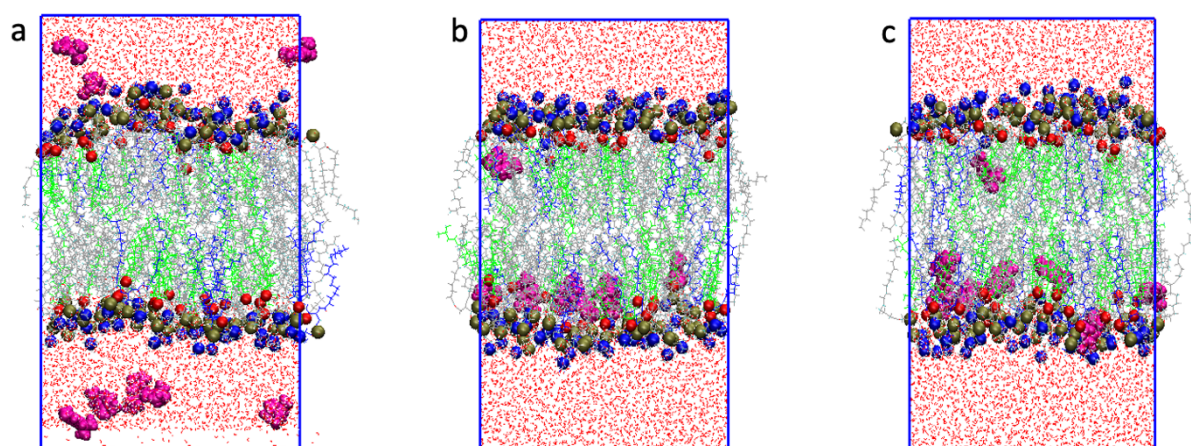


Figure 34. Snapshots of the fully simulated flexible cancer bilayer with the addition of 8 carvacrol (magenta purple) molecules are shown with; (a) presenting the initial configuration with carvacrol molecules randomly placed in the water phase; (b) showing the configuration

after 100 ns of MD production run; and with (c) showing the configuration after 200 ns of MD production run. These images were obtained using the VMD software package.

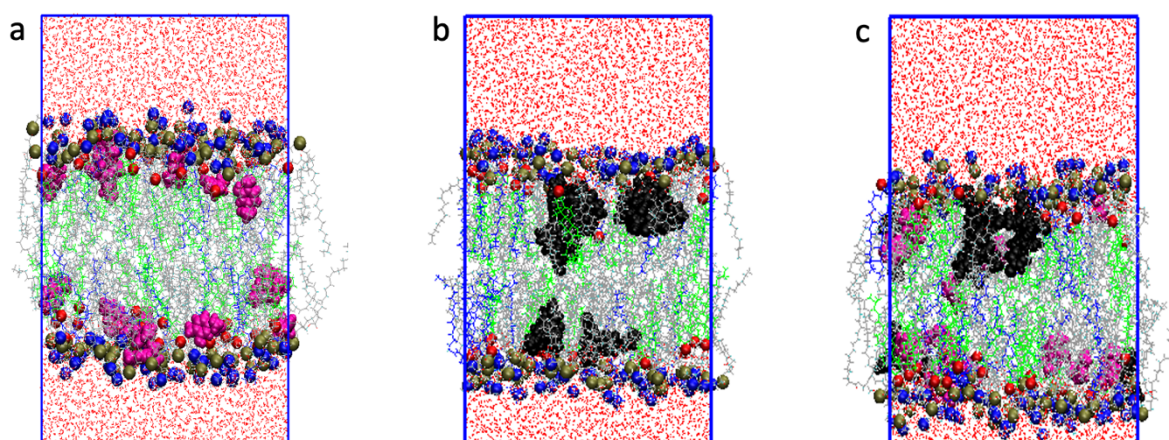


Figure 35. Snapshots of the fully simulated flexible cancer bilayer with the addition of carvacrol (magenta purple) molecules and loratadine (black) molecules are shown with; (a) The configuration with 16 carvacrol molecules after 200 ns of MD production run; (b) shows the configuration after 350 ns of MD production run for the addition of 8 loratadine molecules to the bilayer; and (c) presents the configuration after 350 ns of MD production run, for the combination of 16 carvacrol molecules with 8 loratadine molecules added in this membrane. These images were obtained using the VMD software package.

In general Figure 34 shows the way in which 8 carvacrol molecules behave in the flexible cancer membrane. Initially all of the drug molecules whether carvacrol or loratadine, are seen to just sit anywhere in the water phase above and below the bilayer as shown in Figure 34a for the cancer membrane but this is also the case for both healthy membrane systems. When the blocks of 50 ns simulations begin in the system the carvacrol molecules are able to move around inside and outside of the membrane. In Figure 34b and Figure 34c after 100 ns and 200 ns of MD simulations all 8 of the carvacrol molecules have fully penetrated the cancer lipid membrane and are mainly located sitting near the head groups of the lipids while a couple can be seen closer to the middle or centre of the lipid bilayer. Similar results were also achieved for the cancer membrane with the addition of 16 carvacrol and 8 loratadine molecules individually as well as in combination as shown across Figure 35. All of the drug molecules for carvacrol and loratadine penetrated the cancer bilayer, though for combination this took a longer simulation time of 350 ns.

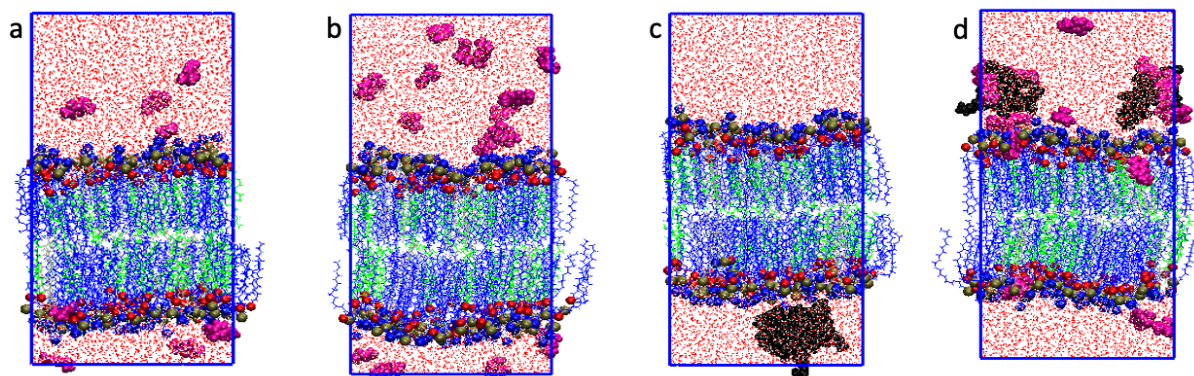


Figure 36. Snapshots of the fully simulated healthy rigid bilayer after the addition of carvacrol (magenta purple) and loratadine (black) molecules. (a) The configuration with 8 carvacrol molecules after 200 ns of MD production run; (b) shows the configuration after 200 ns of MD production run for the addition of 16 carvacrol molecules to the bilayer; (c) the configuration of the membrane with the addition of 8 loratadine molecules after 200 ns of MD production run, and (d) presents the configuration after 350 ns of MD production run, for the combination of 16 carvacrol molecules with 8 loratadine molecules added in this membrane. These images were obtained using the VMD software package.

In the case of the rigid healthy membrane system neither of the drugs carvacrol (8 or 16 molecules) nor loratadine (8 molecules) individually were able to penetrate the bilayer. In Figure 36a and Figure 36b the carvacrol molecules even after being simulated for 200 ns still remain randomly placed in the water phase above and below the bilayer. The black loratadine molecules can be seen to actually cluster together after being simulated for 200 ns outside of the lipid membrane system in Figure 36c. While the carvacrol molecules individually were not able to penetrate the membrane, with the combination, one or two molecules were able to get into the membrane bilayer consistently between 200 to 350 ns, though these molecules also remain near the lipid head groups, a trend also seen in the cancer membrane. Even with the combination the loratadine molecules remain steadfast and do not bypass into the rigid healthy membrane as seen in Figure 36d.

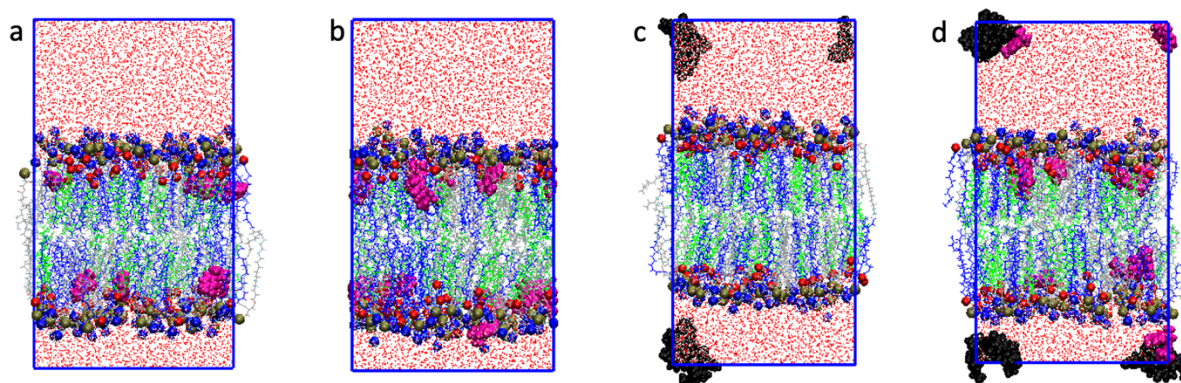


Figure 37. Snapshots of the fully simulated healthy intermediate bilayer after the addition of carvacrol (magenta purple) and loratadine (black) molecules. (a) The configuration with 8 carvacrol molecules after 200 ns of MD production run; (b) shows the configuration of the membrane after 400 ns of MD production run for the addition of 16 carvacrol molecules to the bilayer; (c) the configuration of the membrane with the addition of 8 loratadine molecules after 200 ns of MD production run, and (d) presents the configuration after 350 ns of MD production run, for the combination of 16 carvacrol molecules with 8 loratadine molecules added in this membrane. These images were obtained using the VMD software package.

In the healthy intermediate membrane, carvacrol with the addition of 8 and 16 molecules can penetrate the bilayer as presented in Figure 37a and Figure 37b and also remains near the lipid head groups, a trend across all mixed membrane systems. From Figure 37c it can be noted that loratadine however, does not penetrate this bilayer thus this drug does not cross the lipid bilayer for both healthy membrane systems and remains in the water phase throughout. Figure 37d represents the membrane when both drugs are added in combination here it can be seen that while most carvacrol molecules do pass into the lipid bilayer a few remain in the water phase alongside the loratadine molecules even after 350 ns MD simulation time.

While very little work within our research group has been done on these specific mix lipid membrane models, research from Ahmed Irfan (2020) who looked at cancer and healthy membrane models of the same composition has achieved similar findings. The author found that the cancer membrane allowed permeation of both limonene and carvacrol terpene molecules which were studied. The limonene molecules were found in the midplane while the carvacrol molecules stayed near the lipid headgroups. Limonene only contains

hydrocarbon atoms in its structure overall with no polar groups allowing it to get into the midplane of the cancer membrane. The OH group found in the structure of carvacrol allows it to stay near the lipid head groups instead of completely moving into the midplane. No limonene molecules permeated the healthy rigid membrane though there was some limited permeation for carvacrol, and those molecules stayed near the lipid head groups.

Literature data for skin lipids has shown the permeation of menthol molecules in the ceramide membrane (Wang & Meng, 2017). By increasing the concentration to 16, 32 and 64, the author found that the ceramide membrane each time allowed the permeation of all menthol molecules. This is in line with what was achieved in our data set as increasing the concentration of carvacrol from 8 to 16 molecules in each membrane system individually, the same results were found whether the molecules permeated the membrane or not.

6.2.2 Area per lipid (APL)

One of the first analysis which was done on all the membrane systems was calculating the average APL. The phrase, average area per lipid, ultimately is a measure of the total average membrane bilayer area which is found in the X-Y plane, over the number of lipids that are found in a single leaflet, which in this case was 64 lipids (Akinshina et al., 2016; Saeedimazine et al., 2019). Moradi et al. (2019) have explained the average APL as the initial analysis point as a means of checking the force fields and parameters of the systems allowing adjustments to be made if required. Factors which can affect and cause a fluctuation in the APL value obtained includes the membrane composition, pressure, and temperature in addition to the overall hydration and pH levels of the membrane (Martinez-Seara et al., 2010). APL is usually expressed in the form of an equation as shown below in Equation 8.

$$APL(t) = \frac{A_{XY}(t)}{64} \quad (8)$$

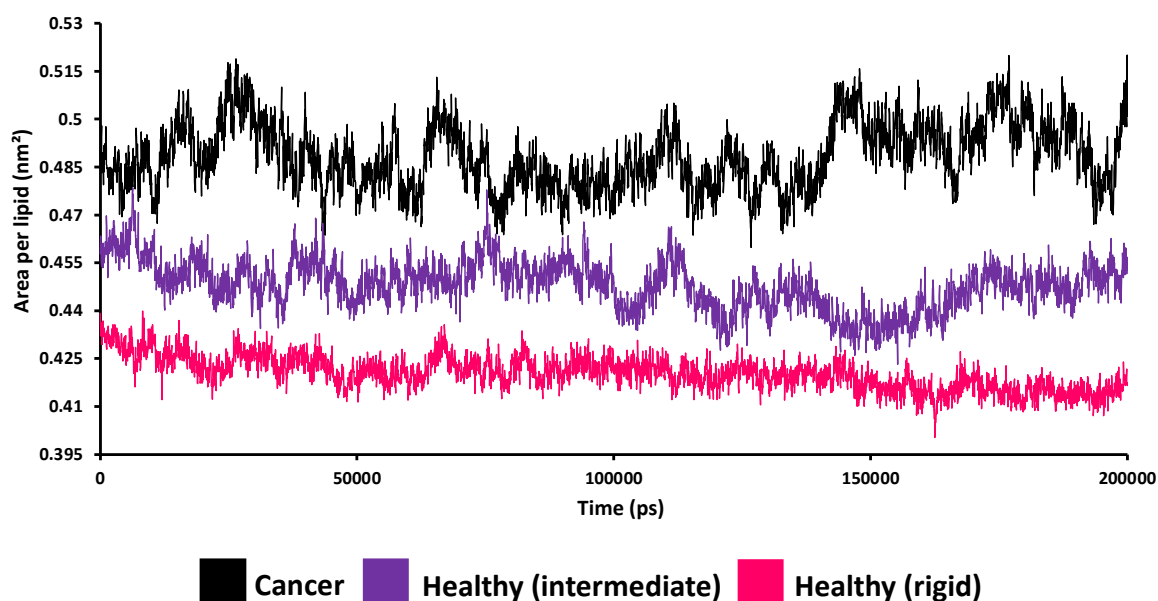


Figure 38. Area per lipid achieved for the mixed membrane systems without the addition of drugs. The black line represents the cancer membrane, purple line represents the healthy intermediate membrane, and the pink line represents the healthy rigid membrane. Each 50,000 ps (50 ns) simulation represents a single MD simulation block.

Figure 38 represents the APL of all the membrane systems before any drugs were added to them. The black lines represent the cancer membrane, purple represents the healthy intermediate membrane, and the pink line represents the healthy rigid membrane. Results achieved from APL can be interpreted as the lower the APL value the tighter the lipid packing is of the membrane system. Here it can be seen that the membrane system with the highest APL was achieved by the cancer membrane which had an APL value of $0.487 \pm 0.005 \text{ nm}^2$, hence making it the membrane with the least densely packed membrane. Both healthy membrane systems achieved relatively similar APL value results with a difference of only 0.027 nm^2 . Between the healthy membranes, the intermediate membrane had the higher APL value at $0.446 \pm 0.004 \text{ nm}^2$, while the rigid membrane achieved the lowest APL value of all the membrane systems at $0.419 \pm 0.003 \text{ nm}^2$.

The results achieved are in line to what is currently seen across previous literature data. Pure CHOL bilayer systems habitually obtain the lowest APL thus the tightest lipid packing, while on the other hand POPC bilayer systems are considered the least tightly packed bilayer as these achieve the highest APL values (Kučerka et al., 2011; Shinoda, 2016). In addition to this,

experimentally pure PSM membranes have also achieved the lower APL values of 0.47 nm^2 in accordance with the work by Maulik and Shipley (1996) while Li et al. (2000) has also experimentally achieved an APL value of 0.52 nm^2 . Additionally, in our research group besides Ahmed Irfan (2020), Hopton (2019) also looked at cancer and healthy membrane models of the similar composition obtaining similar findings. Both authors were able to look at single lipid membrane systems such as POPC, PSM and CHOL in addition to the mixed membrane systems. Results for APL from Hopton (2019) and Ahmed Irfan (2020) are shown below in Figure 39a and Figure 39b, respectively. CHOL had the lowest APL hence the tightest lipid packing across both APL. This was due to its overall planar structure which results in the membrane bilayer having a more rigid liquid-ordered form. On the other hand, POPC achieved the higher APL value consequently resulting in the least tightly packed membrane system. As mentioned previously in the “Cell membranes” section, this results from the *cis*-double bond found in the tails of unsaturated lipids like POPC which leads to a disordered structure preventing tight packing of lipids and consequently leading to higher fluidity in the membrane (Kučerka et al., 2011; Szlasa et al., 2020; Zalba & ten Hagen, 2017). PSM was in the middle so achieved a higher APL than CHOL but lower than POPC. This is because PSM, a saturated phospholipid, contains very straight hydrophobic tails interacting with others via van der Waals interaction (Zalba & ten Hagen, 2017). This therefore means that saturated phospholipids like PSM have a greater preference for a much more ordered and relatively tight packed membrane which has been reflected in the results. As a result of this, amongst the cancer and healthy membrane models, the difference lies within their lipid membrane composition of POPC, PSM and CHOL molecules across all membrane systems, which affects the APL value achieved. Full details of the membrane compositions can be found in the “Computational Methodology” section. POPC levels were higher occupying 65% of the total membrane composition in the cancer membrane. In the healthy rigid and healthy intermediate membrane systems, PSM and CHOL combined amassed the larger total membrane compositions. Therefore, it can be suggested that the POPC lipids are responsible for this disorder and membrane fluidity and PSM as well as CHOL added rigidity and order to membrane systems as has been reflected across the VMD images in the “Membrane model system visualisation” section.

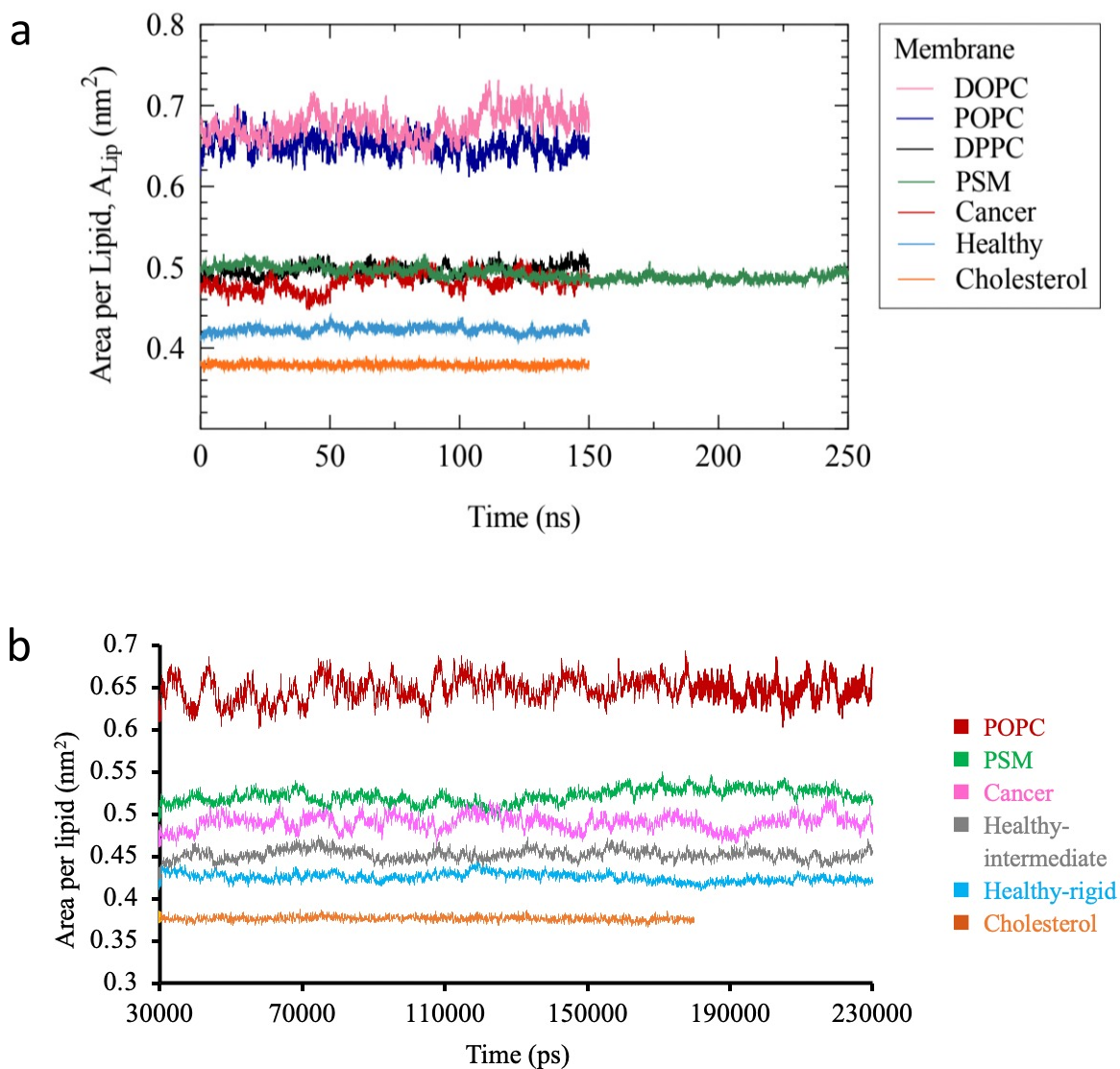
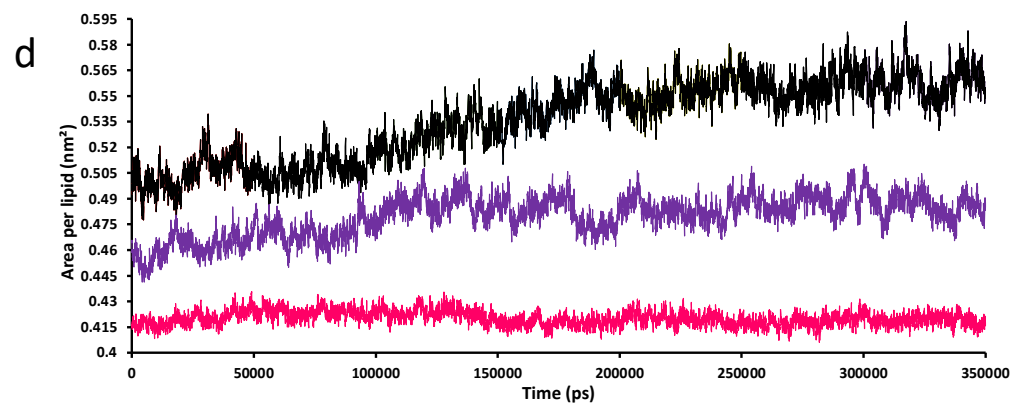
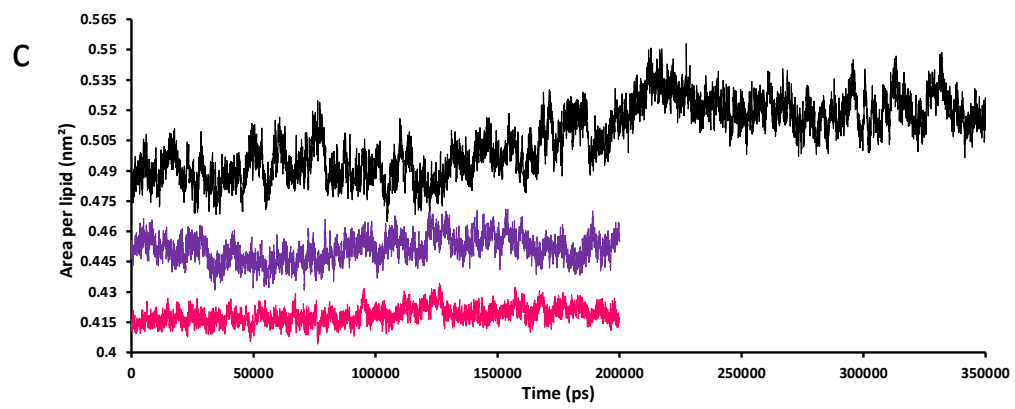
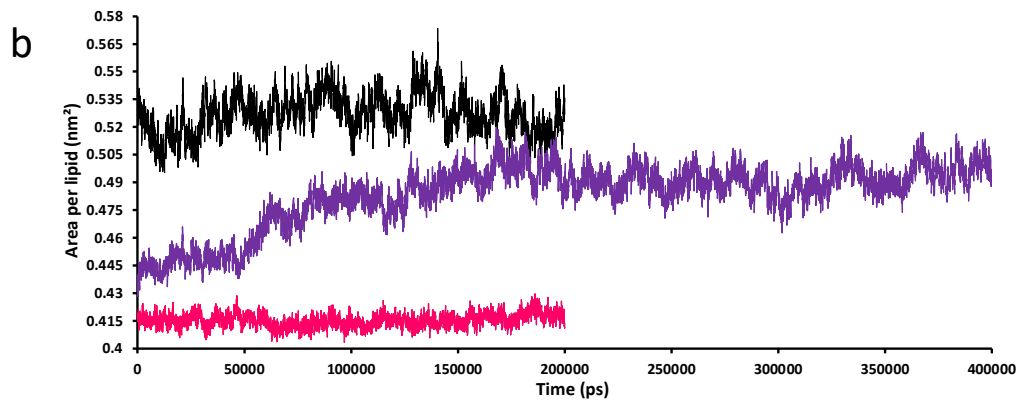
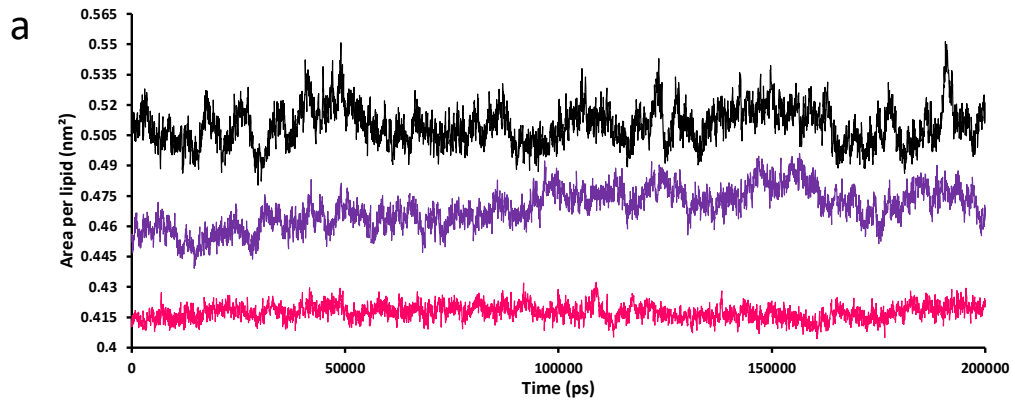


Figure 39. (a) Area per lipid results of single lipid membrane systems (DOPC, POPC, DPPC, PSM and Cholesterol) as well as mixed lipid membrane systems representing a cancer and healthy model membrane (Hopton, 2019). (b) Area per lipid of mono-lipid membranes (POPC, PSM and Cholesterol) and mixed lipid membrane systems (Cancer, Healthy – intermediate and Healthy – rigid) (Ahmed Irfan, 2020).



Cancer
 Healthy (intermediate)
 Healthy (rigid)

Figure 40. Area per lipid of each membrane system after the addition of carvacrol, loratadine. (a) Cancer, healthy rigid and healthy intermediate membrane systems with the addition of 8 carvacrol molecules. (b) Cancer, healthy rigid and healthy intermediate membrane systems with the addition of 16 carvacrol molecules. (c) Cancer, healthy rigid and healthy intermediate membrane systems with the addition of 8 loratadine molecules. (d) Cancer, healthy rigid and healthy intermediate membrane systems with the addition of 16 carvacrol and 8 loratadine molecules in combination. Each 50,000 ps (50 ns) simulation represents a single MD simulation block.

Figure 40a and Figure 40b present each membrane system with the addition of 8 and 16 carvacrol molecules. While the cancer membrane already had the highest APL before the addition of drugs, APL further increases when carvacrol and loratadine molecules are added to the membrane. With the addition of 8 and 16 carvacrol molecules the APL rose to $0.509 \pm 0.002 \text{ nm}^2$ and $0.528 \pm 0.004 \text{ nm}^2$, respectively from $0.487 \pm 0.005 \text{ nm}^2$. From Figure 40c it can be noted that the addition of 8 loratadine molecules also increased the initial APL value to $0.521 \pm 0.003 \text{ nm}^2$. The combination of both drugs in this membrane saw the highest increase overall in APL across all systems as this increased to a value of $0.555 \pm 0.005 \text{ nm}^2$ as seen in Figure 40d.

Unsurprisingly, the lowest APL was obtained by the healthy rigid membrane as the value achieved for APL before and after the addition of carvacrol and loratadine molecules showed no significant change. In the case of 8 carvacrol molecules the APL value was $0.417 \pm 0.001 \text{ nm}^2$ and with 16 carvacrol molecules the APL value only dropped slightly to $0.415 \pm 0.001 \text{ nm}^2$ from the initial $0.419 \pm 0.003 \text{ nm}^2$. For both the addition of loratadine and combination the APL remained unchanged. This can therefore suggest that the lipid packing of this healthy rigid membrane remained tightly packed upon the addition of drugs to its membrane.

The middle range was achieved by the healthy intermediate membrane system which did see a small increase in its APL value when carvacrol and loratadine molecules were added. Both 8 and 16 carvacrol molecules increased the APL value, from $0.446 \pm 0.004 \text{ nm}^2$ to $0.472 \pm 0.005 \text{ nm}^2$ and $0.490 \pm 0.001 \text{ nm}^2$ respectively, hence making the lipid packing somewhat less rigid of the healthy intermediate membrane system allowing the carvacrol molecules to

penetrate. This is also portrayed in the VMD images in Figure 37a and Figure 37b as the carvacrol molecules can be seen inside the bilayer near the lipid head groups. With the addition of 8 loratadine molecules only a slight increase was seen in APL as a value of $0.451 \pm 0.003 \text{ nm}^2$ was achieved. The lipid bilayer remained packed and ordered as it was before the addition of loratadine and from the VMD image in Figure 37c it also shows that loratadine does not permeate the healthy intermediate membrane. With regards to the drug combination the APL does increase by 0.040 nm^2 to $0.486 \pm 0.002 \text{ nm}^2$. This increase could result from the presence of the carvacrol molecules as although not all, some of the molecules are able to penetrate membrane as shown in Figure 37d from the VMD image.

An increase in the APL achieved through the addition of drugs to a membrane system has also been reported in literature. Witzke et al. (2010) found an increase in the APL value when the terpenes limonene, perillyl alcohol, perillaldehyde and deprotonated perillic acid (DPAC) were added to the DMPC and POPC lipid membranes. The authors noted that the largest increase was accomplished through the addition of DPAC as an 11% increase in APL was achieved overall in the membranes. On the other hand, Wang and Meng (2017) found that in two membrane systems, a pure ceramide membrane or a mixed membrane system consisting of ceramide, free fatty acid and CHOL, upon the addition of increased concentrations of menthol the APL decreases overall. The APL graph which Wang and Meng (2017) achieved for the pure ceramide membrane system is found in Figure 41. While 16 molecules of menthol do not shift the ceramide APL from 0.42 nm^2 achieved for its pure system, this value decreases to 0.41 nm^2 (green line) and 0.40 nm^2 (purple line) for 32 and 64 menthol molecules as seen in Figure 41. In the mixed systems between no menthol and 50 molecules of menthol no significant change is seen in APL while the addition of 100 molecules of menthol led to a decrease from the initial 0.83 nm^2 to 0.63 nm^2 .

Overall, as the increase and decrease in APL before and after addition of the drugs was kept minimal in the membrane systems, this can suggest that drug permeation does not actually disrupt their lipid packing. Generally, each of the membranes were able to uphold their initial structure and shape when drugs were added.

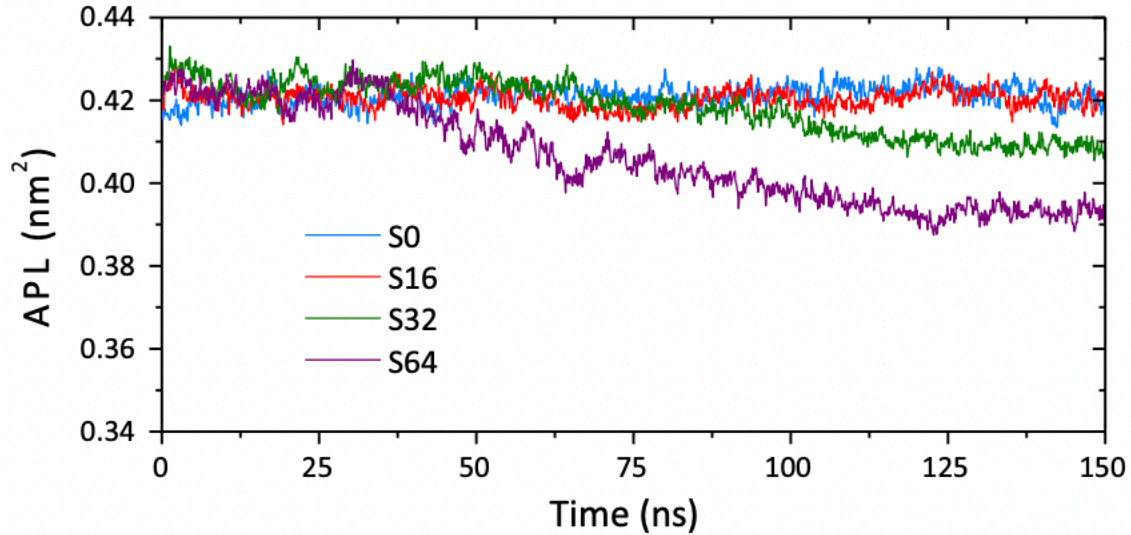


Figure 41. Area per lipid of the ceramide with and without the addition of increasing concentrations of menthol molecules. S0 represents the pure ceramide membrane (blue line), S16 represents the ceramide membrane with 16 menthol molecules (red line), S32 is for the ceramide membrane with 32 menthol molecules (green line) and S64 shows the ceramide membrane with 64 menthol molecules (Wang & Meng, 2017).

6.2.3 Area compressibility modulus

An increase in the membrane flexibility can lead to an increase in the membrane permeability therefore allowing more molecules to pass into the lipid bilayer (Lande et al., 1995). The lipid packing analysis achieved from APL is found to be directly correlated to the membrane flexibility as having more space for movement will ensure better fluidity of the lipids within the membrane. As a result, the next area for analysis, to distinguish how the cancer and healthy membrane systems react to the drugs was area compressibility modulus κ_A . This refers to the amount of energy which is needed per unit surface area in order to stretch the membrane bilayer (Akinshina et al., 2016). Essentially κ_A is a measure of the membrane rigidity, and its calculations are based on the area fluctuations of the membrane bilayer represented as the Equation 9 presented below.

$$\kappa_A = k_B T \frac{\langle A \rangle}{\langle A^2 \rangle - \langle A \rangle^2} \quad (9)$$

Whereby, k_B represents the Boltzmann constant, T is the temperature and the $\langle A \rangle$ signifies the average membrane bilayer area from the X-Y plane (Akinshina et al., 2016; Doktorova et

al., 2019; Moradi et al., 2019; Venable et al., 2015). With the compressibility modulus, the higher the value achieved for κ_A , the more rigid the membrane system is. All results for the average compressibility modulus for each system are found in Figure 42 and Table 7. For the mixed lipid membrane models before the addition of drugs, the cancer membrane attained the lowest κ_A value, 233 ± 36 dyne/cm which in-line with its APL results means this membrane is highly flexible. Research has found that in cancers such as lymphomas and lung cancer, membrane fluidity is a great deal higher and membrane rigidity is lower compared to healthy counterparts (Alves et al., 2016; Sherbet, 1989). Sok et al. (2002) have proposed that the changes which are observed in the cancer cell membrane in terms of increased fluidity and decreased membrane rigidity is related to the ability of these cancer cells to metastasize/form metastases. The healthy (rigid) membrane attained the highest κ_A value at 1415 ± 339 dyne/cm suggesting out of all the membrane systems this was the one which had the highest rigidity thus lowest flexibility. The healthy (intermediate) membrane which achieved a κ_A value at 461 ± 164 dyne/cm was much more flexible compared to the healthy (rigid) membrane but not as much as the cancer membrane.

These results for the κ_A values which have been achieved are fairly expected, rising from the lipid membrane construction of each mixed system. The healthy rigid membrane would be anticipated to achieve the highest κ_A value as its lipid composition consists of a larger number of lipids which are responsible for rigidity, PSM and CHOL. Similarly, for the flexible cancer membrane which contains a majority of POPC lipids in its composition the κ_A value achieved would be expected to be lower.

Very little change in the compressibility modulus can be seen with the addition of both carvacrol and loratadine to the cancer membrane overall. It remained with the lowest κ_A value throughout meaning its disordered fluidic state allowed it to be very flexible and permeable to the entry of the drugs even in combination. With the addition of 8 carvacrol molecules, 8 loratadine molecules and the combination (16 CARV + 8 LOR) the cancer membrane did see a slight increase in the overall κ_A value with each being 273 ± 80 dyne/cm, 291 ± 37 dyne/cm and 263 ± 24 dyne/cm which could suggest a slight increase in its membrane rigidity. The results for 8 carvacrol molecules was not significant achieving a p value of greater than 0.05 while for 8 loratadine and the combination the results were

significant with a p value of less than 0.05. A decrease in κ_A from the addition of 16 carvacrol molecules at 225 ± 39 dyne/cm was seen which could suggest that with this addition the cancer membrane became less rigid and more flexible and permeable. The p value obtained in this instance was less than 0.05 so the results can be regarded as significant.

Moreover, both healthy membrane systems also saw little to no change in their compressibility modulus after the addition of both drugs. When both loratadine and carvacrol were added to the healthy rigid membrane the κ_A value throughout did somewhat decrease but this was not seen as significant. The compressibility modulus decreased with the average κ_A value reaching 1182 ± 229 dyne/cm in the presence of 8 carvacrol molecules, 1413 ± 255 dyne/cm for 16 carvacrol molecules as well as 1146 ± 104 dyne/cm for 8 loratadine molecules from the original 1415 ± 339 dyne/cm when no drugs were present. In the case of the healthy intermediate membrane both 8 and 16 molecules of carvacrol slightly decreased the compressibility modulus with the κ_A value being 410 ± 99 dyne/cm and 378 ± 99 dyne/cm, correspondingly though this was not significant. On the other hand, 8 loratadine molecules increased the membrane rigidity as the compressibility modulus had a κ_A value being 524 ± 18 dyne/cm.

When the drugs were in combination (16 CARV + 8 LOR) the compressibility modulus for both healthy membrane systems decreased. The healthy (rigid) membrane had a κ_A value of 1266 ± 138 dyne/cm while the healthy (intermediate) membrane was 419 ± 73 dyne/cm. Therefore, even though the healthy (rigid) membrane system is the most rigid membrane overall, with the addition of both drugs individually and in combination, it becomes slightly more flexible and permeable losing a bit of its rigidity.

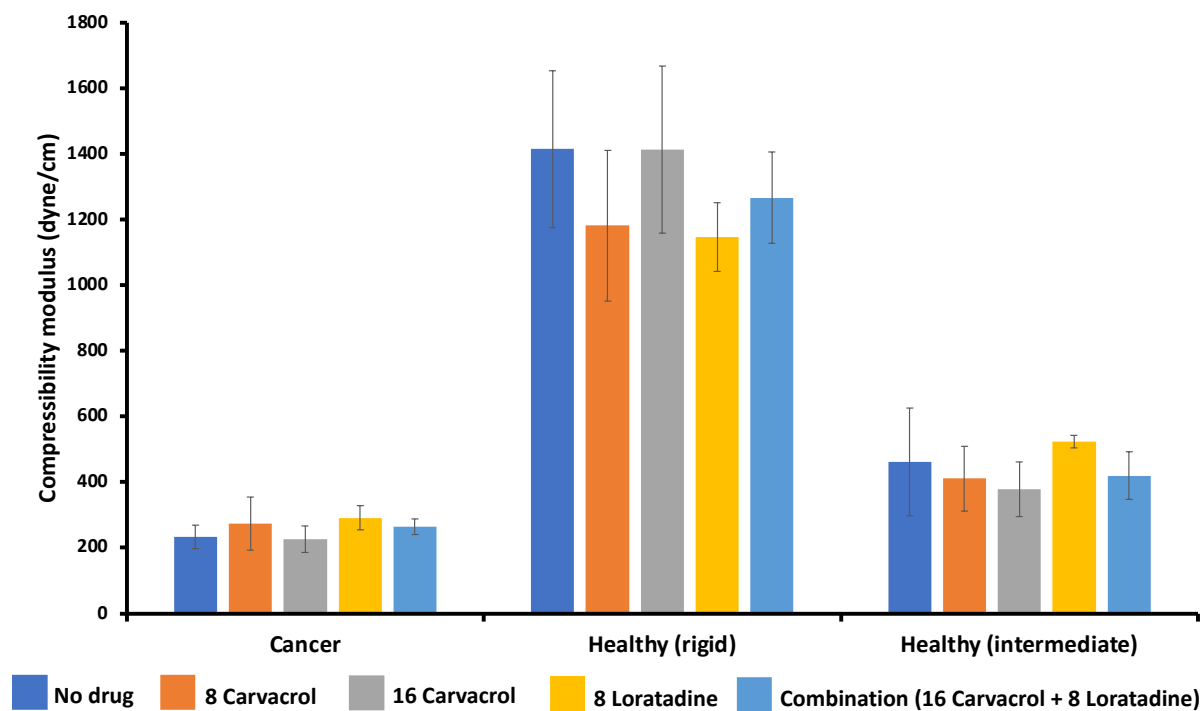


Figure 42. Average compressibility modulus achieved for the cancer, healthy rigid and healthy intermediate membrane systems.

Table 7. Area compressibility modulus of the cancer and healthy membrane models before and after the addition of drugs.

	K_A (dyne/cm)	Cancer K_A (dyne/cm)	Healthy (rigid) K_A (dyne/cm)	Healthy (intermediate) K_A (dyne/cm)
NO DRUG	233 ± 36	1415 ± 239	461 ± 164	
CARVACROL (8)	273 ± 80	1182 ± 229	410 ± 99	
CARVACROL (16)	226 ± 39	1413 ± 255	378 ± 83	
LORATADINE (8)	291 ± 37	1146 ± 104	524 ± 18	
COMBINATION (16 CARV + 8 LOR)	263 ± 24	1266 ± 138	419 ± 73	

6.2.4 Lipid tail order parameters

The lipid tail order parameters are denoted as S_z . These order parameters are used to refer to the overall positioning of the hydrocarbon tails with reference to the z axis which is also referred to as the membrane bilayer normal. Additionally, when the motion of lipids remains the same around the membrane bilayer normal, the deuterium order parameter, S_{CD} , instead can be measured via NMR experiments of lipids as $S_z = -2S_{CD}$ (Akinshina et al., 2016). The equation used to calculate the lipid tail order parameters is presented in Equation 10.

$$S_z = \frac{3}{2} \langle \cos^2 \theta_z \rangle - \frac{1}{2} \quad (10)$$

The components making up Equation 10 are defined as the following. The θ_z refers to the angle found between the membrane bilayer normal i.e., the z axis and the molecular axis. For all of the lipids, the average time for two bonds which are found in each group of CH_2 is represented by the brackets in the equation. Molecular axis for any atom signified as n can potentially be outlined as a vector and can be calculated from the atom C_{n-1} to the atom C_{n+1} . The numbers which can be obtained for the S_z can vary between -0.5 to a value of 1. Vectors which are perpendicular to each other i.e., the alignment of the hydrocarbon tails is perpendicular to the membrane bilayer normal, achieve the smaller S_z value of -0.5. On the other hand, the higher value of 1 is obtained when the alignment of hydrocarbons is parallel with the membrane bilayer normal (Akinshina et al., 2016; Moradi et al., 2019). By utilizing the lipid tail order parameters, analysis of the cancer and healthy membrane systems in terms of fluidity/rigidity can be made and it can be used to describe how the addition of the drugs can ultimately disturb the lipid tail order.

The order/disorder and fluidity/rigidity for lipid tail order parameter analysis is made in reference to tail 1 (sn-1) and tail 2 (sn-2) for both POPC and PSM lipids in each membrane system.

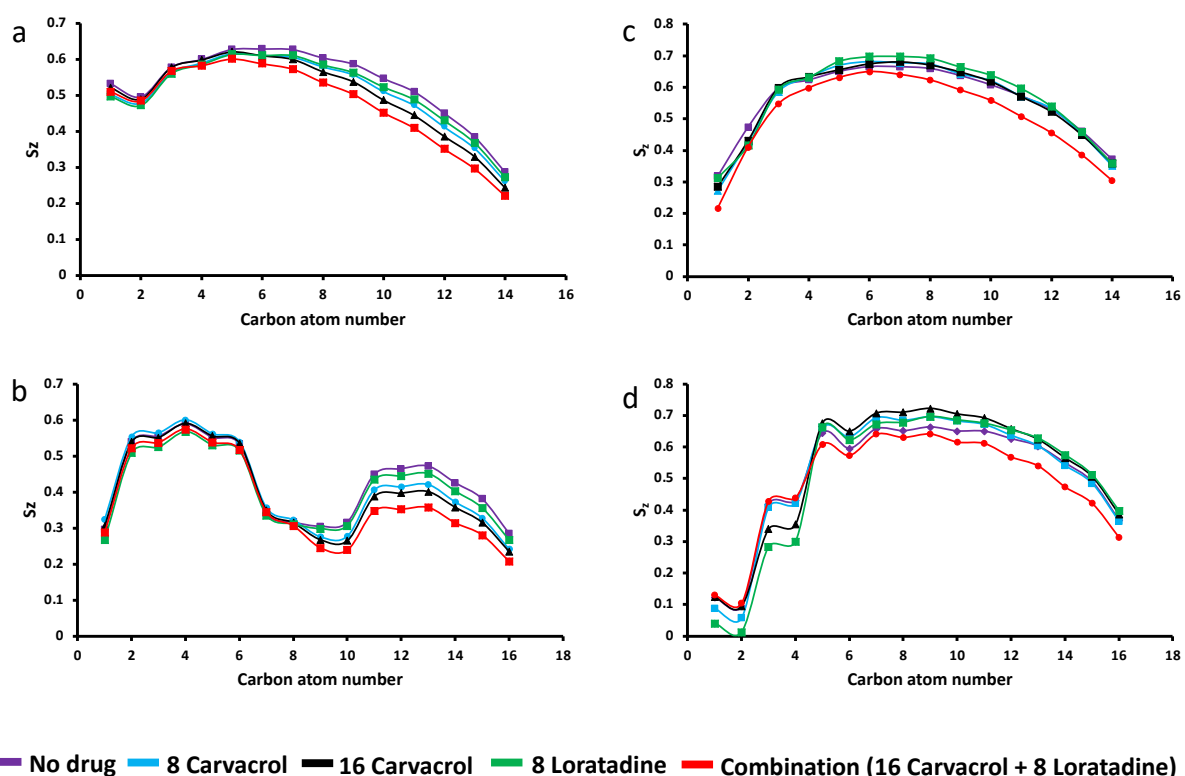
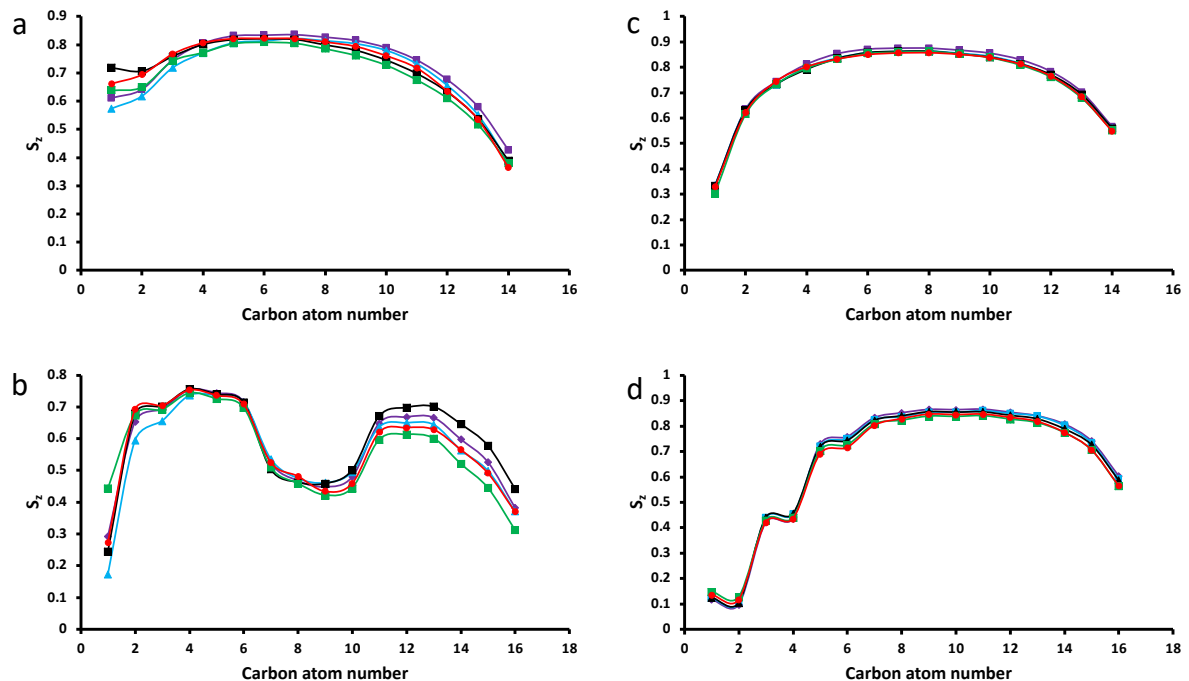


Figure 43. POPC and PSM lipid tail order parameters for the cancer membrane whereby (a) is representing the POPC sn-1 tail and (b) is for the POPC sn-2 tail. (c) Represents the tail order for the PSM sn-1 tail while (d) is representative of PSM sn-2 tail.

Out of all mixed membrane systems, the cancer membrane had the lowest overall lipid tail order parameters for POPC and PSM tail 1 and tail 2 even before the addition of any drugs to its system. In all tail order graphs, the first carbon atom indicates where the lipid head group is while carbon atoms 14 to 16 indicate the midplane of the membrane bilayer. In the case of POPC, the dip seen between the atoms 6 to 10 in Figure 43b was due to the *cis* double bond found in the POPC sn-2 tail. The S_z parameter decreases overall in the cancer membrane with the addition of both drugs, for both tails of POPC and PSM lipids. Furthermore, the order parameters for PSM are always higher than that of POPC as it contains all saturated bonds and has a different structure in terms of its head group. By taking into account the combination of 16 carvacrol molecules with 8 loratadine molecules, across both POPC and PSM in the cancer membrane, there is a decrease in the S_z values that are obtained in comparison to no drugs in this membrane system. When the drugs are combined it is clear to see that the POPC and PSM tails become less ordered than when there are no drugs. The

lowest S_z values attained for POPC sn-1 and sn-2 tails was 0.29 and 0.28 before drugs and this decreased to 0.22 and 0.21 respectively, when the drugs were combined. Whilst the lowest S_z values achieved for PSM sn-1 and sn-2 tails was 0.32 and 0.09 with no drugs and in combination the S_z values were 0.22 and 0.10, respectively. So, this indicates the perpendicular alignment of the lipid tails to the membrane bilayer normal and an overall increase of lipid tail disorder.



— No drug — 8 Carvacrol — 16 Carvacrol — 8 Loratadine — Combination (16 Carvacrol + 8 Loratadine)

Figure 44. POPC and PSM lipid tail order parameters for the healthy rigid membrane whereby (a) is representing the POPC sn-1 tail and (b) is for the POPC sn-2 tail. (c) Represents the tail order for the PSM sn-1 tail while (d) is representative of PSM sn-2 tail.

The highest overall lipid tail order parameters were expectedly achieved by the healthy rigid membrane system. Before and after the addition of drugs to the membrane not much change in terms of S_z is observed across Figure 44 for both POPC and PSM tails. Especially for PSM there is no effect to be reported for both tails. For POPC there is no effect on the saturated sn-1 tail, the small change on the only unsaturated sn-2 tail could just be a result of the fluctuations which occurred from the addition of drugs as this tail is the most flexible. Therefore, it can be understood that this membrane in general remains very rigid with

ordered tails not allowing the permeation of either drug into its membrane bilayer hence concluding the parallel alignment of the lipid tails to the membrane bilayer normal as can be seen in the VMD images across Figure 36.

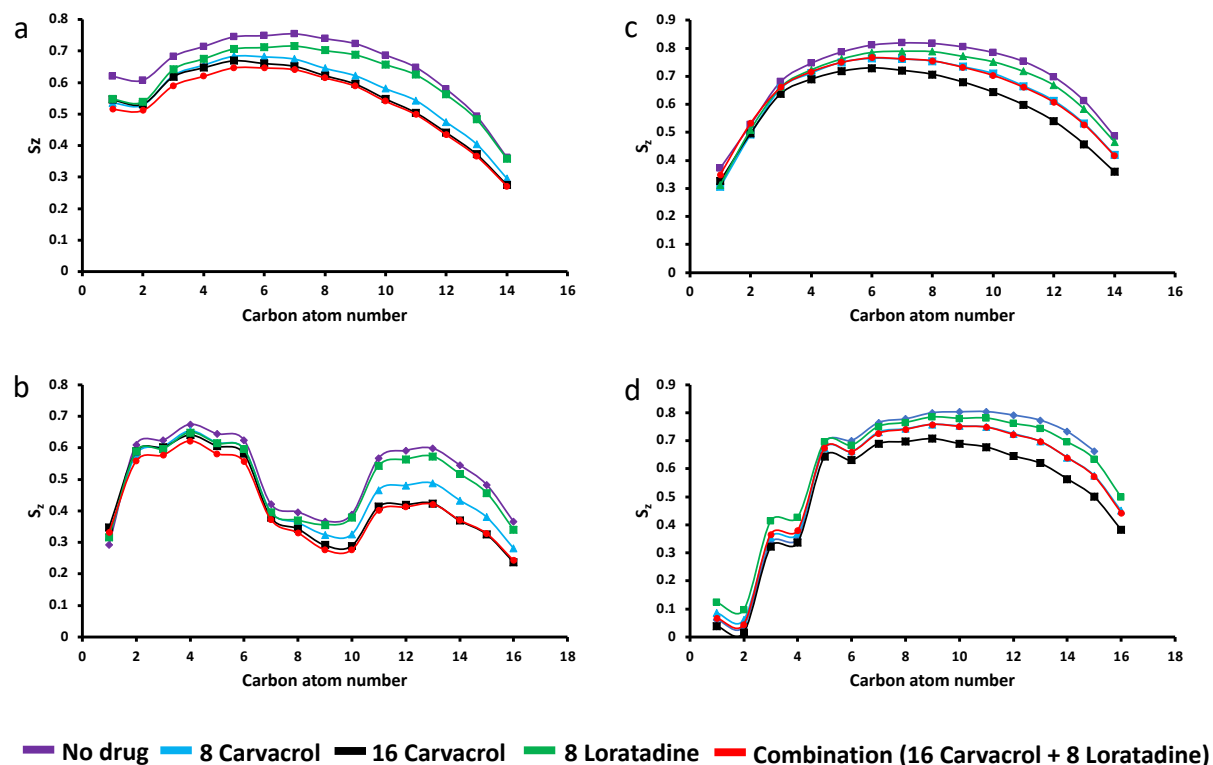


Figure 45. POPC and PSM lipid tail order parameters for the healthy intermediate membrane whereby (a) is representing the POPC sn-1 tail and (b) is for the POPC sn-2 tail. (c) Represents the tail order for the PSM sn-1 tail while (d) is representative of PSM sn-2 tail.

With the healthy intermediate membrane system, straightaway from Figure 45 it can be seen that the addition of drugs generally has led to a decline in the S_z . For the POPC tails the combination of the drugs achieved the lowest S_z value (although there was not much difference when compared to the tail order for 16 carvacrol molecules). Before drugs were added the S_z value for POPC at the last carbon atom was 0.36 (sn-1) and 0.37 (sn-2) and this decreases to 0.27 (sn-1) and 0.24 (sn-2) for the combination. In terms of the PSM tails the greatest decline in the S_z value was obtained for the addition of 16 carvacrol molecules. The S_z values for the PSM tails were 0.49 (sn-1) and 0.53 (sn-2) at the last carbon atom with no drugs. For the 16 carvacrol molecules this S_z value decreased to 0.36 (sn-1) and 0.38 (sn-2) for the PSM tails. It may be interesting how the S_z is not the lowest for the combination of drugs though this could be explained due to the fewer carvacrol molecules which had penetrated

the healthy intermediate membrane when combined with loratadine. Thus, the carvacrol molecules cause a greater disorder to the healthy intermediate membrane allowing it to be more fluid/permeable leading to some perpendicular alignment of the lipid tails to the membrane bilayer normal as also highlighted by the VMD images in Figure 37.

Results on the lipid tail order parameters from Ahmed Irfan (2020) have shown that between mono and mixed lipid, cancer and healthy membrane systems, both POPC and PSM have much more order in their lipid tails in a mixed system compared to pure POPC and PSM membranes. A reason for this is due to the ordering effect which has been associated with CHOL molecules. Literature papers have also reported that the tail order of phospholipid bilayer membranes in particular increases with the presence of CHOL (Hantal et al., 2019; Róg et al., 2009). Moreover, experimental research also provides support for this as it has been found that when CHOL is added to a pure POPC membrane, which is already naturally disordered resulting from the *cis*-double bond causing a kink in its structure, the tail order increases in the membrane overall (Saeedimazine et al., 2019). Furthermore, research into the PSM lipid has found that this too can result in an increase in lipid tail order especially when it is added to a phospholipid bilayer hence resulting in a more ordered system (Bera & Kluda, 2017). Therefore, when higher levels of either PSM or CHOL are found in a mixed lipid membrane, which in this case were the healthy membrane systems, it can be correlated with more order in their tails. On the other hand, the more POPC found in a mixed lipid membrane (cancer membrane system) the more disordered their tails will appear to be, and these results have been reflected in the VMD images.

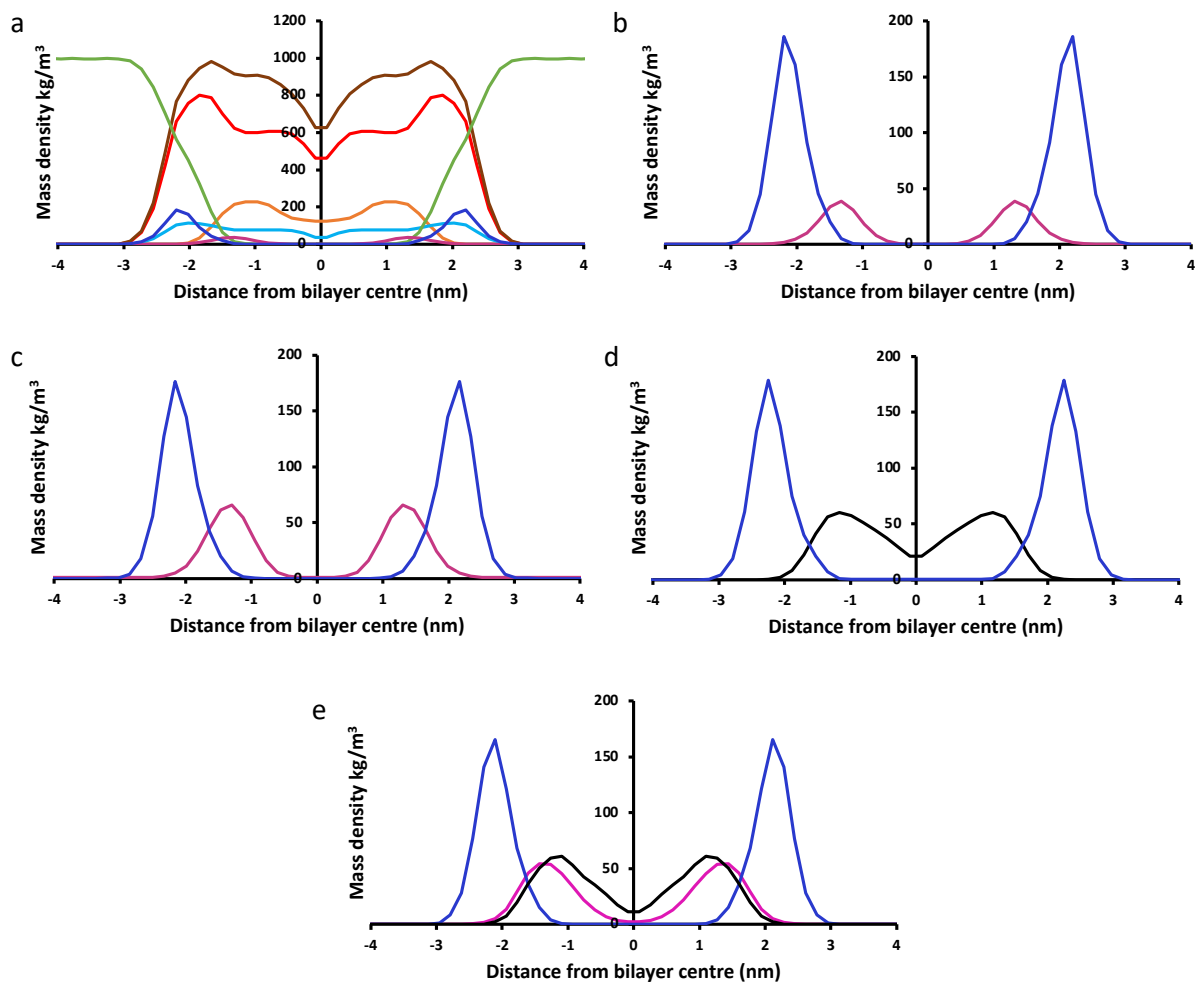
The research from Ahmed Irfan (2020) also looked at the effects of the terpenes, carvacrol and limonene on cancer and healthy membrane systems. Here it was found that when carvacrol was added to the mixed membrane bilayers the S_z achieved for each system would decline much more than with the addition of limonene. Consequently, this led to higher levels of disorder with the lipid tails for their healthy and cancer membrane systems. Reasons for this, as stated previously, is due to the structure of limonene containing all hydrocarbons with no polar groups allowing it to move into the membrane midplane with ease. While carvacrol contains an OH group in its structure allowing it to stay near the lipid head groups. Thus, evidencing what was also achieved in terms of a decline in the lipid tail order parameters for

POPC and PSM for our cancer and both healthy membrane systems with the addition of both carvacrol and loratadine molecules. Furthermore, Alsop et al. (2016) have reported that in a pure POPC membrane when increasing concentrations of cortisone (up to 50 mol%) is added, this leads to a decline in the lipid tail order. This is therefore in agreement of what was achieved in our results. It has also been found that for skin lipids the tail order decreases only when very large amounts of menthol (64 or 100 molecules) are added as the effect was much weaker with lower amounts (Wang & Meng, 2017). But as skin lipids mainly consist of ceramides which in turn are very ordered lipids with small head groups, they can form very well packed membrane systems. Concerning the research from Witzke et al. (2010) the opposite effect has been achieved. In this case the tail order of the lipids increased upon the addition of all the terpenes except for DPAC and this difference could be related to the structures of the lipids and the fact that DPAC is a charged molecule and interacts stronger with the lipid head groups.

6.2.5 Mass density & membrane thickness

The membrane density profiles in general are used to refer to the time average of various properties that can be calculated for the membrane systems, along the Z plane. These properties can include but are not limited to, electron density, the scattering length, occurrence, charge, and mass which was the membrane property focused on for our research project (Martinez-Seara et al., 2010; Moradi et al., 2019). This mass density profile analysis was done by using the *gmx_density* tool from GROMACS for the density of individual components such as the lipids, water, the drugs, and head groups. As mentioned previously N, P and O were chosen to represent the head group region of the lipids. In relation to the centre of the lipid bilayer (0 nm), this analysis tool permitted us to pinpoint the location of the drugs and consequently understand the level of permeability of each cancer and healthy membrane system to carvacrol and loratadine.

From the density profiles the membrane thickness can also be calculated. The membrane thickness refers to the distance between the two peaks found in the mass density profiles for the headgroups of the lipids (Moradi et al., 2019; Saedimazine et al., 2019; Van der Paal et al., 2017). This allows us to see whether the addition of drugs to each mixed membrane system, affected the membrane thickness as a whole.



■ POPC
 ■ PSM
 ■ CHOL
 ■ Head groups of the lipids
 ■ Membrane
 ■ Water
 ■ Carvacrol

Figure 46. Mass density profiles of the cancer membrane after the addition carvacrol and loratadine molecules. (a) The complete mass density profile for the addition of 8 carvacrol molecules consisting of the lipids POPC, PSM and CHOL which are red, light blue and orange lines. The dark blue line represents the head groups of the lipids, the membrane is brown, water is green, and the magenta purple line signifies carvacrol. (b) Same 8 carvacrol molecules mass density profile but this only contains the dark blue line which represents the head groups of the lipids and the magenta purple line to show carvacrol, all other components are omitted. (c) Profile for the addition of 16 carvacrol molecules. (d) Profile for the addition of 8 loratadine molecules. (e) Profile for the combination of 16 carvacrol with 8 loratadine molecules. For profiles (b) to (e) the scale of the graphs was increased for better visibility of the results. All mass density profiles were symmetrised.

The mass density profile for the cancer membrane is presented in Figure 46 after the addition of carvacrol and loratadine molecules. The distance from the midplane of the lipid bilayer is denoted on the x axis, whereby the 0 nm is used to represent the actual centre of the lipid bilayer. The mass density of the various components, so the individual lipids, the membrane, water, head groups of the lipids and carvacrol, are presented on the y axis as presented in Figure 46a. As the graph may not be clear to depict, for clarity purposes besides the head groups of the lipids and the drug, the rest of the components will be omitted as shown in Figure 46b from the mass density profile. Together with the VMD images in Figure 34c and Figure 35, all of the molecules for both drugs penetrate the cancer membrane. From Figure 46d and Figure 46e, the 8 loratadine molecules are found to have a shorter distance to the midplane making them closer to centre of the bilayer compared to the carvacrol molecules which are closer to the head groups of the lipids. The density of loratadine at the centre is not 0 nm which means that some molecules have permeated inside the bilayer and have either reached or crossed the midplane, an effect not observed for the carvacrol molecules in this membrane.

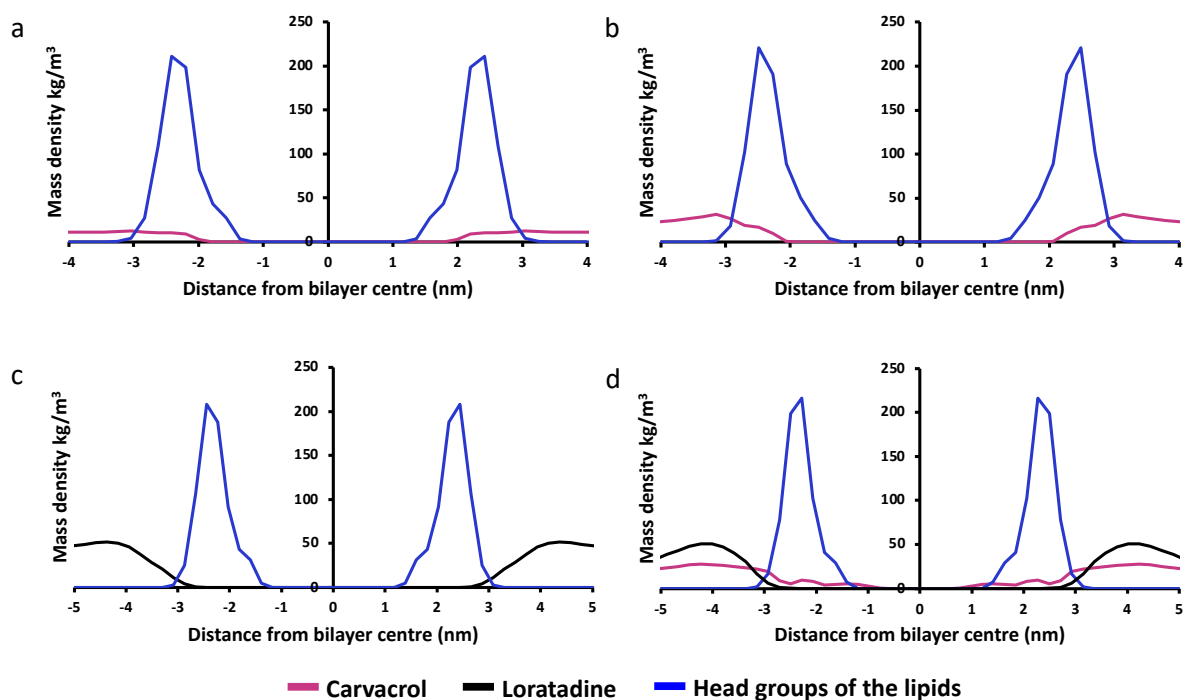


Figure 47. Mass density profiles of the healthy rigid membrane after the addition of (a) 8 carvacrol molecules, (b) 16 carvacrol molecules, (c) 8 loratadine molecules and (d) the combination of 16 carvacrol with 8 loratadine molecules.

From the mass density profiles presented in Figure 47a, Figure 47b and Figure 47d, it can be noted that carvacrol does penetrate the lipid head group area in the healthy rigid membrane. This can be observed from the overlaps which occur between blue (lipid head groups) and magenta purple (carvacrol) profiles. However, the density of carvacrol inside the membrane remains 0 nm across these profiles except in the case with the combination of drugs where some carvacrol molecules can be found inside the membrane near the lipid head group region. But no carvacrol or loratadine molecules are found in the midplane. Loratadine in any case in this membrane does not permeate the membrane bilayer. For Figure 47c the lines for loratadine are raised at each end in the mass density profile. By looking at the corresponding VMD image in Figure 36c this can be correlated to the formation of the loratadine aggregate in the water phase outside of the membrane bilayer. Results from Ahmed Irfan (2020) have also found limonene molecules to aggregate in a pure PSM and healthy membrane system as what was achieved here for loratadine. The author also reported some carvacrol molecules to have permeated the healthy rigid membrane. With loratadine being quite hydrophobic, it would be expected for it to permeate any membrane system without any problems. However, there could be a large barrier for loratadine to go through the head group region. By calculating the free energy of transfer of carvacrol and/or the loratadine molecules from the water phase to the membrane this would bring in more information about the system behaviour. However, calculating free energy was an impossible task due to the restricted nature in the computational resources available for this.

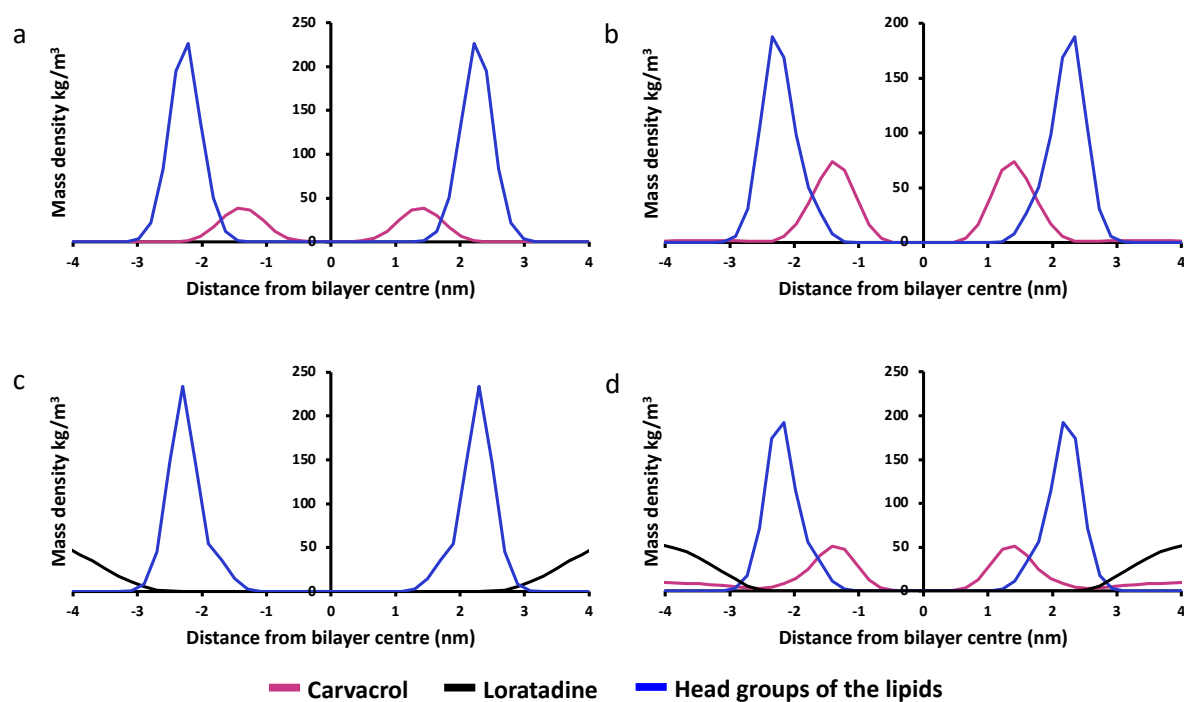


Figure 48. Mass density profiles of the healthy intermediate membrane after the addition of (a) 8 carvacrol molecules, (b) 16 carvacrol molecules, (c) 8 loratadine molecules and (d) the combination of 16 carvacrol with 8 loratadine molecules.

In the case of the healthy intermediate membrane through the mass density profiles, it can be noted that the carvacrol molecules do penetrate this membrane. The 16 carvacrol molecules in Figure 48b have a shorter distance to the centre of the bilayer and a larger maxima compared to 8 carvacrol molecules in Figure 48a as there are twice as many carvacrol molecules present. This has also been reflected in the VMD images in Figure 37a and Figure 37b. Ahmed Irfan (2020) also achieved similar findings as their carvacrol penetrated the healthy intermediate membrane with the molecules mainly lingering near the head groups. For loratadine the mass density is 0 nm inside the membrane showing that the molecules do not permeate the healthy intermediate membrane and remain in the water phase with a much further distance away from the centre of the bilayer. In combination most of the carvacrol molecules penetrate the membrane and are near the lipid head groups hence the overlap in the profiles. A few carvacrol molecules also remain unable to penetrate the membrane thus the slight raise at the end of the mass density profile in Figure 48d for carvacrol and in respect to the VMD image in Figure 37d.

Membrane thickness data calculated via the distances between the maxima of the head groups for the different membranes are presented in Figure 49. The results show the thickness for cancer and healthy membranes with and without the addition of the drugs.

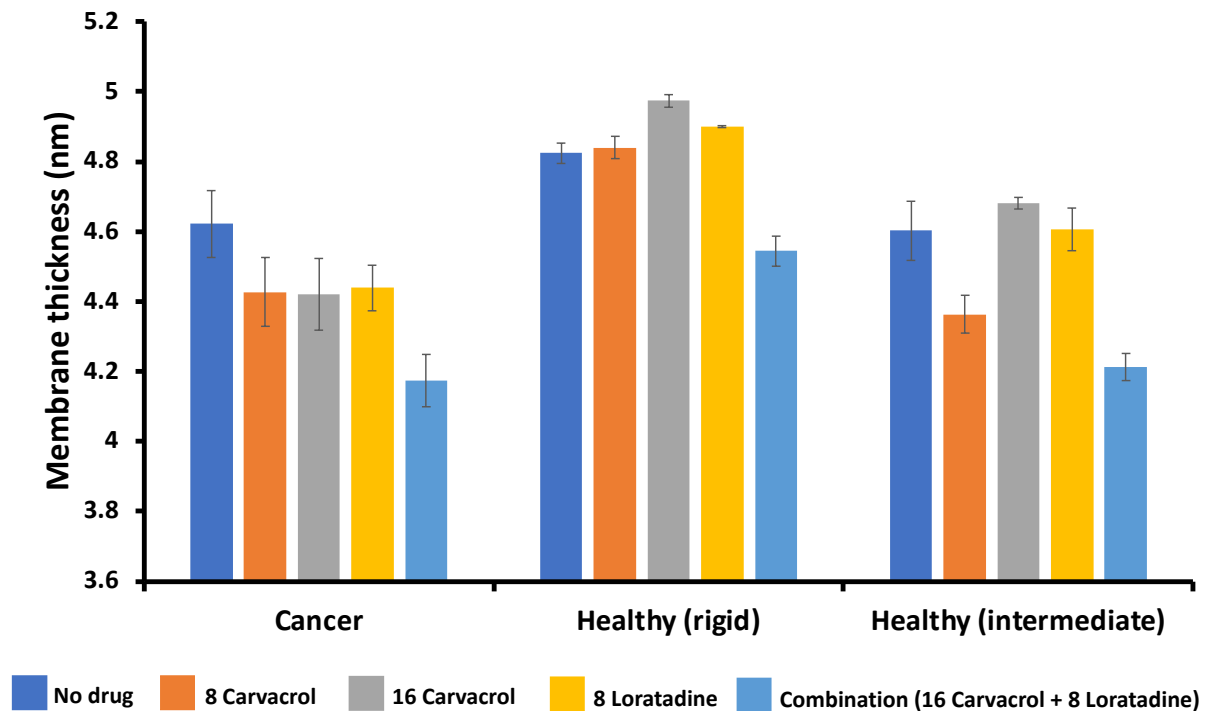


Figure 49. Average membrane thickness for each membrane system before and after the addition of carvacrol and loratadine.

From the results of the membrane thickness, it was found that the cancer membrane was the thinnest out of all systems, while the healthy rigid membrane was the thickest one. Before the drugs were added to the membrane it achieved a thickness of 4.62 ± 0.10 nm. The membrane thickness decreases overall from addition of all drug molecules whether individually or in combination. The healthy rigid membrane obtained a membrane thickness of 4.82 ± 0.03 nm, before the addition of the drugs, making it the thickest between all membrane systems. Although this did not increase by a significantly large amount there was a slight increase upon the addition of 16 carvacrol and 8 loratadine molecules to 4.97 ± 0.02 nm and 4.89 ± 0.003 nm respectively. For the rest, the membrane thickness decreased. The healthy intermediate membrane achieved a membrane thickness of 4.60 ± 0.08 nm, with only a 0.018 nm difference between the cancer membrane. Similarly, as what was found for the healthy rigid membrane, the membrane thickness for the healthy intermediate slightly

increased upon the addition of 16 carvacrol and 8 loratadine molecules and decreased for the rest.

Bera and Klauda (2017) found that the membrane thickness for a pure POPC membrane bilayer increases when CHOL and PSM lipids are added to the system. This was especially true for PSM as it was found that the increasing concentrations of PSM led to further increase in the membrane thickness overall. Additionally, Shinoda (2016) has also mentioned that one of the effects of CHOL is that it leads to an increase in membrane thickness in a phospholipid membrane system. From Das et al. (2009), CHOL was reported to affect the membrane thickness of phospholipid and skin membranes in the opposite manner. CHOL increased the membrane thickness (and tail order) in the case of the phospholipid membrane but decreased the thickness (and tail order) in the case of very rigid skin lipids. Moreover, in terms of membrane thickness, the authors Wang and Meng (2017) found that the increasing concentrations of up to 64 menthol molecules in the ceramide membrane had led to a significant increase in the membrane thickness overall. The leaflets in the ceramide membrane were parted resulting from some of the menthol molecules which were found in the centre of this bilayer. While the membrane did not part in our results, increasing the concentration of carvacrol from 8 molecules to 16 molecules did see the increase in membrane thickness for both healthy membrane systems as mentioned above. Other changes may have also been observed had we also used 64 carvacrol molecules. Moreover, many computational studies have found that membrane thickness decreases upon the addition of ethanol while the opposite is found for xenon which increases the membrane thickness (Hantal et al., 2019). Therefore, our results for membrane thickness are in line with what has been achieved in literature. The healthy membrane systems, which contain higher levels of CHOL and PSM, did obtain the higher membrane thickness in comparison to the cancer membrane system. Thus, for carvacrol and loratadine it was much more difficult, or it took longer to penetrate a thicker membrane which reflect the results produced for the healthy rigid and healthy intermediate membranes.

6.2.6 Hydrogen bonds

The head groups present in the composition of lipids allow them to form hydrogen bonds with the different components of the membrane bilayer as well as with the water molecules that

surround the lipid bilayer. Hydrogen bond interactions overall are essentially responsible for not only the stability of the lipid membrane bilayer but also for many biological processes and membrane function dynamics which occur in the lipid bilayer (Moradi et al., 2019). Therefore, assessing the different hydrogen bond interactions which can occur in the membrane bilayer is necessary to see any changes which may occur upon the addition of drugs to their systems.

The distance to angle criteria was used to calculate the hydrogen bonds. For distance the cut-off point was 0.35 nm between the hydrogen bond donor and acceptor also known as the donor-acceptor distance, while the cut-off angle was 30° between the hydrogen, the donor, and the acceptor atoms. The groups which are regarded as the hydrogen bond donors are both OH and NH, while the atoms which are regarded as the hydrogen bond acceptors are O and N (Lindahl et al., 2021; Saeedimazine et al., 2019). In order to analyse the hydrogen bonds which occurred in the cancer and healthy membrane systems, the GROMACS tool *gmx_hbond* was used.

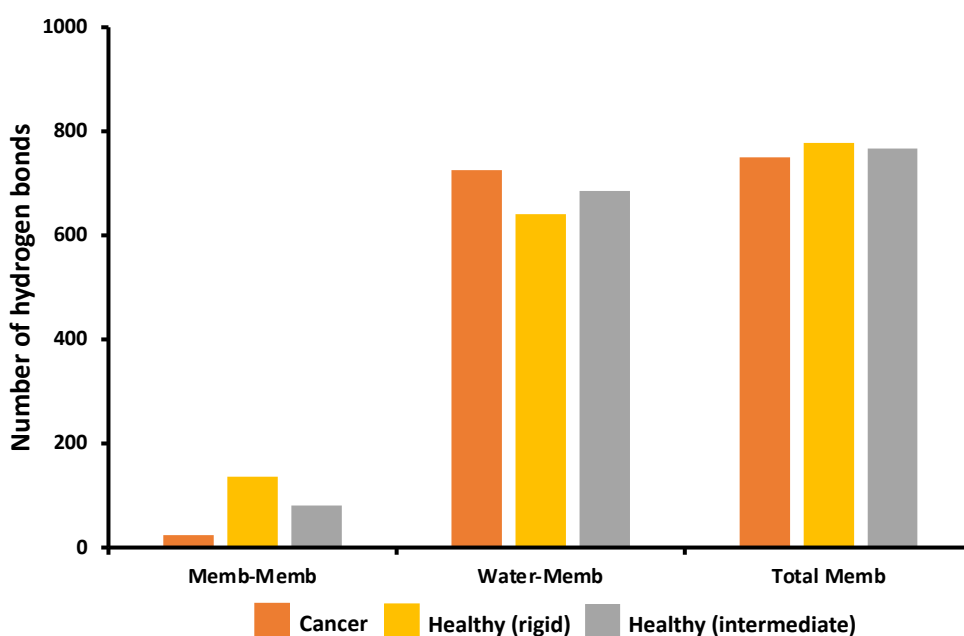


Figure 50. The number of hydrogen bonds formed between the lipids (Membrane-Membrane), between the water and the lipid membrane (Water-Membrane) and total hydrogen bonds formed in the membrane (Total Membrane) before any drugs were added to the cancer and healthy membrane systems.

Due to time restrictions, SD for the case of hydrogen bonds was unable to be calculated as triplicates and the results provided are in accordance with what was achieved in the last MD

simulation. As shown in Figure 50, the cancer membrane has the lowest amount of hydrogen bonds which formed between the membrane lipids. By having the least amount of hydrogen bonds between the membrane lipids and highest number of hydrogen bonds between the water and membrane lipids, this means that the cancer membrane is able to be more flexible overall. On the other hand, the healthy rigid membrane had the highest amount of hydrogen bonds formed between the membrane lipids, more than double of that which was found for the cancer membrane thus making this membrane the least flexible out of all the membrane systems. This difference in hydrogen bonds formed can be explained through the structure of the lipids presented previously in Figure 26. POPC can only act as a hydrogen bond acceptor which can form two bonds, one with the carbonyl and the other with the phosphate oxygens. PSM, on the other hand, can act as both a hydrogen bond donor and hydrogen bond acceptor, giving it many more sites to form hydrogen bonds at such as the amide, hydroxyl and carbonyl groups found in its structure. So, membrane flexibility is affected not only by the saturation and length of the tails but also the ability to form hydrogen bonds. Therefore, PSM lipids or even skin lipid ceramides which are derived from PSM (Akinshina et al., 2016), can form far more rigid membranes with a strong hydrogen bond network.

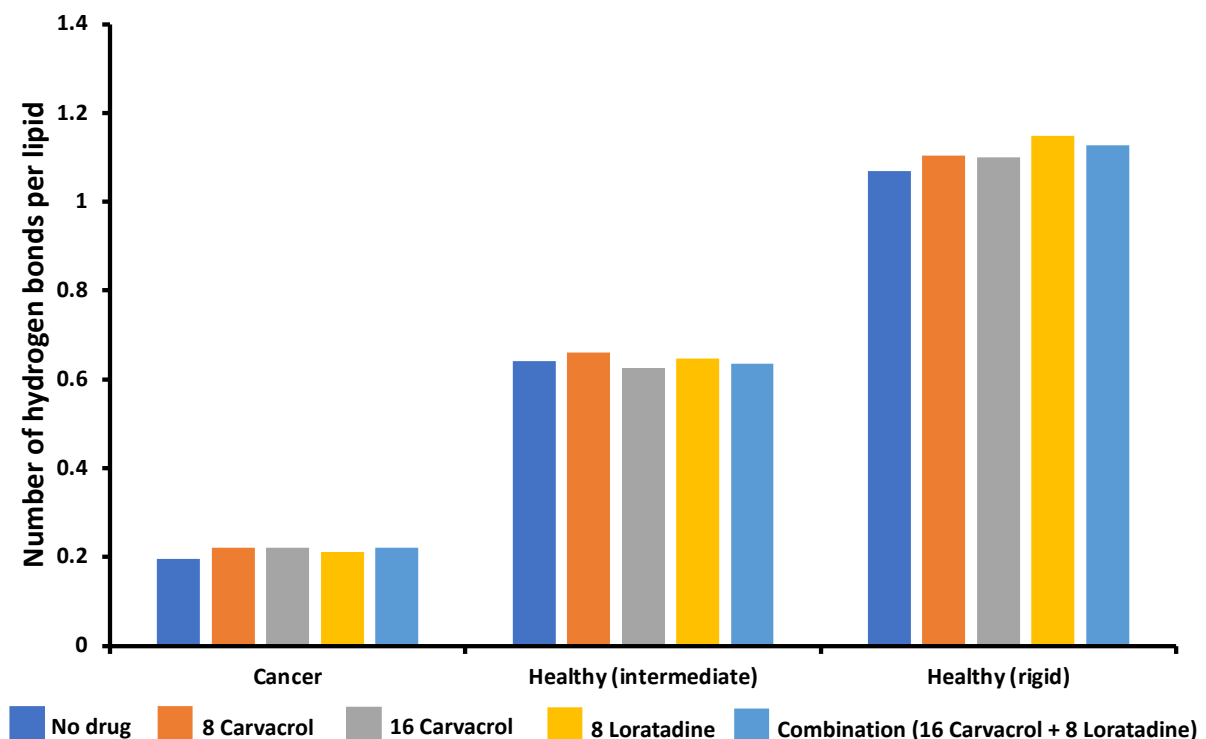


Figure 51. Total number of hydrogen bonds which are formed in the cancer and healthy membrane systems, per lipid for no drugs, 8 and 16 carvacrol molecules, 8 loratadine molecules and for the combination of both drugs.

From Figure 51, it can be noted that with the addition of carvacrol and loratadine individually and in combination did not influence the total amount of hydrogen bonds in the cancer and both healthy membrane systems per lipid. The highest number of hydrogen bonds came from the healthy rigid membrane whilst the lowest was achieved from the cancer membrane system.

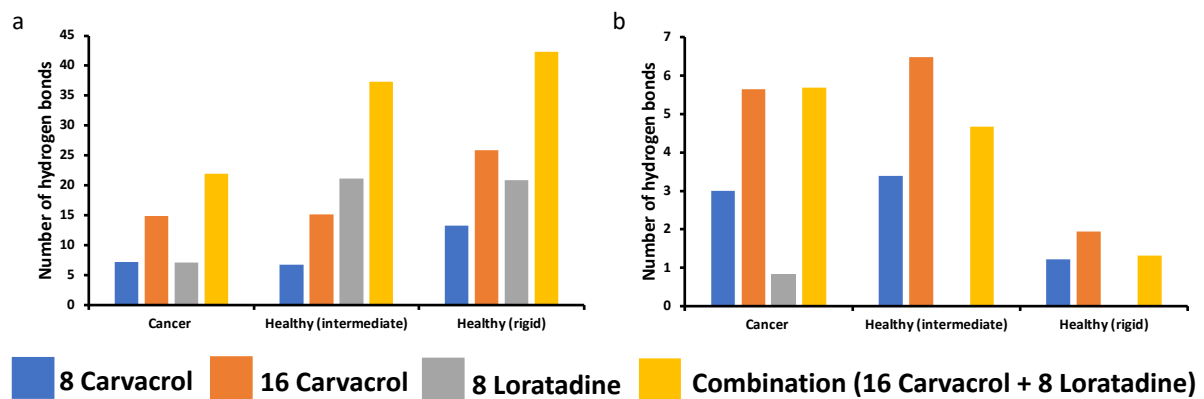


Figure 52. Number of hydrogen bonds formed after the addition of carvacrol and loratadine (a) with the water molecules and (b) with the membrane lipids.

The healthy rigid membrane forms the highest number of hydrogen bonds to the water molecules in the presence of carvacrol and loratadine individually and in combination. The opposite was true for the number of hydrogen bonds formed to the membrane lipids as this was the lowest for the healthy rigid membrane. In both healthy membrane models the loratadine molecules do not form any hydrogen bonds with the membrane lipids. This therefore suggests and further validates that carvacrol molecules were able to permeate the cancer and healthy intermediate membrane systems hence the number of hydrogen bonds formed with the water and membrane lipids, while loratadine only permeated the cancer membrane. The lack of hydrogen bonds with the lipids may be the reason for the loratadine molecules not interacting with the lipid head groups thus hindering their permeation.

In the work by Ahmed Irfan (2020), it was discovered that for the pure PSM, POPC and CHOL model membranes, the total number of hydrogen bonds overall was highest for the PSM membrane. This was due to the fact that both POPC and CHOL were unable to form hydrogen bonds between their lipids unlike PSM. Therefore, for both POPC and CHOL the only hydrogen bonds they can form are with the water molecules, which in that case was the highest for the

POPC membrane. Similar results for hydrogen bonds with the membrane lipids and water molecules in the cancer and healthy membrane systems was also achieved before and after the addition of carvacrol molecules. Thus, it can be suggested that the lower the number of hydrogen bonds which are formed between the membrane lipids, which in turn relates to the number of PSM or POPC lipids in the membrane composition, the more flexible the membrane system is.

6.2.7 Discussion of drug-membrane interactions

The interactions of different drugs with model membranes ultimately affects the way in which the lipids are packed within the membrane, the membrane thickness, and the overall ordering of the membrane. The decrease observed in APL for skin lipids studied by Wang and Meng (2017) can be correlated to the increase in the membrane bilayer thickness. In this work, the lipid tails of the ceramide membrane in the presence of either zero or a very low number of menthol molecules appear to have a tilt with the bilayer normal. On the other hand, the lipid tails were found to be much straighter and perpendicular to the bilayer surface upon the addition of larger concentration of menthol molecules. Similar effect on ceramides was also observed upon addition of unsaturated fatty acids and monoglycerides that disturb the membrane order, while the saturated ones make the membrane more rigid (Akinshina et al., 2016). In our case for the cancer membrane the lipid tails appeared much more disordered achieving the highest APL amongst the membrane systems hence making it the least tightly packed membrane. In the healthy rigid membrane, which contained higher concentrations of PSM, the lipid tails appeared straighter and in line with the bilayer normal. It achieved the lowest APL making it the most tightly packed membrane system while the results for the healthy intermediate membrane were in-between these. Moreover, although for high concentrations the menthol molecules for Wang and Meng (2017) were predominantly located inside the membrane near the midplane (pulling the leaflets apart), the drugs in our research project were localised much closer to the lipid headgroups (see Figures 35, 37, 46 and 48 above) in the membrane interior and therefore affected differently the lipid tail ordering and packing. One should also mention that the main effects in the menthol research was observed for very high amount of menthol molecules (32, 64 and 100), while for 16 menthols the effects were very negligible and comparable to our results. In another work by Witzke et al. (2010) mentioned previously, all four terpenes studied partitioned into the

bilayer in a similar manner as in our study. The penetrated terpenes also located near the headgroups and oriented parallel to the lipid tails (Figures 2 and 3 from Witzke et al. (2010)). Interesting that comparing the membrane changes upon addition of terpenes, three neutral terpenes (LIM, PALC and PALD) shows contradictory effects on membrane, such as increasing the tail order and membrane thickness (what would be logical) but also slightly increasing APL, while APL decrease would be expected in this case, similar to Wang and Meng (2017) results. The author argued that the slight increase in APL originates from the two opposing effects: penetration of the terpenes into the bilayer increases the distance between the headgroup and so increases APL, while ordering of the lipid tails decreases the area occupied by each lipid and so decreases the APL. Therefore, the combined effect on APL is very small. The reason why the APL affected differently in these two works is most possible due to location of the terpenes in the membrane – the midplane location would not affect the headgroups region, while the location near the headgroups would.

Loratadine is a poorly water-soluble drug. From the research of Guruge et al. (2021) who found that when loratadine is combined with a surfactant and oil, phase separation was observed in water. In both healthy membranes, the presence of 8 loratadine molecules seemed to form a cluster in the water phase of the modelled lipid membrane system. This was also the case when it was combined with 16 carvacrol molecules, as some carvacrol molecules seemed to have penetrated the healthy membranes but the loratadine molecules remained in the water phase and somewhat near the lipid head groups. According to the structure and solubility of loratadine, it should prefer to be in the lipid phase. However, as mentioned previously there is a possibility that there could be a large free energy barrier for loratadine molecules to cross the headgroup region of the lipid bilayer in order to immerse inside the membrane. Hence, it would be beneficial to carry out additional simulations where loratadine is placed inside the bilayer to investigate its affinity to lipid tails and also to calculate the free energy of translocation of loratadine (and carvacrol) inside the bilayer. The free energy barrier has also been observed for the anticancer drug doxorubicin which consists of multiple polar groups sites. Yacoub et al. (2011) found the free energy barrier for doxorubicin translocation across the DPPC and CHOL lipid membrane to be quite large especially in the midplane region. Furthermore, upon the increasing concentration of CHOL Yacoub et al. (2011) also found the free energy barrier changed from releasing doxorubicin

into the water to flip-flop over the midplane of the membrane. A different research group Meng and Xu (2013) also studied permeability of doxorubicin and two other more permeable drugs using DPPC bilayer (more rigid as DPPC is a saturated lipid) and their research shows two local free energy minima (where the drug could be temporary trapped) separated by a small barrier, and a larger (~ 10 kJ/mol) free energy barrier near the headgroups before the global minimum (~ -13 kJ/mol) after the headgroups, where the location of doxorubicin would be most favourable (Figure 2 from Meng and Xu (2013)). These barriers do not appear for the more permeable drugs. Therefore, analysing our results, it seems that in the case of cancer membrane the barrier could be small and easy for loratadine and carvacrol to overcome, but in the case of healthy rigid membrane the barriers are too large to cross spontaneously during considered simulation time.

Another interesting point of discussion would be considering the orientation of drugs inside the bilayer. Visual analysis of our and Witzke et al. (2010) images shows that the terpenes mostly oriented parallel to the lipid tails (bilayer normal). This is not always the case. Orsi et al. (2011) studied interactions of antimicrobials with aromatic rings, triclocarban and triclosan, with DOPC bilayer and in their case the antimicrobials oriented mostly perpendicular to bilayer normal. The reason for this is the structure of the antimicrobial molecules that contain several polar groups along the molecules that interact with the headgroups.

6.2.8 Discussion of lipid phases and lipid rafts

Lipid rafts are often described as being small, between 10-200 nm, highly dynamic and heterogenous (Ripa et al., 2021; Risselada & Marrink, 2008; Semrau & Schmidt, 2009). For ternary systems, *ld* (liquid disordered) phase usually contains unsaturated lipid and a small amount of cholesterol, while *lo* (liquid ordered) phase contains saturated lipid and a large amount of cholesterol (Bunge et al., 2008; Kaiser et al., 2009; Semrau & Schmidt, 2009). Some authors have argued there are two types of *lo* lipid rafts where the first type are enriched with assemblies of sphingolipids and CHOL (plays a key role in cell proliferation) and the second one is enriched in sphingolipids and ceramides that replace CHOL (plays a key role in cell apoptosis) (Zalba & ten Hagen, 2017). Lipid rafts are mainly found in the plasma membrane, intracellular membrane as well as the extracellular vesicles. The ternary systems

containing the three lipids from this research (POPC, PSM and CHOL) in different compositions and at two temperatures, 23 °C and 37 °C were used to study lipid rafts by De Almeida et al. (2003). The authors presented phase diagrams for ternary systems showing *lo* and *ld* states. Their research shows that there no “magical” raft mixture, raft-associated *lo*-domains can exist at various compositions and coexist with *ld*-domains. Mapping our compositions to the phase diagram at 37 °C (Figure 53) shows that our three membrane models fall into coexisting *ld* + *lo* phase region.

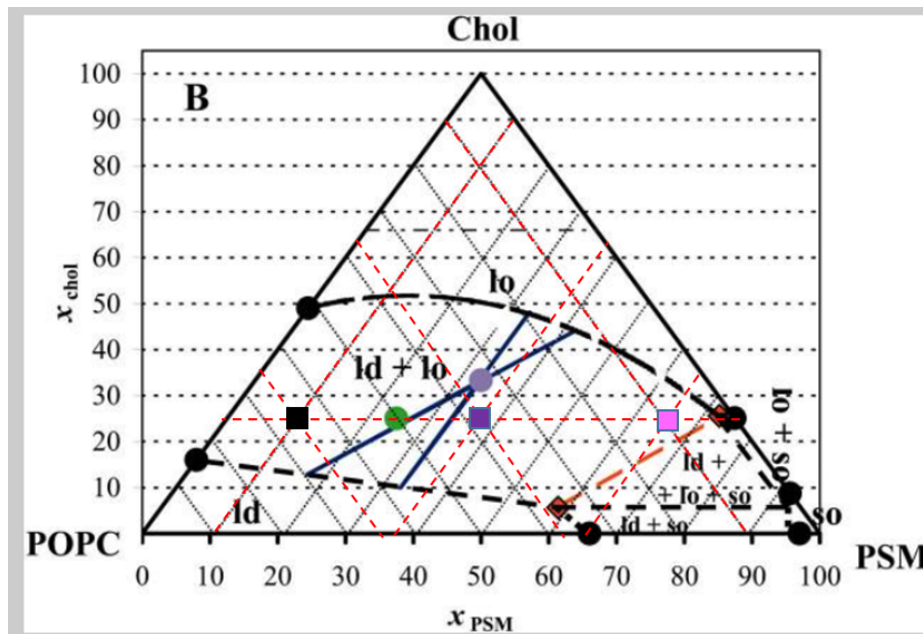


Figure 53. Mapping the lipid composition of the membranes used in this research into the ternary phase diagram for POPC/PSM/CHOL system at 37 °C. The composition for cancer (flexible) membrane is shown as black square, the composition for normal (rigid) membrane is shown as pink square, and the composition for normal (intermediate) membrane is shown as purple square in the middle. The red dashed lines show the lipid mol %. The image is adapted from De Almeida et al. (2003).

Applying to our membranes, ideally we should observe PSM+CHOL rich *lo* phase (so called lipid raft phase (Semrau & Schmidt, 2009) and predominantly POPC (with a few CHOL) *ld* phase. However, we were not able to clearly observe lipid phase separation in our systems. To detect and numerically assess phase separation into different phases in simulations a larger system is required, with a substantial amount of each lipid type present. The literature reports that at least 256 lipids (twice larger system comparing to ours) should be considered for atomistic simulations (Hall et al., 2010). Unfortunately, we do not have computational

resources for larger lipid systems. Lipid raft studies are often carried out using coarse-grained models, such as the MARTINI model (Marrink et al., 2007; Pezeshkian & Marrink, 2021; Schäfer & Marrink, 2010). The MARTINI model allows considering much larger modelling systems, up to thousands of lipids, for example Risselada and Marrink (2008) used 2000 lipid molecules, Li and Gorfe (2013) used 7320 lipids, and Ingólfsson et al. (2014) used 20,000 lipids in their lipid membranes studies. A reasonable future development of this project would be scaling up the number of lipids in the models considered using the MARTINI model for both lipids and the drugs. This would bring broader understanding of the lipid mixture behaviour and potential involvement of lipid raft formation into lipid-drug interactions.

By being able to differentiate and segregate certain elements these lipid rafts have the ability to regulate the interactions they have with other membrane components (Ripa et al., 2021). Sezgin et al. (2017) have stated that lipid rafts can cause changes in the conformation of proteins and consequently alter their bioactivity. As a result of this, lipid rafts are believed to play a crucial role in maintaining cellular functions. These cellular functions include the activation of receptors (Shi & Ruan, 2020), signal transduction (Simons & Ehehalt, 2002; Simons & Toomre, 2000), apoptosis (George & Wu, 2012) and exosome formation has also been linked to lipid rafts (Skryabin et al., 2020).

Unfortunately, taking into consideration of proteins is another aspect that was outside of the framework of this study. Previous and recent studies suggest that anticancer properties of terpenes, in particular carvacrol, are strongly related with altering protein activity, where some effect can originate from lipid raft reorganisation (Greay & Hammer, 2015). For example, Heidarian and Keloushadi (2019) found carvacrol decreasing the level of the interleukin-6 protein resulting in less cellular signalling proteins. This led to a decline in cell survival, proliferation, and the invasion of human prostate PC3 cells. Considering interaction of drugs with specific cytoplasmic proteins and/or membrane proteins could provide deeper insight into drug permeation and their mechanism of action. This could also answer the question that was impossible to address in the lipid-only study – how do the drugs cross the membrane? Our data show only that the studied drugs can permeate into the membrane and modify the membrane interior, but none of the drugs permeated out of the membrane. To

address these questions, a more complex membrane model with relevant embedded proteins is required.

Chapter 7 Conclusion

In conclusion, this current research project focused on the drug-cell interactions of extracranial RT, a rare childhood cancer, and the interactions with a novel combination of repurposed drugs i.e., carvacrol and loratadine. General cancer and healthy membrane models were also employed for the visual representation of the interactions which occurred upon the addition of the drugs to each of the membrane systems.

Ultimately, through experimental data it was revealed that both carvacrol and loratadine displayed a level of cytotoxicity to the A204 cells. Between both drugs it was loratadine which came out on top achieving an order of magnitude higher toxicity to the cells than carvacrol. Additionally, a synergistic effect was produced when the drugs were used in combination which meant that the combined effect of the drugs was better than that which was produced individually. However, more research and additional studies would be very much needed exploring the various concentration combinations of both drugs on other cancer cells lines in addition to normal healthy cell lines. This would allow comparisons to be made detailing the effects of the drug combinations not only in cancer but also healthy cell lines.

Analysing the three simulated membrane models presented we can conclude the model for “cancer” membrane is reasonably good and could form a basis for future more complex model that should include asymmetric leaflets and more lipid types, such as PE and PS lipids. However, the “healthy rigid” one is probably too rigid as the content of PSM is too high, but the “healthy intermediate” as a better model from the two presented and also could be used as a first step for creating more realistic model. The drug permeation results show that while both drugs were able to permeate into the cancer membrane, neither of the drugs permeated the healthy rigid membrane. Healthy intermediate membrane was found to be permeable for small carvacrol, but not large loratadine. The differences in permeation were found to be related to the lipid composition of each mixed lipid membrane system. The cancer membrane containing higher levels of POPC allowed better overall flexibility and fluidity of the membrane. The healthy rigid membrane containing higher levels of PSM and CHOL resulted

in greater overall rigidity thus making it more difficult for the drugs to permeate this membrane.

Upon permeation of the cancer membrane the carvacrol molecules were found to be near the head group of the membrane lipids while the loratadine molecules were located deeper in the membrane inside the hydrocarbon tail region but avoided the membrane midplane. The reason for this is that loratadine is bulkier molecule and occupy almost whole length of the lipid tails. For the healthy rigid membrane, the drug molecules just stayed in the water phase above and below the lipid bilayer. The obvious explanation would be the large free energy barrier for crossing the headgroup area as both drugs are hydrophobic and should favour being in lipid interior.

The properties of the cancer membrane upon addition of the drugs alter in a predicted manner. As all the drugs permeated the membrane, the APL increases while the thickness decreases, and the tail order also decreases but only slightly. Regarding the healthy rigid membrane, we can conclude that all the properties remain unaffected by the drugs (the fluctuations were within the error bars). For the healthy intermediate membrane, the APL increases for the permeated drugs and remains unaffected for non-permeated loratadine. The tail order slightly decreases. The data for the membrane thickness look inconclusive, as thickness drastically decreases for 8 CAR and CAR+LOR but remains practically unaffected for 16 CAR and LOR. Different results for 8 and 16 CAR are surprising, as similar effect was expected as CAR permeated the membrane. Probably in this case longer simulation or deeper analysis is required. Comparing compressibility modulus data, we can conclude that addition of the drugs does not affect membrane stiffness – the compressibility modulus data show no significant effect for all types of the drugs and membranes. The lowest values of the compressibility modulus (230-290 dyne/cm) were observed for cancer membrane, with the values in line with the literature data for phospholipid membranes comprised mostly of unsaturated lipids (POPC, 270-400 dyne/cm, (Janosi & Gorfe, 2010)). The highest values for compressibility modulus (1100-1400 dyne/cm) were observed for healthy rigid membrane rich in PSM and CHOL and for healthy intermediate membrane, the values are between the two extreme cases above, around 400-500 dyne/cm; these results are also in line with literature data (Jójárt & Martinek, 2007; Li et al., 2001; Miyoshi & Kato, 2015; Wang & Klauda, 2017). The last analysis was the amount of hydrogen bonds per lipid. The lowest values (~0.2

bonds/lipid) were observed for cancer membrane, the intermediate values (~0.6 bonds/lipid) for intermediate membrane, and the highest values (1-1.1 bonds/lipid) for the rigid membranes. This result could be explained by high amount of PSM, that can act as both donor and acceptor, in rigid and intermediate membranes. However, again we do not see any effect of the h-bonds upon addition of the drugs, probably because the drugs have low h-bond forming ability.

Future work, as mentioned previously, could include calculating free energy of transfer of the drug molecules from the water phase to the membrane. Larger systems could also be considered with many more lipids of each type to evaluate the size effect. Employing coarse-grained model, for example MARTINI, would allow consideration of larger systems and longer time scale. In addition to this, embedding proteins into the membrane bilayer and looking into the effects of this can also be considered.

Much comprehensive information has been obtained for drugs that are currently not used in childhood cancer treatment but could be, when used in combination therapy to augment the effectiveness of current treatment regimes. Through the combination of experimental and computational approaches the findings suggest and further reiterate the potential benefits of using non-cancer drugs for the treatment of childhood RT.

References

- Abraham, M. J., Murtola, T., Schulz, R., Páll, S., Smith, J. C., Hess, B., & Lindahl, E. (2015). GROMACS: High performance molecular simulations through multi-level parallelism from laptops to supercomputers. *SoftwareX*, 1-2, 19-25. <https://doi.org/https://doi.org/10.1016/j.softx.2015.06.001>
- Abraham, M. J., Van Der Spoel, D., Lindahl, E., & Hess, B. (2014). *GROMACS User Manual version 5.0.4*. www.gromacs.org
- Adams, D. B., & Morgan, K. A. (2019). Chapter 66 - Miscellaneous Benign Lesions and Conditions of the Stomach, Duodenum, and Small Intestine. In C. J. Yeo (Ed.), *Shackelford's Surgery of the Alimentary Tract, 2 Volume Set (Eighth Edition)* (pp. 764-769). Elsevier. <https://doi.org/https://doi.org/10.1016/B978-0-323-40232-3.00066-2>
- Adelusi, T. I., Oyedele, A.-Q. K., Boyenle, I. D., Ogunlana, A. T., Adeyemi, R. O., Ukachi, C. D., . . . Abdul-Hammed, M. (2022). Molecular modeling in drug discovery. *Informatics in Medicine Unlocked*, 29, 100880. <https://doi.org/https://doi.org/10.1016/j.imu.2022.100880>
- Agrons, G. A., Kingsman, K. D., Wagner, B. J., & Sotelo-Avila, C. (1997). Rhabdoid tumor of the kidney in children: a comparative study of 21 cases. *American Journal of Roentgenology*, 168(2), 447-451. <https://doi.org/10.2214/ajr.168.2.9016225>
- Ahmed Irfan, K. (2020). *Effect of monoterpenes on model cancer and healthy cell membranes: combined molecular dynamics simulation and cell toxicity study* [Research Placement Report]. University of Salford.
- Akinshina, A., Das, C., & Noro, M. G. (2016). Effect of monoglycerides and fatty acids on a ceramide bilayer [10.1039/C6CP01238H]. *Physical Chemistry Chemical Physics*, 18(26), 17446-17460. <https://doi.org/10.1039/C6CP01238H>
- Alam, M. I., Beg, S., Samad, A., Baboota, S., Kohli, K., Ali, J., . . . Akbar, M. (2010). Strategy for effective brain drug delivery. *European Journal of Pharmaceutical Sciences*, 40(5), 385-403. <https://doi.org/https://doi.org/10.1016/j.ejps.2010.05.003>
- Alsop, R. J., Khondker, A., Hub, J. S., & Rheinstädter, M. C. (2016). The Lipid Bilayer Provides a Site for Cortisone Crystallization at High Cortisone Concentrations. *Scientific Reports*, 6(1), 22425. <https://doi.org/10.1038/srep22425>
- Alves, A. C., Ribeiro, D., Nunes, C., & Reis, S. (2016). Biophysics in cancer: The relevance of drug-membrane interaction studies. *Biochimica et Biophysica Acta (BBA) - Biomembranes*, 1858(9), 2231-2244. <https://doi.org/https://doi.org/10.1016/j.bbamem.2016.06.025>
- AMBERMD. (2022). *The Amber Molecular Dynamics Package*. Retrieved May 5 2022 from <https://ambermd.org/GetAmber.php>
- Andoh, Y., Aoki, N., & Okazaki, S. (2016). Molecular dynamics study of lipid bilayers modeling the plasma membranes of mouse hepatocytes and hepatomas. *The Journal of Chemical Physics*, 144(8), 085104. <https://doi.org/10.1063/1.4942159>
- Andoh, Y., Okazaki, S., & Ueoka, R. (2013). Molecular dynamics study of lipid bilayers modeling the plasma membranes of normal murine thymocytes and leukemic GRSL cells. *Biochimica et Biophysica Acta (BBA) - Biomembranes*, 1828(4), 1259-1270. <https://doi.org/https://doi.org/10.1016/j.bbamem.2013.01.005>

- Arsov, Z., González-Ramírez, E. J., Goñi, F. M., Tristram-Nagle, S., & Nagle, J. F. (2018). Phase behavior of palmitoyl and egg sphingomyelin. *Chemistry and physics of lipids*, *213*, 102-110. <https://doi.org/10.1016/j.chemphyslip.2018.03.003>
- Arunasree, K. M. (2010). Anti-proliferative effects of carvacrol on a human metastatic breast cancer cell line, MDA-MB 231. *Phytomedicine*, *17*(8-9), 581-588. <https://doi.org/10.1016/j.phymed.2009.12.008>
- Askins, M. A., & Moore, B. D., 3rd. (2008). Preventing neurocognitive late effects in childhood cancer survivors. *Journal of child neurology*, *23*(10), 1160-1171. <https://doi.org/10.1177/0883073808321065>
- Aslantürk, Ö. S. (2017). In Vitro Cytotoxicity and Cell Viability Assays: Principles, Advantages, and Disadvantages. In *Genotoxicity - A Predictable Risk To Our Actual World*. <https://doi.org/10.5772/intechopen.71923>
- Athale, U. H., Duckworth, J., Odame, I., & Barr, R. (2009). Childhood atypical teratoid rhabdoid tumor of the central nervous system: a meta-analysis of observational studies. *J Pediatr Hematol Oncol*, *31*(9), 651-663. <https://doi.org/10.1097/MPH.0b013e3181b258a9>
- Baker, M. J., Trevisan, J., Bassan, P., Bhargava, R., Butler, H. J., Dorling, K. M., . . . Martin, F. L. (2014). Using Fourier transform IR spectroscopy to analyze biological materials. *Nature protocols*, *9*(8), 1771-1791. <https://doi.org/10.1038/nprot.2014.110>
- Barth, A. (2007). Infrared spectroscopy of proteins. *Biochimica et Biophysica Acta (BBA) - Bioenergetics*, *1767*(9), 1073-1101. <https://doi.org/https://doi.org/10.1016/j.bbabi.2007.06.004>
- Baykal-Köse, S., Acikgoz, E., Yavuz, A. S., Gönül Gevik, Ö., Ateş, H., Sezerman, O. U., . . . Yüce, Z. (2020). Adaptive phenotypic modulations lead to therapy resistance in chronic myeloid leukemia cells. *PLoS One*, *15*(2), e0229104-e0229104. <https://doi.org/10.1371/journal.pone.0229104>
- Bera, I., & Klauda, J. B. (2017). Molecular Simulations of Mixed Lipid Bilayers with Sphingomyelin, Glycerophospholipids, and Cholesterol. *The Journal of Physical Chemistry B*, *121*(20), 5197-5208. <https://doi.org/10.1021/acs.jpcc.7b00359>
- Bernardino de la Serna, J., Schütz, G. J., Eggeling, C., & Cebecauer, M. (2016). There Is No Simple Model of the Plasma Membrane Organization [Review]. *Frontiers in Cell and Developmental Biology*, *4*(106). <https://doi.org/10.3389/fcell.2016.00106>
- Bijnsdorp, I. V., Giovannetti, E., & Peters, G. J. (2011). Analysis of Drug Interactions. In I. Cree (Ed.), *Cancer Cell Culture. Methods in Molecular Biology (Methods and Protocols)* (Vol. 731). Humana Press. https://doi.org/https://doi.org/10.1007/978-1-61779-080-5_34
- Biswas, A., Kashyap, L., Kakkar, A., Sarkar, C., & Julka, P. K. (2016). Atypical teratoid/rhabdoid tumors: challenges and search for solutions. *Cancer management and research*, *8*, 115-125. <https://doi.org/10.2147/CMAR.S83472>
- Blass, B. E. (2015). Chapter 13 - Case Studies in Drug Discovery. In B. E. Blass (Ed.), *Basic Principles of Drug Discovery and Development* (pp. 499-529). Academic Press. <https://doi.org/https://doi.org/10.1016/B978-0-12-411508-8.00013-X>
- Bors, L. A., & Erdő, F. (2019). Overcoming the Blood–Brain Barrier. Challenges and Tricks for CNS Drug Delivery. *Sci. Pharm*, *87*(1), 6. <https://doi.org/10.3390/scipharm87010006>
- Botan, A., Favela-Rosales, F., Fuchs, P. F. J., Javanainen, M., Kanduč, M., Kulig, W., . . . Tynkkynen, J. (2015). Toward Atomistic Resolution Structure of Phosphatidylcholine Headgroup and Glycerol Backbone at Different Ambient Conditions. *The Journal of*

- Physical Chemistry B*, 119(49), 15075-15088.
<https://doi.org/10.1021/acs.jpcc.5b04878>
- Boyer, A., Pasquier, E., Tomasini, P., Ciccolini, J., Greillier, L., Andre, N., . . . Mascaux, C. (2018). Drug repurposing in malignant pleural mesothelioma: a breath of fresh air? *Eur Respir Rev*, 27(147). <https://doi.org/10.1183/16000617.0098-2017>
- Brennan, B., Stiller, C., & Bourdeaut, F. (2013). Extracranial rhabdoid tumours: what we have learned so far and future directions. *Lancet Oncol*, 14(8), e329-336.
[https://doi.org/10.1016/S1470-2045\(13\)70088-3](https://doi.org/10.1016/S1470-2045(13)70088-3)
- Brierley, J., Gospodarowicz, M., & O'Sullivan, B. (2016). The principles of cancer staging. *Ecancermedicalscience*, 10, ed61-ed61. <https://doi.org/10.3332/ecancer.2016.ed61>
- Brierley, J., O'Sullivan, B., Asamura, H., Byrd, D., Huang, S. H., Lee, A., . . . Gospodarowicz, M. (2019). Global Consultation on Cancer Staging: promoting consistent understanding and use. *Nature Reviews Clinical Oncology*, 16(12), 763-771.
<https://doi.org/10.1038/s41571-019-0253-x>
- Brok, J., Treger, T. D., Gooskens, S. L., van den Heuvel-Eibrink, M. M., & Pritchard-Jones, K. (2016). Biology and treatment of renal tumours in childhood. *European Journal of Cancer*, 68, 179-195. <https://doi.org/https://doi.org/10.1016/j.ejca.2016.09.005>
- Bunge, A., Müller, P., Stöckl, M., Herrmann, A., & Huster, D. (2008). Characterization of the Ternary Mixture of Sphingomyelin, POPC, and Cholesterol: Support for an Inhomogeneous Lipid Distribution at High Temperatures. *Biophysical Journal*, 94(7), 2680-2690. <https://doi.org/https://doi.org/10.1529/biophysj.107.112904>
- Buscariollo, D. L., Park, H. S., Roberts, K. B., & Yu, J. B. (2012). Survival outcomes in atypical teratoid rhabdoid tumor for patients undergoing radiotherapy in a Surveillance, Epidemiology, and End Results analysis. *Cancer*, 118(17), 4212-4219.
<https://doi.org/10.1002/cncr.27373>
- Casares, D., Escribá, P. V., & Rosselló, C. A. (2019). Membrane Lipid Composition: Effect on Membrane and Organelle Structure, Function and Compartmentalization and Therapeutic Avenues. *International journal of molecular sciences*, 20(9), 2167.
<https://doi.org/10.3390/ijms20092167>
- Case, D. A., Cheatham, T. E., 3rd, Darden, T., Gohlke, H., Luo, R., Merz, K. M., Jr., . . . Woods, R. J. (2005). The Amber biomolecular simulation programs. *Journal of Computational Chemistry*, 26(16), 1668-1688. <https://doi.org/10.1002/jcc.20290>
- Childers, M. C., & Daggett, V. (2018). Validating Molecular Dynamics Simulations against Experimental Observables in Light of Underlying Conformational Ensembles. *The journal of physical chemistry. B*, 122(26), 6673-6689.
<https://doi.org/10.1021/acs.jpcc.8b02144>
- Chou, T.-C. (2010). Drug Combination Studies and Their Synergy Quantification Using the Chou-Talalay Method. *Cancer Research*, 70(2), 440-446.
<https://doi.org/10.1158/0008-5472.Can-09-1947>
- Chrabaszcz, K., Jaształ, A., Smęda, M., Zieliński, B., Błaż, A., Diem, M., . . . Marzec, K. M. (2018). Label-free FTIR spectroscopy detects and visualizes the early stage of pulmonary micrometastasis seeded from breast carcinoma. *Biochimica et Biophysica Acta (BBA) - Molecular Basis of Disease*, 1864(11), 3574-3584.
<https://doi.org/https://doi.org/10.1016/j.bbadis.2018.08.022>
- Chung, C. J., Lorenzo, R., Rayder, S., Schemankewitz, E., Guy, C. D., Cutting, J., & Munden, M. (1995). Rhabdoid tumors of the kidney in children: CT findings. *AJR Am J Roentgenol*, 164(3), 697-700. <https://doi.org/10.2214/ajr.164.3.7863897>

- Cinosi, V., Antonini, R., Crateri, P., & Arancia, G. (2011). Modifications in plasma membrane lipid composition and morphological features of AH-130 hepatoma cells by polyenylphosphatidylcholine in vivo treatment. *Oncol Rep*, *26*(1), 229-235. <https://doi.org/10.3892/or.2011.1272>
- Collins, S. A., Guinn, B. A., Harrison, P. T., Scallan, M. F., O'Sullivan, G. C., & Tangney, M. (2008). Viral vectors in cancer immunotherapy: which vector for which strategy? *Curr Gene Ther*, *8*(2), 66-78. <https://doi.org/10.2174/156652308784049345>
- Cooper, G. M. (2000). *The Cell: A Molecular Approach* (2nd ed.). Sinauer Associates. <https://www.ncbi.nlm.nih.gov/books/NBK9839/>
- Csoboz, B., Balogh, G. E., Kusz, E., Gombos, I., Peter, M., Crul, T., . . . Vigh, L. (2013). Membrane fluidity matters: Hyperthermia from the aspects of lipids and membranes. *International Journal of Hyperthermia*, *29*(5), 491-499. <https://doi.org/10.3109/02656736.2013.808765>
- Dai, W., Sun, C., Huang, S., & Zhou, Q. (2016). Carvacrol suppresses proliferation and invasion in human oral squamous cell carcinoma. *Oncotargets and therapy*, *9*, 2297-2304. <https://doi.org/10.2147/OTT.S98875>
- Daleke, D. L. (2008). Regulation of phospholipid asymmetry in the erythrocyte membrane. *Curr Opin Hematol*, *15*(3), 191-195. <https://doi.org/10.1097/MOH.0b013e3282f97af7>
- Daneman, R., & Prat, A. (2015). The blood-brain barrier. *Cold Spring Harbor perspectives in biology*, *7*(1), a020412-a020412. <https://doi.org/10.1101/cshperspect.a020412>
- Das, C., Noro, M. G., & Olmsted, P. D. (2009). Simulation Studies of Stratum Corneum Lipid Mixtures. *Biophysical Journal*, *97*(7), 1941-1951. <https://doi.org/10.1016/j.bpj.2009.06.054>
- Dasari, S., & Tchounwou, P. B. (2014). Cisplatin in cancer therapy: molecular mechanisms of action. *European journal of pharmacology*, *740*, 364-378. <https://doi.org/10.1016/j.ejphar.2014.07.025>
- De Almeida, R. F. M., Fedorov, A., & Prieto, M. (2003). Sphingomyelin/phosphatidylcholine/cholesterol phase diagram: boundaries and composition of lipid rafts. *Biophysical Journal*, *85*(4), 2406-2416. [https://doi.org/10.1016/S0006-3495\(03\)74664-5](https://doi.org/10.1016/S0006-3495(03)74664-5)
- De Vivo, M., Masetti, M., Bottegoni, G., & Cavalli, A. (2016). Role of Molecular Dynamics and Related Methods in Drug Discovery. *Journal of Medicinal Chemistry*, *59*(9), 4035-4061. <https://doi.org/10.1021/acs.jmedchem.5b01684>
- Derenne, A., Vandersleyen, O., & Goormaghtigh, E. (2014). Lipid quantification method using FTIR spectroscopy applied on cancer cell extracts. *Biochim Biophys Acta*, *1841*(8), 1200-1209. <https://doi.org/10.1016/j.bbailip.2013.10.010>
- Desai, P., Thakkar, A., Ann, D., Wang, J., & Prabhu, S. (2019). Loratadine self-microemulsifying drug delivery systems (SMEDDS) in combination with sulforaphane for the synergistic chemoprevention of pancreatic cancer. *Drug delivery and translational research*, *9*(3), 641-651. <https://doi.org/10.1007/s13346-019-00619-0>
- Di, L., Kerns, E. H., & Di, L. (2008). *Drug-Like Properties: Concepts, Structure Design and Methods : From ADME to Toxicity Optimization*. Elsevier Science & Technology. <http://ebookcentral.proquest.com/lib/salford/detail.action?docID=365589>
- Dobbs, M. D., Correa, H., Schwartz, H. S., & Kan, J. H. (2011). Extrarenal rhabdoid tumor mimicking a sacral peripheral nerve sheath tumor. *Skeletal Radiol*, *40*(10), 1363-1368. <https://doi.org/10.1007/s00256-011-1160-0>

- Doherty, J., Zhang, Z., Wehbe, K., Cinque, G., Gardner, P., & Denbigh, J. (2018). Increased optical pathlength through aqueous media for the infrared microanalysis of live cells. *Analytical and Bioanalytical Chemistry*, 410(23), 5779-5789. <https://doi.org/10.1007/s00216-018-1188-2>
- Doktorova, M., LeVine, M. V., Khelashvili, G., & Weinstein, H. (2019). A New Computational Method for Membrane Compressibility: Bilayer Mechanical Thickness Revisited. *Biophysical Journal*, 116(3), 487-502. <https://doi.org/https://doi.org/10.1016/j.bpj.2018.12.016>
- Dong, X. (2018). Current Strategies for Brain Drug Delivery. *Theranostics*, 8(6), 1481-1493. <https://doi.org/10.7150/thno.21254>
- Dorak, M. T., & Karpuzoglu, E. (2012). Gender differences in cancer susceptibility: an inadequately addressed issue. *Front Genet*, 3, 268. <https://doi.org/10.3389/fgene.2012.00268>
- Dreissig, I., Machill, S., Salzer, R., & Krafft, C. (2009). Quantification of brain lipids by FTIR spectroscopy and partial least squares regression. *Spectrochimica Acta Part A: Molecular and Biomolecular Spectroscopy*, 71(5), 2069-2075. <https://doi.org/https://doi.org/10.1016/j.saa.2008.08.008>
- Dubus, E., Ijjaali, I., Barberan, O., & Petitet, F. (2009). Drug repositioning using in silico compound profiling. *Future Med Chem*, 1(9), 1723-1736. <https://doi.org/10.4155/fmc.09.123>
- Duffner, P. K., Armstrong, F. D., Chen, L., Helton, K. J., Brecher, M. L., Bell, B., & Chauvenet, A. R. (2014). Neurocognitive and neuroradiologic central nervous system late effects in children treated on Pediatric Oncology Group (POG) P9605 (standard risk) and P9201 (lesser risk) acute lymphoblastic leukemia protocols (ACCL0131): a methotrexate consequence? A report from the Children's Oncology Group. *J Pediatr Hematol Oncol*, 36(1), 8-15. <https://doi.org/10.1097/mpg.0000000000000000>
- Durrant, J. D., & McCammon, J. A. (2011). Molecular dynamics simulations and drug discovery. *BMC Biology*, 9(1), 71. <https://doi.org/10.1186/1741-7007-9-71>
- Dyrna, F., Hanske, S., Krueger, M., & Bechmann, I. (2013). The Blood-Brain Barrier. *Journal of Neuroimmune Pharmacology*, 8(4), 763-773. <https://doi.org/10.1007/s11481-013-9473-5>
- Eastman, R. T., Roth, J. S., Brimacombe, K. R., Simeonov, A., Shen, M., Patnaik, S., & Hall, M. D. (2020). Remdesivir: A Review of Its Discovery and Development Leading to Emergency Use Authorization for Treatment of COVID-19. *ACS Cent Sci*, 6(5), 672-683. <https://doi.org/10.1021/acscentsci.0c00489>
- Edelmann, M. N., Krull, K. R., Liu, W., Glass, J. O., Ji, Q., Ogg, R. J., . . . Reddick, W. E. (2014). Diffusion tensor imaging and neurocognition in survivors of childhood acute lymphoblastic leukaemia. *Brain*, 137(Pt 11), 2973-2983. <https://doi.org/10.1093/brain/awu230>
- Ellegaard, A. M., Dehlendorff, C., Vind, A. C., Anand, A., Cederkvist, L., Petersen, N. H. T., . . . Jaattela, M. (2016). Repurposing Cationic Amphiphilic Antihistamines for Cancer Treatment. *EBioMedicine*, 9, 130-139. <https://doi.org/10.1016/j.ebiom.2016.06.013>
- Escribá, P. V., González-Ros, J. M., Goñi, F. M., Kinnunen, P. K. J., Vigh, L., Sánchez-Magraner, L., . . . Barceló-Coblijn, G. (2008). Membranes: a meeting point for lipids, proteins and therapies. *Journal of cellular and molecular medicine*, 12(3), 829-875. <https://doi.org/10.1111/j.1582-4934.2008.00281.x>

- Fale, P. L., Altharawi, A., & Chan, K. L. (2015). In situ Fourier transform infrared analysis of live cells' response to doxorubicin. *Biochim Biophys Acta*, 1853(10 Pt A), 2640-2648. <https://doi.org/10.1016/j.bbamcr.2015.07.018>
- Feitelson, M. A., Arzumanyan, A., Kulathinal, R. J., Blain, S. W., Holcombe, R. F., Mahajna, J., . . . Nowsheen, S. (2015). Sustained proliferation in cancer: Mechanisms and novel therapeutic targets. *Seminars in cancer biology*, 35 Suppl(Suppl), S25-S54. <https://doi.org/10.1016/j.semcan.2015.02.006>
- Feller, S. E. (2000). Molecular dynamics simulations of lipid bilayers. *Current Opinion in Colloid & Interface Science*, 5(3), 217-223. [https://doi.org/https://doi.org/10.1016/S1359-0294\(00\)00058-3](https://doi.org/https://doi.org/10.1016/S1359-0294(00)00058-3)
- Fernald, K., & Kurokawa, M. (2013). Evading apoptosis in cancer. *Trends in cell biology*, 23(12), 620-633. <https://doi.org/10.1016/j.tcb.2013.07.006>
- Fouad, Y. A., & Aanei, C. (2017). Revisiting the hallmarks of cancer. *American journal of cancer research*, 7(5), 1016-1036. <https://www.ncbi.nlm.nih.gov/pmc/articles/PMC5446472/>
- Fritz, I., Wagner, P., Broberg, P., Einfeldt, R., & Olsson, H. (2020). Desloratadine and loratadine stand out among common H1-antihistamines for association with improved breast cancer survival. *Acta Oncologica*, 59(9), 1103-1109. <https://doi.org/10.1080/0284186X.2020.1769185>
- Fuertes, M. A., Castilla, J., Alonso, C., & Perez, J. M. (2003). Cisplatin biochemical mechanism of action: from cytotoxicity to induction of cell death through interconnections between apoptotic and necrotic pathways. *Curr Med Chem*, 10(3), 257-266. <https://doi.org/10.2174/0929867033368484>
- Gao, W., Liu, Y., Jing, G., Li, K., Zhao, Y., Sha, B., . . . Wu, D. (2017). Rapid and efficient crossing blood-brain barrier: Hydrophobic drug delivery system based on propionylated amylose helix nanoclusters. *Biomaterials*, 113, 133-144. <https://doi.org/10.1016/j.biomaterials.2016.10.045>
- Gardner, S. L., Asgharzadeh, S., Green, A., Horn, B., McCowage, G., & Finlay, J. (2008). Intensive induction chemotherapy followed by high dose chemotherapy with autologous hematopoietic progenitor cell rescue in young children newly diagnosed with central nervous system atypical teratoid rhabdoid tumors. *Pediatr Blood Cancer*, 51(2), 235-240. <https://doi.org/10.1002/pbc.21578>
- Geller, J. I., Roth, J. J., & Biegel, J. A. (2015). Biology and Treatment of Rhabdoid Tumor. *Crit Rev Oncog*, 20(3-4), 199-216. <https://doi.org/10.1615/critrevoncog.2015013566>
- George, K. S., & Wu, S. (2012). Lipid raft: A floating island of death or survival. *Toxicology and applied pharmacology*, 259(3), 311-319. <https://doi.org/10.1016/j.taap.2012.01.007>
- Ginn, K. F., & Gajjar, A. (2012). Atypical teratoid rhabdoid tumor: current therapy and future directions. *Frontiers in Oncology*, 2, 114-114. <https://doi.org/10.3389/fonc.2012.00114>
- Goñi, F. M. (2014). The basic structure and dynamics of cell membranes: An update of the Singer–Nicolson model. *Biochimica et Biophysica Acta (BBA) - Biomembranes*, 1838(6), 1467-1476. <https://doi.org/https://doi.org/10.1016/j.bbamem.2014.01.006>
- Greay, S. J., & Hammer, K. A. (2015). Recent developments in the bioactivity of mono- and diterpenes: anticancer and antimicrobial activity. *Phytochemistry Reviews*, 14(1), 1-6. <https://doi.org/10.1007/s11101-011-9212-6>

- Greene, F. L., & Sobin, L. H. (2008). The Staging of Cancer: A Retrospective and Prospective Appraisal. *CA: A Cancer Journal for Clinicians*, *58*(3), 180-190. <https://doi.org/https://doi.org/10.3322/CA.2008.0001>
- Grein, J., Ohmagari, N., Shin, D., Diaz, G., Asperges, E., Castagna, A., . . . Flanigan, T. (2020). Compassionate Use of Remdesivir for Patients with Severe Covid-19. *New England Journal of Medicine*, *382*(24), 2327-2336. <https://doi.org/10.1056/NEJMoa2007016>
- Gu, R.-X., Baoukina, S., & Tieleman, D. P. (2019). Cholesterol Flip-Flop in Heterogeneous Membranes. *Journal of Chemical Theory and Computation*, *15*(3), 2064-2070. <https://doi.org/10.1021/acs.jctc.8b00933>
- Gündüz, K., Shields, J. A., Eagle, R. C., Jr, Shields, C. L., De Potter, P., & Klombers, L. (1998). Malignant Rhabdoid Tumor of the Orbit. *Archives of Ophthalmology*, *116*(2), 243-246. <https://doi.org/10.1001/archopht.116.2.243>
- Günes-Bayir, A., Kocyigit, A., Güler, E. M., Bilgin, M. G., Ergün, İ. S., & Dadak, A. (2018). Effects of carvacrol on human fibroblast (WS-1) and gastric adenocarcinoma (AGS) cells in vitro and on Wistar rats in vivo. *Molecular and Cellular Biochemistry*, *448*(1), 237-249. <https://doi.org/10.1007/s11010-018-3329-5>
- Guruge, A. G., Warren, D. B., Benameur, H., Ford, L., Williams, H. D., Jannin, V., . . . Chalmers, D. K. (2021). Computational and Experimental Models of Type III Lipid-Based Formulations of Loratadine Containing Complex Nonionic Surfactants. *Molecular Pharmaceutics*, *18*(12), 4354-4370. <https://doi.org/10.1021/acs.molpharmaceut.1c00547>
- Gutschner, T., & Diederichs, S. (2012). The hallmarks of cancer: a long non-coding RNA point of view. *RNA biology*, *9*(6), 703-719. <https://doi.org/10.4161/rna.20481>
- Hall, A., Róg, T., Karttunen, M., & Vattulainen, I. (2010). Role of Glycolipids in Lipid Rafts: A View through Atomistic Molecular Dynamics Simulations with Galactosylceramide. *The Journal of Physical Chemistry B*, *114*(23), 7797-7807. <https://doi.org/10.1021/jp912175d>
- Hanafy, N. A. N., El-Kemary, M., & Leporatti, S. (2018). Micelles Structure Development as a Strategy to Improve Smart Cancer Therapy. *Cancers*, *10*(7), 238. <https://doi.org/10.3390/cancers10070238>
- Hanahan, D., & Weinberg, Robert A. (2011). Hallmarks of Cancer: The Next Generation. *Cell*, *144*(5), 646-674. <https://doi.org/https://doi.org/10.1016/j.cell.2011.02.013>
- Hantal, G., Fábíán, B., Sega, M., Jójárt, B., & Jedlovsky, P. (2019). Effect of general anesthetics on the properties of lipid membranes of various compositions. *Biochimica et Biophysica Acta (BBA) - Biomembranes*, *1861*(3), 594-609. <https://doi.org/https://doi.org/10.1016/j.bbamem.2018.12.008>
- Harayama, T., & Riezman, H. (2018). Understanding the diversity of membrane lipid composition. *Nature Reviews Molecular Cell Biology*, *19*(5), 281-296. <https://doi.org/10.1038/nrm.2017.138>
- Haria, M., Fitton, A., & Peters, D. H. (1994). Loratadine. A reappraisal of its pharmacological properties and therapeutic use in allergic disorders. *Drugs*, *48*(4), 617-637. <https://doi.org/10.2165/00003495-199448040-00009>
- Heck, J. E., Lombardi, C. A., Cockburn, M., Meyers, T. J., Wilhelm, M., & Ritz, B. (2013). Epidemiology of rhabdoid tumors of early childhood. *Pediatric Blood & Cancer*, *60*(1), 77-81. <https://doi.org/10.1002/pbc.24141>
- Heidarian, E., & Keloushadi, M. (2019). Antiproliferative and Anti-invasion Effects of Carvacrol on PC3 Human Prostate Cancer Cells through Reducing pSTAT3, pAKT, and

- pERK1/2 Signaling Proteins. *International journal of preventive medicine*, 10, 156-156. https://doi.org/10.4103/ijpvm.IJPVM_292_17
- Hollingsworth, S. A., & Dror, R. O. (2018). Molecular Dynamics Simulation for All. *Neuron*, 99(6), 1129-1143. <https://doi.org/https://doi.org/10.1016/j.neuron.2018.08.011>
- Hopton, C. (2019). *Permeation of reactive oxygen species through model cancer and healthy cell membranes: insights from molecular dynamics simulations* [Year in Industry Project Report]. University of Salford.
- Hospital, A., Goñi, J. R., Orozco, M., & Gelpí, J. L. (2015). Molecular dynamics simulations: advances and applications. *Advances and applications in bioinformatics and chemistry : AABC*, 8, 37-47. <https://doi.org/10.2147/AABC.S70333>
- Hubbard, A. K., Spector, L. G., Fortuna, G., Marcotte, E. L., & Poynter, J. N. (2019). Trends in International Incidence of Pediatric Cancers in Children Under 5 Years of Age: 1988-2012. *JNCI cancer spectrum*, 3(1), pkz007-pkz007. <https://doi.org/10.1093/jncics/pkz007>
- Hudu, S. A., Alshrari, A. S., Syahida, A., & Sekawi, Z. (2016). Cell Culture, Technology: Enhancing the Culture of Diagnosing Human Diseases. *Journal of clinical and diagnostic research : JCDR*, 10(3), DE01-DE05. <https://doi.org/10.7860/JCDR/2016/15837.7460>
- Ingólfsson, H. I., Melo, M. N., van Eerden, F. J., Arnarez, C., Lopez, C. A., Wassenaar, T. A., . . . Marrink, S. J. (2014). Lipid Organization of the Plasma Membrane. *Journal of the American Chemical Society*, 136(41), 14554-14559. <https://doi.org/10.1021/ja507832e>
- Irwin, J. J., & Shoichet, B. K. (2005). ZINC--a free database of commercially available compounds for virtual screening. *Journal of chemical information and modeling*, 45(1), 177-182. <https://doi.org/10.1021/ci049714+>
- Jairam, V., Roberts, K. B., & Yu, J. B. (2013). Historical trends in the use of radiation therapy for pediatric cancers: 1973-2008. *International journal of radiation oncology, biology, physics*, 85(3), e151-e155. <https://doi.org/10.1016/j.ijrobp.2012.10.007>
- Janosi, L., & Gofre, A. A. (2010). Simulating POPC and POPC/POPG Bilayers: Conserved Packing and Altered Surface Reactivity. *Journal of Chemical Theory and Computation*, 6(10), 3267-3273. <https://doi.org/10.1021/ct100381g>
- Jo, S., Kim, T., Iyer, V. G., & Im, W. (2008). CHARMM-GUI: A web-based graphical user interface for CHARMM [<https://doi.org/10.1002/jcc.20945>]. *Journal of Computational Chemistry*, 29(11), 1859-1865. <https://doi.org/https://doi.org/10.1002/jcc.20945>
- Jórárt, B., & Martinek, T. A. (2007). Performance of the general amber force field in modeling aqueous POPC membrane bilayers [<https://doi.org/10.1002/jcc.20748>]. *Journal of Computational Chemistry*, 28(12), 2051-2058. <https://doi.org/https://doi.org/10.1002/jcc.20748>
- Jourdan, J.-P., Bureau, R., Rochais, C., & Dallemagne, P. (2020). Drug repositioning: a brief overview. *Journal of Pharmacy and Pharmacology*, n/a(n/a). <https://doi.org/10.1111/jphp.13273>
- Jung, C. Y., Kim, S. Y., & Lee, C. (2018). Carvacrol Targets AXL to Inhibit Cell Proliferation and Migration in Non-small Cell Lung Cancer Cells. *Anticancer Res*, 38(1), 279-286. <https://doi.org/10.21873/anticancer.12219>
- Kaiser, H.-J., Lingwood, D., Levental, I., Sampaio Julio, L., Kalvodova, L., Rajendran, L., & Simons, K. (2009). Order of lipid phases in model and plasma membranes.

- Proceedings of the National Academy of Sciences*, 106(39), 16645-16650.
<https://doi.org/10.1073/pnas.0908987106>
- Kim, D.-G., & Bynoe, M. S. (2016). A2A adenosine receptor modulates drug efflux transporter P-glycoprotein at the blood-brain barrier. *The Journal of clinical investigation*, 126(5), 1717-1733. <https://doi.org/10.1172/JCI76207>
- Klähn, M., & Zacharias, M. (2013). Transformations in plasma membranes of cancerous cells and resulting consequences for cation insertion studied with molecular dynamics [10.1039/C3CP52085D]. *Physical Chemistry Chemical Physics*, 15(34), 14427-14441. <https://doi.org/10.1039/C3CP52085D>
- Kohashi, K., Tanaka, Y., Kishimoto, H., Yamamoto, H., Yamada, Y., Taguchi, T., . . . Oda, Y. (2016). Reclassification of rhabdoid tumor and pediatric undifferentiated/unclassified sarcoma with complete loss of SMARCB1/INI1 protein expression: three subtypes of rhabdoid tumor according to their histological features. *Modern Pathology*, 29(10), 1232-1242. <https://doi.org/10.1038/modpathol.2016.106>
- Koizumi, K., Kano-Tanaka, K., Shimizu, S., Nishida, K., Yamanaka, N., & Ota, K. (1980). Lipids of plasma membranes from rat thymic lymphoid cells: deficiency of sphingomyelin. *Biochim Biophys Acta*, 619(2), 344-352. [https://doi.org/10.1016/0005-2760\(80\)90082-x](https://doi.org/10.1016/0005-2760(80)90082-x)
- Koparal, A. T., & Zeytinoglu, M. (2003). Effects of Carvacrol on a Human Non-Small Cell Lung Cancer (NSCLC) Cell Line, A549. *Cytotechnology*, 43(1-3), 149-154. <https://doi.org/10.1023/B:CYTO.0000039917.60348.45>
 10.1023/b:cyto.0000039917.60348.45
- Kozłowska, K., Nowak, J., Kwiatkowski, B., & Cichorek, M. (1999). ESR study of plasmatic membrane of the transplantable melanoma cells in relation to their biological properties. *Exp Toxicol Pathol*, 51(1), 89-92. [https://doi.org/10.1016/s0940-2993\(99\)80074-8](https://doi.org/10.1016/s0940-2993(99)80074-8)
- Kram, D. E., Henderson, J. J., Baig, M., Chakraborty, D., Gardner, M. A., Biswas, S., & Khatua, S. (2018). Embryonal Tumors of the Central Nervous System in Children: The Era of Targeted Therapeutics. *Bioengineering (Basel, Switzerland)*, 5(4), 78. <https://doi.org/10.3390/bioengineering5040078>
- Kučerka, N., Nieh, M.-P., & Katsaras, J. (2011). Fluid phase lipid areas and bilayer thicknesses of commonly used phosphatidylcholines as a function of temperature. *Biochimica et Biophysica Acta (BBA) - Biomembranes*, 1808(11), 2761-2771. <https://doi.org/https://doi.org/10.1016/j.bbamem.2011.07.022>
- Kuete, V., Karaosmanoğlu, O., & Sivas, H. (2017). Chapter 10 - Anticancer Activities of African Medicinal Spices and Vegetables. In V. Kuete (Ed.), *Medicinal Spices and Vegetables from Africa* (pp. 271-297). Academic Press. <https://doi.org/https://doi.org/10.1016/B978-0-12-809286-6.00010-8>
- Kutanzi, K. R., Lumen, A., Koturbash, I., & Miousse, I. R. (2016). Pediatric Exposures to Ionizing Radiation: Carcinogenic Considerations. *International journal of environmental research and public health*, 13(11), 1057. <https://doi.org/10.3390/ijerph13111057>
- Lafay-Cousin, L., Hawkins, C., Carret, A. S., Johnston, D., Zelcer, S., Wilson, B., . . . Huang, A. (2012). Central nervous system atypical teratoid rhabdoid tumours: the Canadian Paediatric Brain Tumour Consortium experience. *Eur J Cancer*, 48(3), 353-359. <https://doi.org/10.1016/j.ejca.2011.09.005>

- Lande, M. B., Donovan, J. M., & Zeidel, M. L. (1995). The relationship between membrane fluidity and permeabilities to water, solutes, ammonia, and protons. *The Journal of general physiology*, *106*(1), 67-84. <https://doi.org/10.1085/jgp.106.1.67>
- Le Naour, F., Sandt, C., Peng, C., Trcera, N., Chiappini, F., Flank, A. M., . . . Dumas, P. (2012). In situ chemical composition analysis of cirrhosis by combining synchrotron fourier transform infrared and synchrotron X-ray fluorescence microspectroscopies on the same tissue section. *Anal Chem*, *84*(23), 10260-10266. <https://doi.org/10.1021/ac302072t>
- Lee, J., Cheng, X., Swails, J. M., Yeom, M. S., Eastman, P. K., Lemkul, J. A., . . . Im, W. (2016). CHARMM-GUI Input Generator for NAMD, GROMACS, AMBER, OpenMM, and CHARMM/OpenMM Simulations Using the CHARMM36 Additive Force Field. *Journal of Chemical Theory and Computation*, *12*(1), 405-413. <https://doi.org/10.1021/acs.jctc.5b00935>
- Leekumjorn, S., & Sum, A. K. (2007). Molecular Characterization of Gel and Liquid-Crystalline Structures of Fully Hydrated POPC and POPE Bilayers. *The Journal of Physical Chemistry B*, *111*(21), 6026-6033. <https://doi.org/10.1021/jp0686339>
- Lewis, P. D., Lewis, K. E., Ghosal, R., Bayliss, S., Lloyd, A. J., Wills, J., . . . Mur, L. A. J. (2010). Evaluation of FTIR Spectroscopy as a diagnostic tool for lung cancer using sputum. *BMC Cancer*, *10*(1), 640. <https://doi.org/10.1186/1471-2407-10-640>
- Li, H., & Gorfe, A. A. (2013). Aggregation of Lipid-Anchored Full-Length H-Ras in Lipid Bilayers: Simulations with the MARTINI Force Field. *PLoS One*, *8*(7), e71018. <https://doi.org/10.1371/journal.pone.0071018>
- Li, X.-M., Momsen, M. M., Smaby, J. M., Brockman, H. L., & Brown, R. E. (2001). Cholesterol Decreases the Interfacial Elasticity and Detergent Solubility of Sphingomyelins. *Biochemistry*, *40*(20), 5954-5963. <https://doi.org/10.1021/bi002791n>
- Li, X.-M., Smaby, J. M., Momsen, M. M., Brockman, H. L., & Brown, R. E. (2000). Sphingomyelin Interfacial Behavior: The Impact of Changing Acyl Chain Composition. *Biophysical Journal*, *78*(4), 1921-1931. [https://doi.org/https://doi.org/10.1016/S0006-3495\(00\)76740-3](https://doi.org/https://doi.org/10.1016/S0006-3495(00)76740-3)
- Lim, S.-W., Loh, H.-S., Ting, K.-N., Bradshaw, T. D., & Allaudin, Z. N. (2015). Reduction of MTT to Purple Formazan by Vitamin E Isomers in the Absence of Cells. *Tropical life sciences research*, *26*(1), 111-120. <https://www.ncbi.nlm.nih.gov/pmc/articles/PMC4437321/>
- Lin, Y., Pan, D., Li, J., Zhang, L., & Shao, X. (2017). Application of Berendsen barostat in dissipative particle dynamics for nonequilibrium dynamic simulation. *J Chem Phys*, *146*(12), 124108. <https://doi.org/10.1063/1.4978807>
- Lindahl, E., Abraham, M. J., Hess, B., & Van Der Spoel, D. (2021). GROMACS 2021.3 Manual. *Zenodo*, *2021*(3). <https://doi.org/10.5281/zenodo.5053220>
- Liu, X., Shi, D., Zhou, S., Liu, H., Liu, H., & Yao, X. (2018). Molecular dynamics simulations and novel drug discovery. *Expert Opinion on Drug Discovery*, *13*(1), 23-37. <https://doi.org/10.1080/17460441.2018.1403419>
- Llado, V., Lopez, D. J., Ibarguren, M., Alonso, M., Soriano, J. B., Escriba, P. V., & Busquets, X. (2014). Regulation of the cancer cell membrane lipid composition by NaChOleate: effects on cell signaling and therapeutical relevance in glioma. *Biochim Biophys Acta*, *1838*(6), 1619-1627. <https://doi.org/10.1016/j.bbamem.2014.01.027>

- Lombardino, J. G., & Lowe, J. A. (2004). The role of the medicinal chemist in drug discovery — then and now. *Nature Reviews Drug Discovery*, 3(10), 853-862. <https://doi.org/10.1038/nrd1523>
- Lopes, D., Jakobtorweihen, S., Nunes, C., Sarmiento, B., & Reis, S. (2017). Shedding light on the puzzle of drug-membrane interactions: Experimental techniques and molecular dynamics simulations. *Progress in lipid research*, 65, 24-44. <https://doi.org/https://doi.org/10.1016/j.plipres.2016.12.001>
- Lopes, S. C., Ivanova, G., de Castro, B., & Gameiro, P. (2018). Revealing cardiolipins influence in the construction of a significant mitochondrial membrane model. *Biochimica et Biophysica Acta (BBA) - Biomembranes*, 1860(11), 2465-2477. <https://doi.org/https://doi.org/10.1016/j.bbamem.2018.07.006>
- Lopez-Romero, J. C., Gonzalez-Rios, H., Borges, A., & Simoes, M. (2015). Antibacterial Effects and Mode of Action of Selected Essential Oils Components against Escherichia coli and Staphylococcus aureus. *Evid Based Complement Alternat Med*, 2015, 795435. <https://doi.org/10.1155/2015/795435>
- Löscher, W., & Potschka, H. (2005). Blood-brain barrier active efflux transporters: ATP-binding cassette gene family. *NeuroRx : the journal of the American Society for Experimental NeuroTherapeutics*, 2(1), 86-98. <https://doi.org/10.1602/neurorx.2.1.86>
- Lovskaya, D., & Menshutina, N. (2020). Alginate-Based Aerogel Particles as Drug Delivery Systems: Investigation of the Supercritical Adsorption and In Vitro Evaluations. *Materials*, 13(2). <https://doi.org/10.3390/ma13020329>
- Lü, L., Zhang, L., Wai, M. S. M., Yew, D. T. W., & Xu, J. (2012). Exocytosis of MTT formazan could exacerbate cell injury. *Toxicology in Vitro*, 26(4), 636-644. <https://doi.org/https://doi.org/10.1016/j.tiv.2012.02.006>
- Mahler, S. M., Wilce, P. A., & Shanley, B. C. (1988). Studies on regenerating liver and hepatoma plasma membranes--I. Lipid and protein composition. *Int J Biochem*, 20(6), 605-611. [https://doi.org/10.1016/0020-711x\(88\)90100-0](https://doi.org/10.1016/0020-711x(88)90100-0)
- Marrink, S. J., Risselada, H. J., Yefimov, S., Tieleman, D. P., & de Vries, A. H. (2007). The MARTINI Force Field: Coarse Grained Model for Biomolecular Simulations. *The Journal of Physical Chemistry B*, 111(27), 7812-7824. <https://doi.org/10.1021/jp071097f>
- Marshall, C. (2021). *Thyme vs Oregano: What's the Difference for Chefs?* <https://thekitchencommunity.org/thyme-vs-oregano-whats-the-difference/>
- Martinez-Seara, H., Róg, T., Karttunen, M., Vattulainen, I., & Reigada, R. (2010). Cholesterol Induces Specific Spatial and Orientational Order in Cholesterol/Phospholipid Membranes. *PLoS One*, 5(6), e11162. <https://doi.org/10.1371/journal.pone.0011162>
- Matthews, H., Deakin, J., Rajab, M., Idris-Usman, M., & Nirmalan, N. J. (2017). Investigating antimalarial drug interactions of emetine dihydrochloride hydrate using CalcuSyn-based interactivity calculations. *PLoS One*, 12(3), e0173303. <https://doi.org/10.1371/journal.pone.0173303>
- Maulik, P. R., & Shipley, G. G. (1996). N-palmitoyl sphingomyelin bilayers: structure and interactions with cholesterol and dipalmitoylphosphatidylcholine. *Biochemistry*, 35(24), 8025-8034. <https://doi.org/10.1021/bi9528356>
- McAteer, J. A., & Davis, J. M. (2002). Basic cell culture technique the maintenance of cell lines In J. M. Davis (Ed.), *Basic Cell Culture* (2 ed., pp. 135 - 190). Oxford University Press Inc.

- Medina, D. X., Householder, K. T., Ceton, R., Kovalik, T., Heffernan, J. M., Shankar, R. V., . . . Sirianni, R. W. (2017). Optical barcoding of PLGA for multispectral analysis of nanoparticle fate in vivo. *J Control Release*, 253, 172-182. <https://doi.org/10.1016/j.jconrel.2017.02.033>
- Melušová, M., Jantová, S., & Horváthová, E. (2014). Carvacrol and rosemary oil at higher concentrations induce apoptosis in human hepatoma HepG2 cells. *Interdisciplinary toxicology*, 7(4), 189-194. <https://doi.org/10.2478/intox-2014-0027>
- Meng, F., & Xu, W. (2013). Drug permeability prediction using PMF method. *Journal of Molecular Modeling*, 19(3), 991-997. <https://doi.org/10.1007/s00894-012-1655-1>
- Minotti, G., Menna, P., Salvatorelli, E., Cairo, G., & Gianni, L. (2004). Anthracyclines: molecular advances and pharmacologic developments in antitumor activity and cardiotoxicity. *Pharmacol Rev*, 56(2), 185-229. <https://doi.org/10.1124/pr.56.2.6>
- Mirabelli, P., Coppola, L., & Salvatore, M. (2019). Cancer Cell Lines Are Useful Model Systems for Medical Research. *Cancers*, 11(8), 1098. <https://doi.org/10.3390/cancers11081098>
- Miyoshi, T., & Kato, S. (2015). Detailed Analysis of the Surface Area and Elasticity in the Saturated 1,2-Diacylphosphatidylcholine/Cholesterol Binary Monolayer System. *Langmuir*, 31(33), 9086-9096. <https://doi.org/10.1021/acs.langmuir.5b01775>
- Mohamed, M. A., Jaafar, J., Ismail, A. F., Othman, M. H. D., & Rahman, M. A. (2017). Chapter 1 - Fourier Transform Infrared (FTIR) Spectroscopy. In N. Hilal, A. F. Ismail, T. Matsuura, & D. Oatley-Radcliffe (Eds.), *Membrane Characterization* (pp. 3-29). Elsevier. <https://doi.org/https://doi.org/10.1016/B978-0-444-63776-5.00001-2>
- Moradi, S., Nowroozi, A., & Shahlaei, M. (2019). Shedding light on the structural properties of lipid bilayers using molecular dynamics simulation: a review study [10.1039/C8RA08441F]. *RSC Advances*, 9(8), 4644-4658. <https://doi.org/10.1039/C8RA08441F>
- Nesvick, C. L., Nageswara Rao, A. A., Raghunathan, A., Biegel, J. A., & Daniels, D. J. (2018). Case-based review: atypical teratoid/rhabdoid tumor. *Neuro-Oncology Practice*, 6(3), 163-178. <https://doi.org/10.1093/nop/npy037>
- Nian, B., Xu, Y.-J., & Liu, Y. (2021). Molecular dynamics simulation for mechanism revelation of the safety and nutrition of lipids and derivatives in food: State of the art. *Food Research International*, 145, 110399. <https://doi.org/https://doi.org/10.1016/j.foodres.2021.110399>
- Nicolson, G. L. (2014). The Fluid—Mosaic Model of Membrane Structure: Still relevant to understanding the structure, function and dynamics of biological membranes after more than 40years. *Biochimica et Biophysica Acta (BBA) - Biomembranes*, 1838(6), 1451-1466. <https://doi.org/https://doi.org/10.1016/j.bbamem.2013.10.019>
- Nicolson, G. L., & Ash, M. E. (2014). Lipid Replacement Therapy: A natural medicine approach to replacing damaged lipids in cellular membranes and organelles and restoring function. *Biochimica et Biophysica Acta (BBA) - Biomembranes*, 1838(6), 1657-1679. <https://doi.org/https://doi.org/10.1016/j.bbamem.2013.11.010>
- Niemelä, P., Hyvönen, M. T., & Vattulainen, I. (2004). Structure and dynamics of sphingomyelin bilayer: insight gained through systematic comparison to phosphatidylcholine. *Biophysical Journal*, 87(5), 2976-2989. <https://doi.org/10.1529/biophysj.104.048702>

- Notman, R., & Anwar, J. (2013). Breaching the skin barrier — Insights from molecular simulation of model membranes. *Advanced Drug Delivery Reviews*, 65(2), 237-250. <https://doi.org/https://doi.org/10.1016/j.addr.2012.02.011>
- Oita, S., Terui, K., Komatsu, S., Hishiki, T., Saito, T., Mitsunaga, T., . . . Yoshida, H. (2015). Malignant rhabdoid tumor of the liver: a case report and literature review. *Pediatric reports*, 7(1), 5578-5578. <https://doi.org/10.4081/pr.2015.5578>
- Olsson, H. L., Broberg, P., Einefors, R., & Fritz, I. (2018). Effects of antihistamine use on survival in breast cancer. *Journal of Clinical Oncology*, 36(15_suppl), e12527-e12527. https://doi.org/10.1200/JCO.2018.36.15_suppl.e12527
- Orsi, M., Noro, M. G., & Essex, J. W. (2011). Dual-resolution molecular dynamics simulation of antimicrobials in biomembranes. *Journal of The Royal Society Interface*, 8(59), 826-841. <https://doi.org/10.1098/rsif.2010.0541>
- Otto, T., & Sicinski, P. (2017). Cell cycle proteins as promising targets in cancer therapy. *Nature reviews. Cancer*, 17(2), 93-115. <https://doi.org/10.1038/nrc.2016.138>
- Ozkan, A., & Erdogan, A. (2012). A comparative study of the antioxidant/prooxidant effects of carvacrol and thymol at various concentrations on membrane and DNA of parental and drug resistant H1299 cells. *Nat Prod Commun*, 7(12), 1557-1560.
- Pantziarka, P., Bouche, G., & André, N. (2018). "Hard" Drug Repurposing for Precision Oncology: The Missing Link? *Frontiers in pharmacology*, 9, 637-637. <https://doi.org/10.3389/fphar.2018.00637>
- Panwar, P., Burusco, K. K., Abubaker, M., Matthews, H., Gutnov, A., Fernández-Álvaro, E., . . . Nirmalan, N. (2020). Lead Optimization of Dehydroemetine for Repositioned Use in Malaria. *Antimicrobial agents and chemotherapy*, 64(4), e01444-01419. <https://doi.org/10.1128/AAC.01444-19>
- Pardo, J., Shukla, A. M., Chamarthi, G., & Gupte, A. (2020). The journey of remdesivir: from Ebola to COVID-19. *Drugs in context*, 9, 2020-2024-2014. <https://doi.org/10.7573/dic.2020-4-14>
- Pardridge, W. M. (2012). Drug transport across the blood-brain barrier. *Journal of cerebral blood flow and metabolism : official journal of the International Society of Cerebral Blood Flow and Metabolism*, 32(11), 1959-1972. <https://doi.org/10.1038/jcbfm.2012.126>
- Patel, A. (2020). Benign vs Malignant Tumors. *JAMA Oncology*, 6(9), 1488-1488. <https://doi.org/10.1001/jamaoncol.2020.2592>
- Pérez-Martínez, F. C., Carrión, B., & Ceña, V. (2012). The Use of Nanoparticles for Gene Therapy in the Nervous System. *Journal of Alzheimer's Disease*, 31, 697-710. <https://doi.org/10.3233/JAD-2012-120661>
- Peura, L., Malmioja, K., Huttunen, K., Leppänen, J., Hämäläinen, M., Forsberg, M. M., . . . Laine, K. (2013). Design, synthesis and brain uptake of LAT1-targeted amino acid prodrugs of dopamine. *Pharm Res*, 30(10), 2523-2537. <https://doi.org/10.1007/s11095-012-0966-3>
- Pezeshkian, W., & Marrink, S. J. (2021). Simulating realistic membrane shapes. *Current Opinion in Cell Biology*, 71, 103-111. <https://doi.org/https://doi.org/10.1016/j.ceb.2021.02.009>
- Pfeffer, C. M., & Singh, A. T. K. (2018). Apoptosis: A Target for Anticancer Therapy. *International journal of molecular sciences*, 19(2), 448. <https://doi.org/10.3390/ijms19020448>

- Piccaluga, P. P., Agostinelli, C., Gazzola, A., Tripodo, C., Bacci, F., Sabattini, E., . . . Pileri, S. A. (2011). Pathobiology of Hodgkin Lymphoma. *Advances in Hematology*, 2011, 920898. <https://doi.org/10.1155/2011/920898>
- Popper, H. H. (2016). Progression and metastasis of lung cancer. *Cancer metastasis reviews*, 35(1), 75-91. <https://doi.org/10.1007/s10555-016-9618-0>
- Prados, M. D., Schold, S. C., Jr., Fine, H. A., Jaeckle, K., Hochberg, F., Mechtler, L., . . . Graney, W. (2003). A randomized, double-blind, placebo-controlled, phase 2 study of RMP-7 in combination with carboplatin administered intravenously for the treatment of recurrent malignant glioma. *Neuro-oncology*, 5(2), 96-103. <https://doi.org/10.1093/neuonc/5.2.96>
- Pratt, H. P. M., Saxon, A., & Graham, M. L. (1978). Membrane lipid changes associated with malignant transformation and normal maturation of human lymphocytes. *Leukemia Research*, 2(1), 1-10. [https://doi.org/https://doi.org/10.1016/0145-2126\(78\)90002-4](https://doi.org/https://doi.org/10.1016/0145-2126(78)90002-4)
- Pronk, S., Páll, S., Schulz, R., Larsson, P., Bjelkmar, P., Apostolov, R., . . . Lindahl, E. (2013). GROMACS 4.5: a high-throughput and highly parallel open source molecular simulation toolkit. *Bioinformatics (Oxford, England)*, 29(7), 845-854. <https://doi.org/10.1093/bioinformatics/btt055>
- Pushpakom, S., Iorio, F., Eyers, P. A., Escott, K. J., Hopper, S., Wells, A., . . . Pirmohamed, M. (2019). Drug repurposing: progress, challenges and recommendations. *Nature Reviews Drug Discovery*, 18(1), 41-58. <https://doi.org/10.1038/nrd.2018.168>
- Qosa, H., Miller, D. S., Pasinelli, P., & Trotti, D. (2015). Regulation of ABC efflux transporters at blood-brain barrier in health and neurological disorders. *Brain Research*, 1628, 298-316. <https://doi.org/https://doi.org/10.1016/j.brainres.2015.07.005>
- Rai, R., Iwanaga, J., Shokouhi, G., Oskouian, R. J., & Tubbs, R. S. (2018). The Tentorium Cerebelli: A Comprehensive Review Including Its Anatomy, Embryology, and Surgical Techniques. *Cureus*, 10(7), e3079-e3079. <https://doi.org/10.7759/cureus.3079>
- Rajabi, M., & Mousa, S. A. (2017). The Role of Angiogenesis in Cancer Treatment. *Biomedicines*, 5(2), 34. <https://doi.org/10.3390/biomedicines5020034>
- Randall, K. L., & Hawkins, C. A. (2018). Antihistamines and allergy. *Australian prescriber*, 41(2), 41-45. <https://doi.org/10.18773/austprescr.2018.013>
- Reddy, A., Strother, D., Judkins, A., Krailo, M., Gao, Y., Douglas, J., . . . Biegel, J. (2016). AT-09: TREATMENT OF ATYPICAL TERATOID RHABDOID TUMORS (ATRT) OF THE CENTRAL NERVOUS SYSTEM WITH SURGERY, INTENSIVE CHEMOTHERAPY, AND 3-D CONFORMAL RADIATION (ACNS0333). A REPORT FROM THE CHILDREN'S ONCOLOGY GROUP. *Neuro-Oncology*, 18(Suppl 3), iii2-iii2. <https://doi.org/10.1093/neuonc/now065.08>
- Redondo-Morata, L., Giannotti, M. I., & Sanz, F. (2012). Influence of cholesterol on the phase transition of lipid bilayers: a temperature-controlled force spectroscopy study. *Langmuir : the ACS journal of surfaces and colloids*, 28 (35), 12851-12860.
- Richardson, E. A., Ho, B., & Huang, A. (2018). Atypical Teratoid Rhabdoid Tumour : From Tumours to Therapies. *J Korean Neurosurg Soc*, 61(3), 302-311. <https://doi.org/10.3340/jkns.2018.0061>
- Ripa, I., Andreu, S., López-Guerrero, J. A., & Bello-Morales, R. (2021). Membrane Rafts: Portals for Viral Entry [Review]. *Frontiers in Microbiology*, 12. <https://doi.org/10.3389/fmicb.2021.631274>

- Risselada, H. J., & Marrink, S. J. (2008). The molecular face of lipid rafts in model membranes. *Proceedings of the National Academy of Sciences*, *105*(45), 17367-17372. <https://doi.org/10.1073/pnas.0807527105>
- Rivel, T., Ramseyer, C., & Yesylevskyy, S. (2019). The asymmetry of plasma membranes and their cholesterol content influence the uptake of cisplatin. *Scientific Reports*, *9*(1), 5627. <https://doi.org/10.1038/s41598-019-41903-w>
- Róg, T., Pasenkiewicz-Gierula, M., Vattulainen, I., & Karttunen, M. (2009). Ordering effects of cholesterol and its analogues. *Biochimica et Biophysica Acta (BBA) - Biomembranes*, *1788*(1), 97-121. <https://doi.org/https://doi.org/10.1016/j.bbamem.2008.08.022>
- Sabbatini, S., Conti, C., Orilisi, G., & Giorgini, E. (2017). Infrared spectroscopy as a new tool for studying single living cells: Is there a niche? *Biomedical Spectroscopy and Imaging*, *6*, 85-99. <https://doi.org/10.3233/BSI-170171>
- Saeedimazine, M., Montanino, A., Kleiven, S., & Villa, A. (2019). Role of lipid composition on the structural and mechanical features of axonal membranes: a molecular simulation study. *Scientific Reports*, *9*(1), 8000. <https://doi.org/10.1038/s41598-019-44318-9>
- Saletta, F., Seng, M. S., & Lau, L. M. S. (2014). Advances in paediatric cancer treatment. *Translational pediatrics*, *3*(2), 156-182. <https://doi.org/10.3978/j.issn.2224-4336.2014.02.01>
- Saraiva, C., Praça, C., Ferreira, R., Santos, T., Ferreira, L., & Bernardino, L. (2016). Nanoparticle-mediated brain drug delivery: Overcoming blood–brain barrier to treat neurodegenerative diseases. *Journal of Controlled Release*, *235*, 34-47. <https://doi.org/https://doi.org/10.1016/j.jconrel.2016.05.044>
- Schäfer, L. V., & Marrink, S. J. (2010). Partitioning of Lipids at Domain Boundaries in Model Membranes. *Biophysical Journal*, *99*(12), L91-L93. <https://doi.org/10.1016/j.bpj.2010.08.072>
- Schaffrath, J., Schmoll, H.-J., Voigt, W., Müller, L. P., Müller-Tidow, C., & Mueller, T. (2017). Efficacy of targeted drugs in germ cell cancer cell lines with differential cisplatin sensitivity. *PLoS One*, *12*(6), e0178930-e0178930. <https://doi.org/10.1371/journal.pone.0178930>
- Segeritz, C.-P., & Vallier, L. (2017). Cell Culture: Growing Cells as Model Systems In Vitro. *Basic Science Methods for Clinical Researchers*, 151-172. <https://doi.org/10.1016/B978-0-12-803077-6.00009-6>
- Semrau, S., & Schmidt, T. (2009). Membrane heterogeneity – from lipid domains to curvature effects [10.1039/B901587F]. *Soft Matter*, *5*(17), 3174-3186. <https://doi.org/10.1039/B901587F>
- Seyfried, T. N., & Huysentruyt, L. C. (2013). On the origin of cancer metastasis. *Critical reviews in oncogenesis*, *18*(1-2), 43-73. <https://doi.org/10.1615/critrevoncog.v18.i1-2.40>
- Sezgin, E., Levental, I., Mayor, S., & Eggeling, C. (2017). The mystery of membrane organization: composition, regulation and roles of lipid rafts. *Nature reviews. Molecular cell biology*, *18*(6), 361-374. <https://doi.org/10.1038/nrm.2017.16>
- Shahane, G., Ding, W., Palaiokostas, M., & Orsi, M. (2019). Physical properties of model biological lipid bilayers: insights from all-atom molecular dynamics simulations. *J Mol Model*, *25*(3), 76. <https://doi.org/10.1007/s00894-019-3964-0>
- Sherbet, G. V. (1989). Membrane fluidity and cancer metastasis. *Exp Cell Biol*, *57*(4), 198-205. <https://doi.org/10.1159/000163526>

- Shi, Y., & Ruan, H. (2020). Toward a Membrane-Centric Biology. *Frontiers in immunology*, 11, 1909-1909. <https://doi.org/10.3389/fimmu.2020.01909>
- Shih, R. Y., & Koeller, K. K. (2018). Embryonal Tumors of the Central Nervous System: From the Radiologic Pathology Archives. *RadioGraphics*, 38(2), 525-541. <https://doi.org/10.1148/rg.2018170182>
- Shim, J. S., & Liu, J. O. (2014). Recent advances in drug repositioning for the discovery of new anticancer drugs. *International journal of biological sciences*, 10(7), 654-663. <https://doi.org/10.7150/ijbs.9224>
- Shinitzky, M. (1984). Membrane fluidity in malignancy Adversative and recuperative. *Biochimica et Biophysica Acta (BBA) - Reviews on Cancer*, 738(4), 251-261. [https://doi.org/https://doi.org/10.1016/0304-419X\(83\)90007-0](https://doi.org/https://doi.org/10.1016/0304-419X(83)90007-0)
- Shinoda, W. (2016). Permeability across lipid membranes. *Biochimica et Biophysica Acta (BBA) - Biomembranes*, 1858(10), 2254-2265. <https://doi.org/https://doi.org/10.1016/j.bbamem.2016.03.032>
- Shokripour, M., Azarpira, N., Omidifar, N., & Pakniat, B. (2017). Cytologic diagnosis of atypical teratoid rhabdoid tumor based on touch imprint study: Report of a case with review of literature. *Journal of education and health promotion*, 6, 59-59. https://doi.org/10.4103/jehp.jehp_8_17
- Siegel, R. L., Miller, K. D., & Jemal, A. (2019). Cancer statistics, 2019. *CA: A Cancer Journal for Clinicians*, 69(1), 7-34. <https://doi.org/10.3322/caac.21551>
- Siegel, R. L., Miller, K. D., & Jemal, A. (2020). Cancer statistics, 2020. *CA: A Cancer Journal for Clinicians*, 70(1), 7-30. <https://doi.org/https://doi.org/10.3322/caac.21590>
- Silvius, J. R. (1982). Thermotropic Phase Transitions of Pure Lipids in Model Membranes and Their Modifications by Membrane Proteins. In *Lipid-Protein Interactions* (pp. 188-189). John Wiley & Sons, Inc.
- Simons, K., & Ehehalt, R. (2002). Cholesterol, lipid rafts, and disease. *The Journal of clinical investigation*, 110(5), 597-603. <https://doi.org/10.1172/JCI16390>
- Simons, K., & Toomre, D. (2000). Lipid rafts and signal transduction. *Nature Reviews Molecular Cell Biology*, 1(1), 31-39. <https://doi.org/10.1038/35036052>
- Singer, S. J., & Nicolson, G. L. (1972). The fluid mosaic model of the structure of cell membranes. *Science*, 175(4023), 720-731. <https://doi.org/10.1126/science.175.4023.720>
- Skryabin, G. O., Komelkov, A. V., Savelyeva, E. E., & Tchevkina, E. M. (2020). Lipid Rafts in Exosome Biogenesis. *Biochemistry (Mosc)*, 85(2), 177-191. <https://doi.org/10.1134/s0006297920020054>
- Sok, M., Sentjerc, M., & Schara, M. (1999). Membrane fluidity characteristics of human lung cancer. *Cancer Lett*, 139(2), 215-220. [https://doi.org/10.1016/s0304-3835\(99\)00044-0](https://doi.org/10.1016/s0304-3835(99)00044-0)
- Sok, M., Šentjerc, M., Schara, M., Stare, J., & Rott, T. (2002). Cell membrane fluidity and prognosis of lung cancer. *The Annals of Thoracic Surgery*, 73(5), 1567-1571. [https://doi.org/10.1016/S0003-4975\(02\)03458-6](https://doi.org/10.1016/S0003-4975(02)03458-6)
- Sommer, M. E., Elgeti, M., Hildebrand, P. W., Szczepek, M., Hofmann, K. P., & Scheerer, P. (2015). Chapter Twenty-Six - Structure-Based Biophysical Analysis of the Interaction of Rhodopsin with G Protein and Arrestin. In A. K. Shukla (Ed.), *Methods in Enzymology* (Vol. 556, pp. 563-608). Academic Press. <https://doi.org/https://doi.org/10.1016/bs.mie.2014.12.014>

- Song, Y., Kenworthy, A. K., & Sanders, C. R. (2014). Cholesterol as a co-solvent and a ligand for membrane proteins. *Protein Science*, *23*(1), 1-22.
<https://doi.org/10.1002/pro.2385>
- Stevic, M., Bokun, Z., Milojevic, I., Budic, I., Jovanovic, B., Krstic, Z., & Simic, D. (2016). Management of Anesthesia in a Child with a Large Neck Rhabdoid Tumor. *Med Princ Pract*, *25*(3), 290-292. <https://doi.org/10.1159/000443017>
- Stockert, J. C., Blázquez-Castro, A., Cañete, M., Horobin, R. W., & Villanueva, Á. (2012). MTT assay for cell viability: Intracellular localization of the formazan product is in lipid droplets. *Acta Histochemica*, *114*(8), 785-796.
<https://doi.org/https://doi.org/10.1016/j.acthis.2012.01.006>
- Stuelten, C. H., Parent, C. A., & Montell, D. J. (2018). Cell motility in cancer invasion and metastasis: insights from simple model organisms. *Nature Reviews Cancer*, *18*(5), 296-312. <https://doi.org/10.1038/nrc.2018.15>
- Su, K.-Y., & Lee, W.-L. (2020). Fourier Transform Infrared Spectroscopy as a Cancer Screening and Diagnostic Tool: A Review and Prospects. *Cancers*, *12*(1), 115.
<https://doi.org/10.3390/cancers12010115>
- Subczynski, W. K., & Wisniewska, A. (2000). Physical properties of lipid bilayer membranes: relevance to membrane biological functions. *Acta Biochim Pol*, *47*(3), 613-625.
- Sultan, I., Qaddoumi, I., Rodríguez-Galindo, C., Nassan, A. A., Ghandour, K., & Al-Hussaini, M. (2010). Age, stage, and radiotherapy, but not primary tumor site, affects the outcome of patients with malignant rhabdoid tumors. *Pediatric Blood & Cancer*, *54*(1), 35-40. <https://doi.org/10.1002/pbc.22285>
- Suntres, Z. E., Coccimiglio, J., & Alipour, M. (2015). The Bioactivity and Toxicological Actions of Carvacrol. *Critical Reviews in Food Science and Nutrition*, *55*(3), 304-318.
<https://doi.org/10.1080/10408398.2011.653458>
- SwissParam. (2020). <https://www.swissparam.ch/>
- Szlasa, W., Zendran, I., Zalesińska, A., Tarek, M., & Kulbacka, J. (2020). Lipid composition of the cancer cell membrane. *Journal of Bioenergetics and Biomembranes*, *52*(5), 321-342. <https://doi.org/10.1007/s10863-020-09846-4>
- Telleria, C. M. (2012). Drug Repurposing for Cancer Therapy. *Journal of cancer science & therapy*, *4*(7), ix-xi. <https://doi.org/10.4172/1948-5956.1000e108>
- Tenn, M. W., Steacy, L. M., Ng, C. C., & Ellis, A. K. (2018). Onset of action for loratadine tablets for the symptomatic control of seasonal allergic rhinitis in adults challenged with ragweed pollen in the Environmental Exposure Unit: a post hoc analysis of total symptom score. *Allergy, asthma, and clinical immunology : official journal of the Canadian Society of Allergy and Clinical Immunology*, *14*, 5-5.
<https://doi.org/10.1186/s13223-017-0227-4>
- Terwilliger, T., & Abdul-Hay, M. (2017). Acute lymphoblastic leukemia: a comprehensive review and 2017 update. *Blood cancer journal*, *7*(6), e577-e577.
<https://doi.org/10.1038/bcj.2017.53>
- Tomlinson, G. E., Breslow, N. E., Dome, J., Guthrie, K. A., Norkool, P., Li, S., . . . Green, D. M. (2005). Rhabdoid Tumor of the Kidney in The National Wilms' Tumor Study: Age at Diagnosis As a Prognostic Factor. *Journal of Clinical Oncology*, *23*(30), 7641-7645.
<https://doi.org/10.1200/JCO.2004.00.8110>
- Trabelsi, F., Bouthour, H., Bustame, S., Jabloun, A., Abdallah, R. B., & Kaabar, N. (2016). Rhabdoid Tumor of the Kidney: A New Case of Prenatal Diagnosis with Metastases

- Immediately. *Medical & Surgical Urology*, 5(3), 1-3. <https://doi.org/10.4172/2168-9857.1000167>
- Treuting, P. M., & Kowalewska, J. (2012). 16 - Urinary System. In P. M. Treuting & S. M. Dintzis (Eds.), *Comparative Anatomy and Histology* (pp. 229-251). Academic Press. <https://doi.org/https://doi.org/10.1016/B978-0-12-381361-9.00016-0>
- Van Blitterswijk, W. J., De Veer, G., Krol, J. H., & Emmelot, P. (1982). Comparative lipid analysis of purified plasma membranes and shed extracellular membrane vesicles from normal murine thymocytes and leukemic GRSL cells. *Biochim Biophys Acta*, 688(2), 495-504. [https://doi.org/10.1016/0005-2736\(82\)90361-3](https://doi.org/10.1016/0005-2736(82)90361-3)
- Van der Paal, J., Verheyen, C., Neyts, E. C., & Bogaerts, A. (2017). Hampering Effect of Cholesterol on the Permeation of Reactive Oxygen Species through Phospholipids Bilayer: Possible Explanation for Plasma Cancer Selectivity. *Scientific Reports*, 7(1), 39526. <https://doi.org/10.1038/srep39526>
- Van Der Spoel, D., Lindahl, E., Hess, B., Groenhof, G., Mark, A. E., & Berendsen, H. J. C. (2005). GROMACS: Fast, flexible, and free [<https://doi.org/10.1002/jcc.20291>]. *Journal of Computational Chemistry*, 26(16), 1701-1718. <https://doi.org/https://doi.org/10.1002/jcc.20291>
- Van Hoeven, R. P., Emmelot, P., Krol, J. H., & Oomen-Meulemans, E. P. M. (1975). Studies on plasma membranes: XXII. Fatty acid profiles of lipid classes in plasma membranes of rat and mouse livers and hepatomas. *Biochimica et Biophysica Acta (BBA) - Lipids and Lipid Metabolism*, 380(1), 1-11. [https://doi.org/https://doi.org/10.1016/0005-2760\(75\)90039-9](https://doi.org/https://doi.org/10.1016/0005-2760(75)90039-9)
- van Meer, G., & de Kroon, A. I. P. M. (2011). Lipid map of the mammalian cell. *Journal of Cell Science*, 124(1), 5-8. <https://doi.org/10.1242/jcs.071233>
- Venable, R. M., Brown, F. L. H., & Pastor, R. W. (2015). Mechanical properties of lipid bilayers from molecular dynamics simulation. *Chemistry and physics of lipids*, 192, 60-74. <https://doi.org/10.1016/j.chemphyslip.2015.07.014>
- Verma, A., Verma, M., & Singh, A. (2020). Animal tissue culture principles and applications. *Animal Biotechnology*, 269-293. <https://doi.org/10.1016/B978-0-12-811710-1.00012-4>
- Vogt, S., Löffler, K., Dinkelacker, A. G., Bader, B., Autenrieth, I. B., Peter, S., & Liese, J. (2019). Fourier-Transform Infrared (FTIR) Spectroscopy for Typing of Clinical Enterobacter cloacae Complex Isolates [10.3389/fmicb.2019.02582]. *Frontiers in Microbiology*, 10, 2582. <https://www.frontiersin.org/article/10.3389/fmicb.2019.02582>
- von Hoff, K., Hinkes, B., Dannenmann-Stern, E., von Bueren, A. O., Warmuth-Metz, M., Soerensen, N., . . . Rutkowski, S. (2011). Frequency, risk-factors and survival of children with atypical teratoid rhabdoid tumors (AT/RT) of the CNS diagnosed between 1988 and 2004, and registered to the German HIT database. *Pediatr Blood Cancer*, 57(6), 978-985. <https://doi.org/10.1002/pbc.23236>
- Wadhwa, R., Yadav, N. S., Katiyar, S. P., Yaguchi, T., Lee, C., Ahn, H., . . . Sundar, D. (2021). Molecular dynamics simulations and experimental studies reveal differential permeability of withaferin-A and withanone across the model cell membrane. *Scientific Reports*, 11(1), 2352. <https://doi.org/10.1038/s41598-021-81729-z>
- Wagner, L., Hill, D. A., Fuller, C., Pedrosa, M., Bhakta, M., Perry, A., & Dome, J. S. (2002). Treatment of metastatic rhabdoid tumor of the kidney. *J Pediatr Hematol Oncol*, 24(5), 385-388. <https://doi.org/10.1097/00043426-200206000-00012>

- Waldron, P. E., Rodgers, B. M., Kelly, M. D., & Womer, R. B. (1999). Successful treatment of a patient with stage IV rhabdoid tumor of the kidney: case report and review. *J Pediatr Hematol Oncol*, *21*(1), 53-57.
- Walsh, M. J., Singh, M. N., Stringfellow, H. F., Pollock, H. M., Hammiche, A., Grude, O., . . . Martin, F. L. (2008). FTIR Microspectroscopy Coupled with Two-Class Discrimination Segregates Markers Responsible for Inter- and Intra-Category Variance in Exfoliative Cervical Cytology. *Biomark Insights*, *3*, 179-189. <https://doi.org/10.4137/bmi.s592>
- Wang, E., & Klauda, J. B. (2017). Examination of Mixtures Containing Sphingomyelin and Cholesterol by Molecular Dynamics Simulations. *The Journal of Physical Chemistry B*, *121*(18), 4833-4844. <https://doi.org/10.1021/acs.jpcc.7b01832>
- Wang, H., & Meng, F. (2017). The permeability enhancing mechanism of menthol on skin lipids: a molecular dynamics simulation study. *J Mol Model*, *23*(10), 279. <https://doi.org/10.1007/s00894-017-3457-y>
- Wang, M., Zhao, J., Zhang, L., Wei, F., Lian, Y., Wu, Y., . . . Guo, C. (2017). Role of tumor microenvironment in tumorigenesis. *J Cancer*, *8*(5), 761-773. <https://doi.org/10.7150/jca.17648>
- Warren, K. E. (2018). Beyond the Blood:Brain Barrier: The Importance of Central Nervous System (CNS) Pharmacokinetics for the Treatment of CNS Tumors, Including Diffuse Intrinsic Pontine Glioma [Review]. *Frontiers in Oncology*, *8*(239). <https://doi.org/10.3389/fonc.2018.00239>
- Watanabe, T. (2018). Chapter 4 - The Cell. In T. Watanabe (Ed.), *Biophysical Basis of Physiology and Calcium Signaling Mechanism in Cardiac and Smooth Muscle* (pp. 99-137). Academic Press. <https://doi.org/https://doi.org/10.1016/B978-0-12-814950-8.00004-4>
- Wereszczynski, J., & McCammon, J. A. (2012). Statistical mechanics and molecular dynamics in evaluating thermodynamic properties of biomolecular recognition. *Quarterly reviews of biophysics*, *45*(1), 1-25. <https://doi.org/10.1017/S0033583511000096>
- Wijesundara, N. M., Lee, S. F., Cheng, Z., Davidson, R., & Rupasinghe, H. P. V. (2021). Carvacrol exhibits rapid bactericidal activity against *Streptococcus pyogenes* through cell membrane damage. *Scientific Reports*, *11*(1), 1487. <https://doi.org/10.1038/s41598-020-79713-0>
- Witzke, S., Duelund, L., Kongsted, J., Petersen, M., Mouritsen, O. G., & Khandelia, H. (2010). Inclusion of terpenoid plant extracts in lipid bilayers investigated by molecular dynamics simulations. *J Phys Chem B*, *114*(48), 15825-15831. <https://doi.org/10.1021/jp108675b>
- Wohlfart, S., Gelperina, S., & Kreuter, J. (2012). Transport of drugs across the blood-brain barrier by nanoparticles. *Journal of Controlled Release*, *161*(2), 264-273. <https://doi.org/https://doi.org/10.1016/j.jconrel.2011.08.017>
- Wong, R. S. Y. (2011). Apoptosis in cancer: from pathogenesis to treatment. *Journal of experimental & clinical cancer research : CR*, *30*(1), 87-87. <https://doi.org/10.1186/1756-9966-30-87>
- Wu, J., Armstrong, T. S., & Gilbert, M. R. (2016). Biology and management of ependymomas. *Neuro Oncol*, *18*(7), 902-913. <https://doi.org/10.1093/neuonc/nov016>
- Xue, H., Li, J., Xie, H., & Wang, Y. (2018). Review of Drug Repositioning Approaches and Resources. *International journal of biological sciences*, *14*(10), 1232-1244. <https://doi.org/10.7150/ijbs.24612>

- Yacoub, T. J., Reddy, A. S., & Szleifer, I. (2011). Structural effects and translocation of doxorubicin in a DPPC/Chol bilayer: the role of cholesterol. *Biophysical Journal*, *101*(2), 378-385. <https://doi.org/10.1016/j.bpj.2011.06.015>
- Yang, S.-T., Kreutzberger, A. J. B., Lee, J., Kiessling, V., & Tamm, L. K. (2016). The role of cholesterol in membrane fusion. *Chemistry and physics of lipids*, *199*, 136-143. <https://doi.org/10.1016/j.chemphyslip.2016.05.003>
- Yat, H. L., Francois, B., Jennifer, L., Jacques, T., & Veronique, M. (2017). Effects of a Series of Acidic Drugs on L-Lactic Acid Transport by the Monocarboxylate Transporters MCT1 and MCT4. *Current Pharmaceutical Biotechnology*, *18*(14), 1141-1150. <https://doi.org/http://dx.doi.org/10.2174/1389201019666180308091504>
- Yin, Q.-H., Yan, F.-X., Zu, X.-Y., Wu, Y.-H., Wu, X.-P., Liao, M.-C., . . . Zhuang, Y.-Z. (2012). Anti-proliferative and pro-apoptotic effect of carvacrol on human hepatocellular carcinoma cell line HepG-2. *Cytotechnology*, *64*(1), 43-51. <https://doi.org/10.1007/s10616-011-9389-y>
- Zachowski, A. (1993). Phospholipids in animal eukaryotic membranes: transverse asymmetry and movement. *Biochem J*, *294* (Pt 1)(Pt 1), 1-14. <https://doi.org/10.1042/bj2940001>
- Zalba, S., & ten Hagen, T. L. M. (2017). Cell membrane modulation as adjuvant in cancer therapy. *Cancer Treatment Reviews*, *52*, 48-57. <https://doi.org/https://doi.org/10.1016/j.ctrv.2016.10.008>
- Zhang, G., Wang, M., Zhao, H., & Cui, W. (2018). Function of Axl receptor tyrosine kinase in non-small cell lung cancer. *Oncology letters*, *15*(3), 2726-2734. <https://doi.org/10.3892/ol.2017.7694>
- Zhang, H., Yang, B., Mu, X., Ahmed, S. S., Su, Q., He, R., . . . Gao, G. (2011). Several rAAV vectors efficiently cross the blood-brain barrier and transduce neurons and astrocytes in the neonatal mouse central nervous system. *Mol Ther*, *19*(8), 1440-1448. <https://doi.org/10.1038/mt.2011.98>
- ZINC12. (2020). <https://zinc12.docking.org/>
- Zoete, V., Cuendet, M. A., Grosdidier, A., & Michielin, O. (2011). SwissParam: a fast force field generation tool for small organic molecules. *J Comput Chem*, *32*(11), 2359-2368. <https://doi.org/10.1002/jcc.21816>
- Zwaal, R. F. A., Comfurius, P., & Van Deenen, L. L. M. (1977). Membrane asymmetry and blood coagulation. *Nature*, *268*(5618), 358-360. <https://doi.org/10.1038/268358a0>